UNIVERSITY OF OKLAHOMA

GRADUATE COLLEGE

FABRICATION AND CHARACTERIZATION OF 3D-PRINTED CARBON FIBER-REINFORCED EPOXY COMPOSITE HONEYCOMB STRUCTURES WITH TAILORED CORE CONFIGURATIONS FABRICATED USING ENGINEERED VISCOELASTIC INKS

A DISSERTATION

SUBMITTED TO THE GRADUATE FACULTY

in partial fulfillment of the requirements for the

Degree of

DOCTOR OF PHILOSOPHY

By

ANIRBAN MONDAL
Norman, Oklahoma
2025

FABRICATION AND CHARACTERIZATION OF 3D-PRINTED CARBON FIBER-REINFORCED EPOXY COMPOSITE HONEYCOMB STRUCTURES WITH TAILORED CORE CONFIGURATIONS FABRICATED USING ENGINEERED VISCOELASTIC INKS

A DISSERTATION APPROVED FOR THE
SCHOOL OF AEROSPACE AND MECHANICAL ENGINEERING

BY THE COMMITTEE CONSISTING OF

Dr. Mrinal C. Saha, Chair

Dr. Yingtao Liu, Co-Chair

Dr. Zahed Siddique

Dr. Shivakumar Raman

Dedication

I dedicate this dissertation to my family: my mother, Sankari, my father, Prokash, my sisters, Anindita and Minu, my brother-in-law, Ashok, and my nephew, Riddish.

Julius Caesar

by

William Shakespeare

Act III, Scene II

Antony:

"Friends, Romans, countrymen, lend me your ears;

I come to bury Caesar, not to praise him.

The evil that men do lives after them;

The good is oft interred with their bones;

……………………………………..

……………………………………

My heart is in the coffin there with Caesar,

And I must pause till it come back to me."

Acknowledgements

First, I extend my gratitude to Dr. Mrinal C. Saha for providing me the opportunity to work in his research group at the University of Oklahoma. His support and guidance have been instrumental in the successful completion of my Ph.D. I also wish to thank my co-advisor, Dr. Yingtao Liu and other committee members, Dr. Raman and Dr. Siddique for providing their support throughout this journey. My sincere gratitude goes to Dr. M. Cengiz Altan, Dr. Yijie Jiang and Dr. Julian E.C. Sabisch for their contributions to my research. Additionally, I am grateful to my graduate committee members for their constructive insights and encouragement.

This accomplishment would not have been possible without the cooperation and camaraderie of my lab mates. I would like to express my heartfelt thanks to Davin Rhule, Dr. Mohammad Abshirini, Dr. Mohammad Charara, Emmanuel Hakizimana, Iain Kennedy, Omkar Gautam, and Dr. Kuntal Maity for their continuous support. I am especially grateful to Dr. Preston Larson and Dr. Tingting Gu for assisting me with SEM and OM imaging. I also sincerely appreciate Dr. Ramkumar Parthasarathy, Dr. Wilson Merchan-Merchan and Dr. David Baldwin for allowing me to use the high-speed camera and MTS testing machine. I sincerely appreciate the support of both current and former AME staff— Bethany Burklund, Samarpita Ghosh, Elyon Wall Ellis, Aaron Henley, David Madison, Billy Mays, and Greg Williams—as well as the professors for cultivating a collaborative and enriching research environment. I would also like to acknowledge Teijin Carbon and Evonik Corporation for providing us with carbon fibers and silica fillers.

I am profoundly grateful for the financial support that made this work possible, including Dr. Saha's research assistantship, AME department teaching assistantship, Dolese Teaching Fellowship, Jim and Bee Close Scholarship, Frank Chuck Mechanical Engineering Scholarship, and CASH scholarships.

On a personal note, I extend my heartfelt thanks to my mother, Sankari, my father, Prokash, my sisters, Anindita and Minu, my brother-in-law, Ashok, and my nephew, Riddish, for their unconditional love, encouragement, and support throughout this journey.

Finally, I would like to express my deepest gratitude to Dr. Hassan Mahfuz (FAU), Dr. D. Sen (IIT Kharagpur-OENA), Dr. Ashoke Bhar (IIT Kharagpur- OENA), Dr. O.P. Sha (IIT Kharagpur-OENA), and Dr. V. Nagarajan (IIT Kharagpur- OENA) for their constant support and invaluable guidance, and help that shape the course of my academic path. I consider myself incredibly fortunate to have had their mentorship during this journey.

Table of Contents

Abstract

This study investigates the fabrication and mechanical characterization of lightweight, moderate-to-high-strength short carbon fiber-reinforced epoxy composite honeycomb cores and sandwich structures, produced using direct ink writing (DIW) 3D printing and customized viscoelastic inks. The engineered epoxy-based inks (I1–I4), containing 10–40 wt.% short carbon fibers, exhibit shear-thinning and yielding properties, enabling mold-free DIW fabrication of bioinspired cellular structures with hexagonal (H), triangular (T), and square (S) core geometries at infill densities of 30% – 50%. These inks were also used to fabricate sandwich structures with varied core configurations. This fabrication approach results in production of honeycomb cores and sandwich structures with superior surface finish and dimensional accuracy. The base materials (I1–I4) were characterized through tensile testing as per ASTM D638 Type V standards. Microstructural analysis of the printed specimens reveals print-induced fiber alignment, with fibers predominantly oriented along the a_{33} direction compared to a_{11} and a_{22}.

The mechanical behavior of the structures was evaluated under in-plane and out-of-plane compression, as well as three-point bending, to assess their load-bearing capacity, energy absorption and flexural performance. In-plane compression tests showed stiffness improvements of 59%, 43%, and 47%, and strength gains of 106%, 93%, and 162% in triangular, hexagonal, and square cores, respectively, as infill density increased from 30% to 50%, with specific strength following similar trends. Out-of-plane compression tests showed significant improvements in load-bearing capacity as the infill increased from 30% to 40%, enhancing energy absorption (EA) by 11.7% (hexagonal), 98% (square), and 80.8% (triangular). Square cores demonstrated the highest EA, outperforming hexagonal and triangular designs. Analysis of the specific energy absorption (SEA) and crushing force efficiency (CFE) metrics indicated that the DIW-printed

composite honeycomb cores are very competitive when compared to conventional continuous fiber, metal, thermoplastic, and polymer-based cores.

The DIW-printed sandwich structures with integrated skins also showed enhanced flexural stiffness and load-bearing capacity with increased core layers (1L to 2L), although flexural strength exhibited a decreasing trend. Varying core geometries yielded mixed results, yet the DIW-printed carbon fiber-reinforced epoxy composite sandwich structures exhibited competitive flexural properties compared to published studies.

Overall, this study highlights the potential of DIW and engineered composite inks to produce high-performance cellular cores and sandwich structures with tailored mechanical properties, paving the way for advanced lightweight structural applications in crashworthiness, aerospace, and automotive engineering.

List of Figures

List of Tables

Chapter 1: Introduction

1.1. Honeycomb Core Structures and Its Applications

Lightweight honeycomb core structures, inspired by natural cellular materials like cork, balsa wood, bones, teeth, tusks, and horns, are increasingly used in advanced materials and architectures for structural protection and load-bearing applications [1-3]. Low weight, high energy absorption, and effective thermal insulation make honeycomb structures ideal for aerospace, marine, sports, and transportation industries [4-7], where these properties are essential.

The performance of honeycomb structures can be tailored by adjusting fabrication techniques [8-11], geometry [12, 13], microstructure [10], and base materials [14, 15]. Designed to convert external forces into internal energy through large deformations or strain, honeycomb cores excel at energy absorption [16]. The choice of core materials—including aluminum [14, 17], aramid paper [18, 19], and carbon/glass fiber-reinforced composites [8, 10, 20] —significantly impacts their mechanical properties.

Fabrication techniques are pivotal in advancing the widespread use of honeycomb cores by enabling cost-effective, high-quality production while maintaining structural integrity and performance. This chapter provides a comprehensive review of various fabrication methods categorized based on the materials utilized. It explores the benefits and limitations of each technique, considering both the manufacturing process and the material system employed. By analyzing these factors, this review underscores the importance of advanced manufacturing techniques, such as direct ink writing (DIW), in enabling the scalable and cost-effective production of honeycomb cores with diverse shapes and sizes for various engineering applications.

1.2. Expansion-Based Fabrication of Non-Metallic and Metallic Honeycomb Cores

The expansion process for fabricating Nomex/Thermoset honeycomb cores involved several key steps [18, 21] as shown in figure 1.1. Nomex paper sheets were cut into 50 mm-wide ribbons, onto which an epoxy-based adhesive was applied at regular intervals to achieve a honeycomb cell size of 9.5 mm. These adhesive-coated ribbons were then heated at 110°C for 5 minutes to evaporate the solvent. The dried ribbons were stacked and subjected to a curing process at 170°C for 30 minutes to ensure strong bonding.

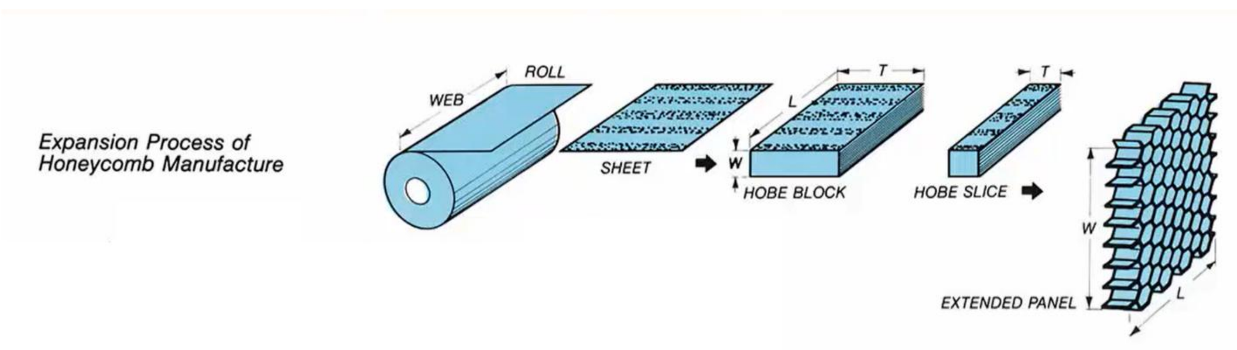

Figure 1. 1. A typical schematic representation of the expansion process [18, 21].

Once cured, the stacked ribbons were mechanically expanded perpendicular to their length using a custom-built expander until the desired hexagonal cell structure was formed. The expanded honeycomb cores were then impregnated with thermoset resins and underwent a series of curing cycles in an oven. This impregnation and curing process was repeated until the honeycombs reached the required density, which ranged from 2.0 to 4.0 lb/ft^3. The final honeycomb structures measured 300 × 300 × 50 mm, with a consistent hexagonal cell height of 9.5 mm. A comparable and similar process is employed for manufacturing metallic honeycomb cores [22].

1.2. Corrugation-Based Fabrication of Metallic Honeycomb Core

In the corrugation process, honeycomb cores are fabricated by forming corrugated sheets and bonding them together. This method is particularly suited for high-density metallic cores that cannot be expanded due to the thickness and strength of the metal sheets.

For metallic honeycomb cores, thin metal sheets are passed through toothed rollers to create corrugations as shown in figure 1.2 [21]. These corrugated sheets are then bonded to form a rigid honeycomb structure. This method is preferred for applications requiring high strength and durability, such as aerospace and industrial sectors. However, the process is more expensive due to the complexity of handling, stacking, and bonding the sheets, as well as the challenges in cutting from the block.

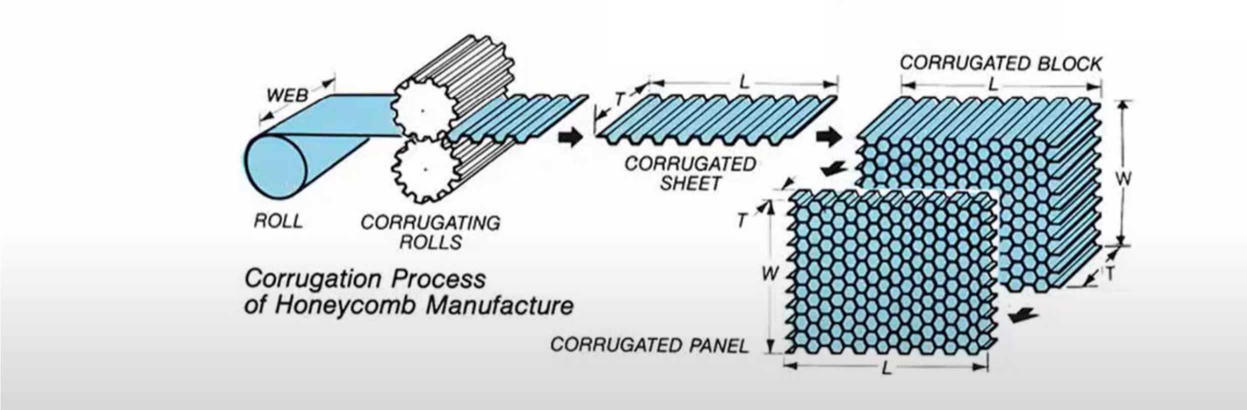

Figure 1. 2. A typical schematic representation of the corrugation process [21].

For paper-based honeycomb cores, the process involves stacking and bonding corrugated cardboard sheets to create an unexpanded block. Once cured, slices are cut from the block and expanded to form the honeycomb structure. While heavier than expanded honeycomb cores, this method remains cost-effective when using standard corrugated cardboard sheets. It enables the production of honeycomb cores with cell sizes as small as 5 mm, improving surface quality and reducing print-through effects. Paper honeycomb cores manufactured through this process are commonly used in automotive applications, including sunroof panels, hard tops, parcel shelves, spare wheel covers, and luggage floor assemblies.

1.3. Fiber-Reinforced Honeycomb Core Fabrication Techniques

Fiber-reinforced composite honeycomb cores are categorized and reviewed based on fabrication techniques, as illustrated in figure 1.3. This figure outlines the primary fabrication methods and the types of reinforcing fibers reported in the literature, offering a comprehensive understanding of fiber-reinforced composite honeycomb materials.

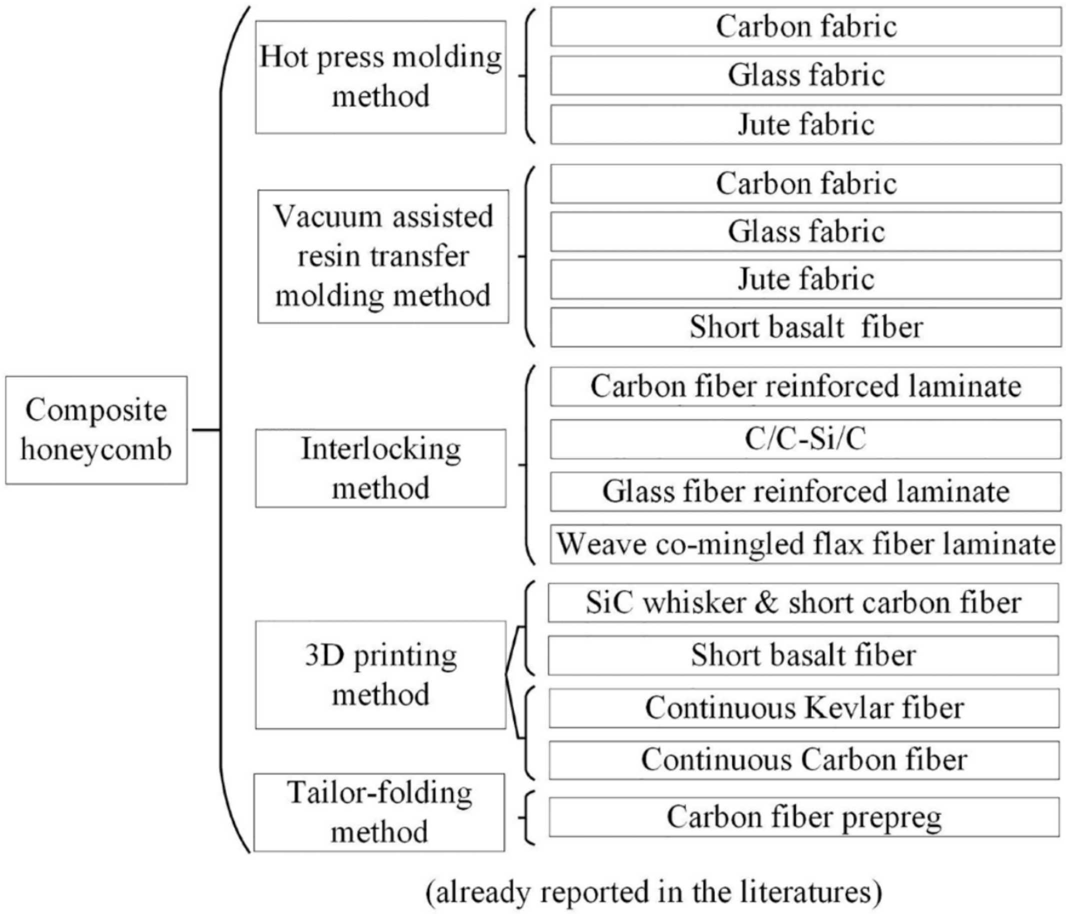

Figure 1. 3. Categorization of fiber-reinforced composite honeycomb materials documented in the literature [23].

1.3.1. Hot press molding method

Hot press molding is a widely used technique for manufacturing composite structures, including honeycomb cores, by curing fiber prepregs in specially designed molds. A natural fiber-reinforced hexagonal honeycomb structure was fabricated using this approach [24].

A mold featuring periodically arranged hexagonal steel pillars (figure 1.4 (a)) was employed, with the pillars securely fastened to a flat steel plate, leaving uniform gaps between them (figure 1.4 (b)) to accommodate fiber prepregs. Jute fabric was placed in a zigzag pattern within these grooves, followed by the infusion of vinylester resin. The assembly was then subjected to controlled pressure and temperature in a hydraulic press, curing the honeycomb walls between the steel inserts. The final structure post fabrication of fabricated core is shown in figure 1.4 (c). It is critical to note that the fabricated core structures exhibited variations in fiber volume fraction between longitudinal and diagonal walls due to differences in fiber layer distribution. However, the absence of transverse pressure during curing led to void formation, affecting fabrication quality.

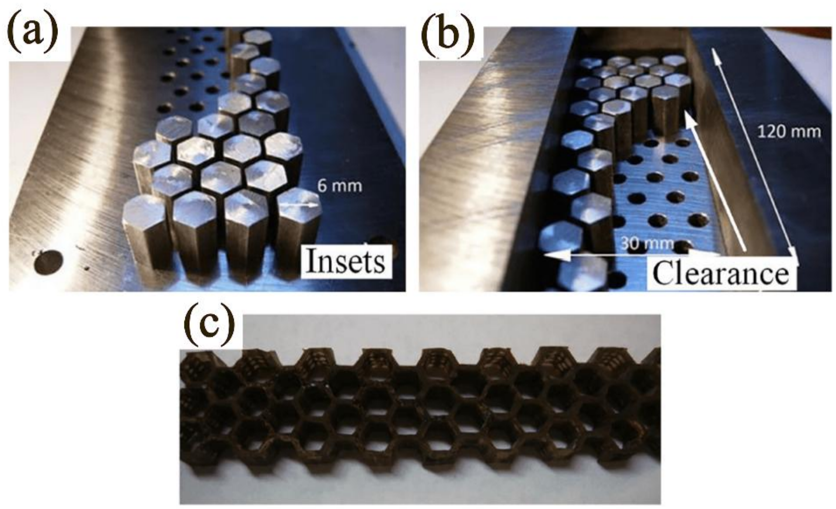

Figure 1. 4. The hot press molding process [24]: (a) bottom plate with inserts, (b) pre-assembled honeycomb structure, (c) final fabricated honeycomb core.

To address this issue, an improved hot press molding method was developed, incorporating a movable hexagonal pillar system (figure 1.5 (a) – (d)). This modification allowed lateral compression during curing, ensuring better resin distribution and structural integrity. The resin-wetted jute fabric was placed within the comb-like mold, laterally pressed to remove excess resin, and then cured under pressure and temperature.

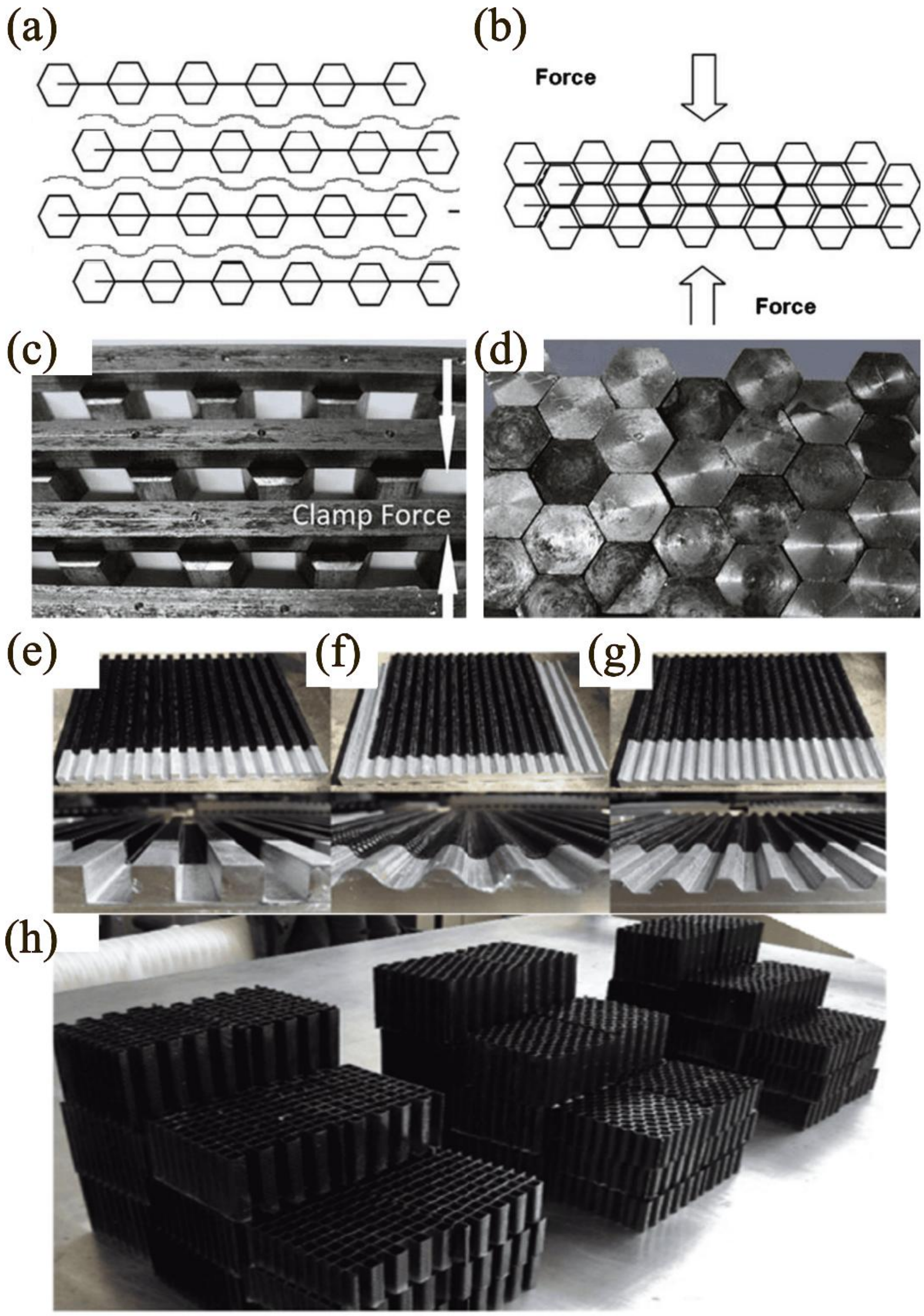

Figure 1. 5. Hot press molding with lateral compression [24]: (a) fabrics placed in the mold, (b) compression force applied to the combs, (c) open mold view, (d) closed mold view. Hot press molding with corrugated molds [8]: (e) square molds, (f) circular molds, (g) hexagonal molds, (h) fabricated honeycomb blocks.

A further variation of this technique replaces hexagonal pillars with corrugated molds, such as square, circular, or hexagonal molds (figure 1.5 (e) – (g)), to preform fiber prepregs into precise shapes before assembly. These cured, singly corrugated sheets were then cut to the desired height and bonded to form the final honeycomb structure (figure 1.5 (h)), ensuring uniform wall thickness and improved structural quality [8].

1.3.2. Interlocking Method

The interlocking method, developed for fabricating grid structures without molds, offers a cost-effective and scalable approach to manufacturing composite materials [25]. These grid structures, characterized by large cell sizes and thick walls, are assembled by interlocking grooved pieces, simplifying fabrication while maintaining structural integrity.

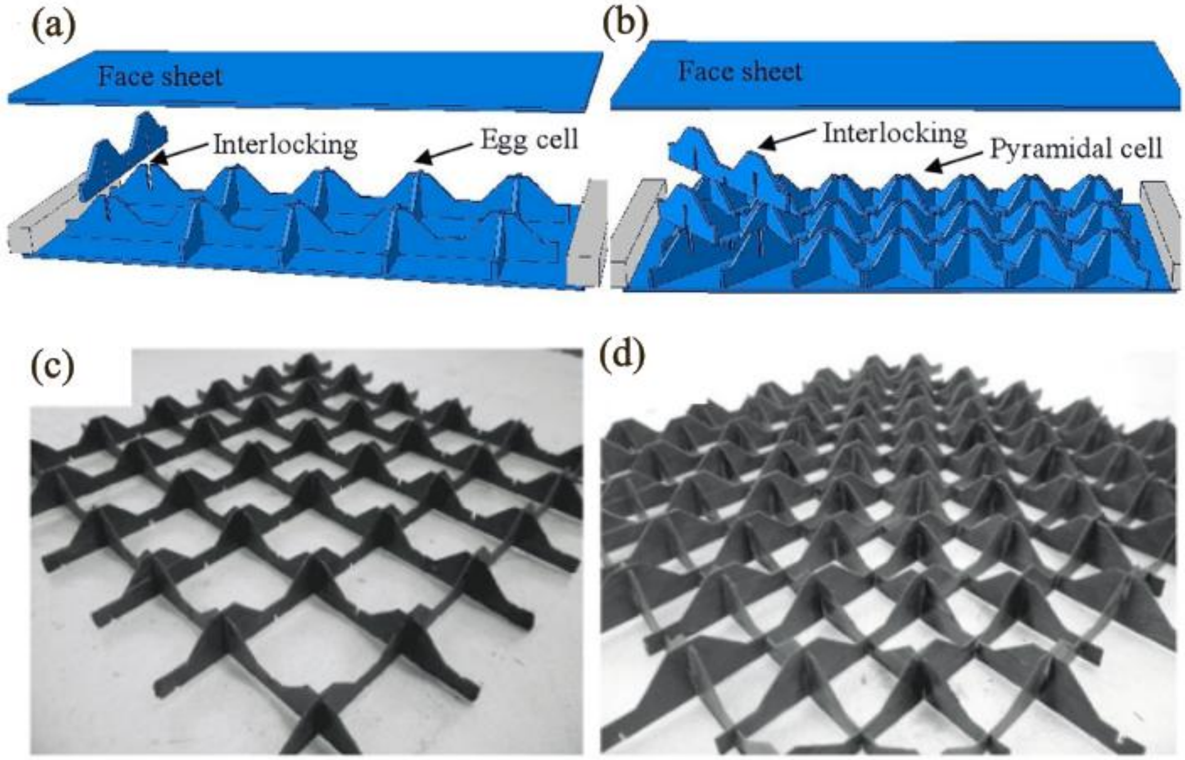

Figure 1. 6. Fabrication of sandwich columns with 3D honeycomb grid cores using cut carbon fiber-reinforced composite sheets and the interlocking method [26]: (a) egg honeycomb grids, (b) pyramidal honeycomb grids. Photographs of egg honeycomb grid cores with 3.0% relative density (c) and pyramidal honeycomb grid cores with 6.0% relative density (d) [27].

In this method, pultruded glass fiber composite ribs, with fibers aligned along the rib direction, maximize stiffness and strength. Grid configurations can be categorized as bi-grid, tri-grid, or quad-grid, depending on the number of ribs crossing each intersection. Bi-grids exhibit superior compressive strength due to their high longitudinal stiffness, while tri-grids and quad-grids provide balanced compressive and shear properties, with the latter excelling in shear resistance due to increased interlocking restraint.

The interlocking method has also been applied to fabricate square-honeycomb cores from composite sheets, mirroring metallic honeycomb manufacturing [28]. Additionally, carbon fiber bi-grid composites with varied fiber architectures have been developed using this approach [29]. To further enhance mechanical properties, the Kagome-grid configuration was introduced, leveraging carbon fiber reinforcement for optimized compressive and shear performance [30, 31].

Initially, interlocking honeycomb grids featured closed-cell architectures due to the absence of perforations in the laminates. However, the method has been adapted to create open-cell structures using modified interlocking components [26, 32], as illustrated in figure 1.6 (a) – (b). A further advancement involved manufacturing 3D carbon fiber composite egg and pyramidal honeycomb grids [27]. In this process, T700/epoxy prepreg laminates are cut using an electronic engraving machine, and interlocked through specific caulking grooves—long grooves for egg-shaped grids and a combination of long and short grooves for pyramidal grids (figure 1.6 (c) - (d)).

Despite its advantages, this method presents challenges, particularly at rib intersections, where fiber interference can lead to local stiffness reductions and potential failure points. However, interlocking mitigates these issues while significantly enhancing manufacturability at a lower cost. Its versatility allows adaptation to various materials, expanding its applications across engineering and scientific fields, from macroscopic structural components to nanoscale systems [33].

1.3.3. Vacuum-Assisted Resin Transfer Molding

VARTM is widely used in the composite industry for manufacturing large, complex structures at a low cost. This method is well-suited for producing high-quality fiber-reinforced honeycomb materials using specialized molds [34]. In this process, hexagonal molds hold strips of jute woven fabric in place on a bottom panel (figure 1.7 (a)). To minimize voids, a polyester resin and curing agent mixture is infused into the mold under vacuum assistance (figure 1.7 (b)). After curing, the honeycomb core is bonded to composite face sheets using a heated hydraulic press (figures 1.7 (c) – (d)).

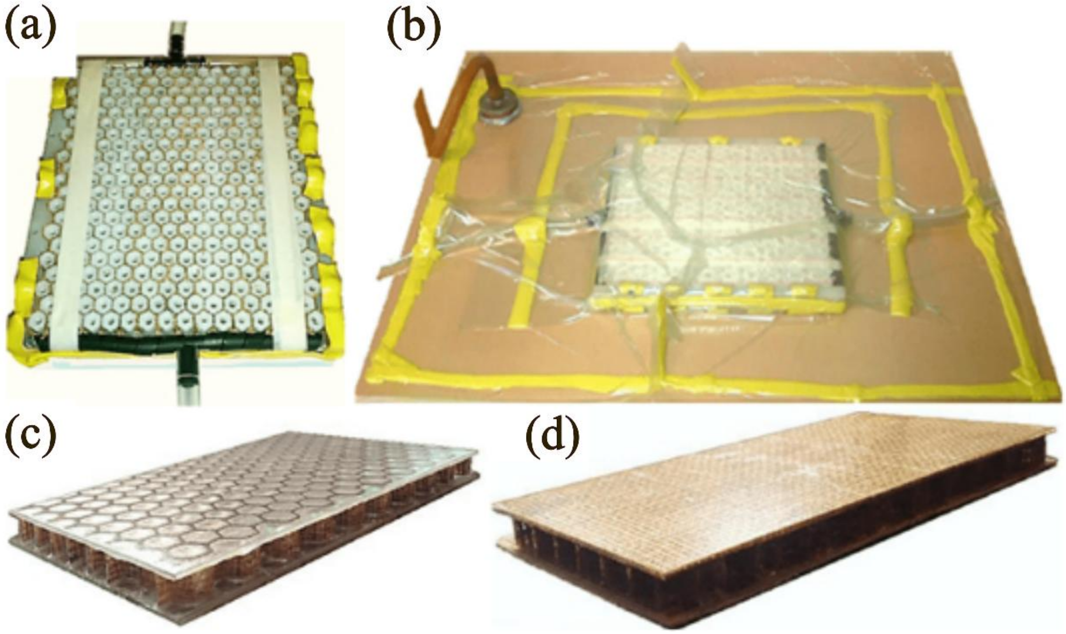

Figure 1. 7. Vacuum-assisted resin transfer molding (VARTM) process [34]: (a) Hexagonal molds with jute woven fabric strips fixed in the bottom panel, (b) Resin infusion assisted by a vacuum pump, (c) Sample sandwich panel with glass fiber skins jute fiber honeycomb core, (d) Jute fiber-reinforced honeycomb sandwich panel.

Compared to hot press molding, VARTM allows for greater design flexibility, enabling the fabrication of honeycomb structures with irregular shapes and customized configurations. However, both methods require high-cost molds and manual processing, which can limit the scalability and affordability of composite honeycomb materials.

1.3.4. Tailor-folding Method

The tailor-folding method enables the high-speed fabrication of cellular cores from planar fiber-reinforced prepregs while maintaining fiber continuity and structural integrity [35]. This approach eliminates weak points such as interlocking slots, ensuring that all fibers remain continuous within the honeycomb cells. Unlike mold-dependent methods, the tailor-folding process allows for scalable production without size limitations. By using woven fiber prepregs or stacked plies, it achieves high mechanical performance at a low surface mass density.

As illustrated in figure 1.8 (a), the process consists of four steps: cutting, folding, curing, and assembling. A numerical control cutting machine pre-cuts slits into the prepreg, followed by a critical two-stage folding step where the material is shaped into a semi-hexagonal corrugated form before being folded back and bonded into a honeycomb structure. Handling thick prepregs with multiple layers is challenging, but the method is well-suited for thin-walled, lightweight honeycombs with engineering applications.

Curing is performed in an autoclave at 130°C and 0.5 MPa for 2 hours, with PTFE hexagonal prism molds inserted to maintain cell shape until resin solidification. This method allows for diverse honeycomb configurations, as shown in figure 1.8 (b), ranging from closed-cell to open-cell structures. The final assembly involves bonding the honeycomb core to face sheets using epoxy-based adhesive, as demonstrated in figure 1.8 (c) with a 300 mm × 300 mm sandwich panel.

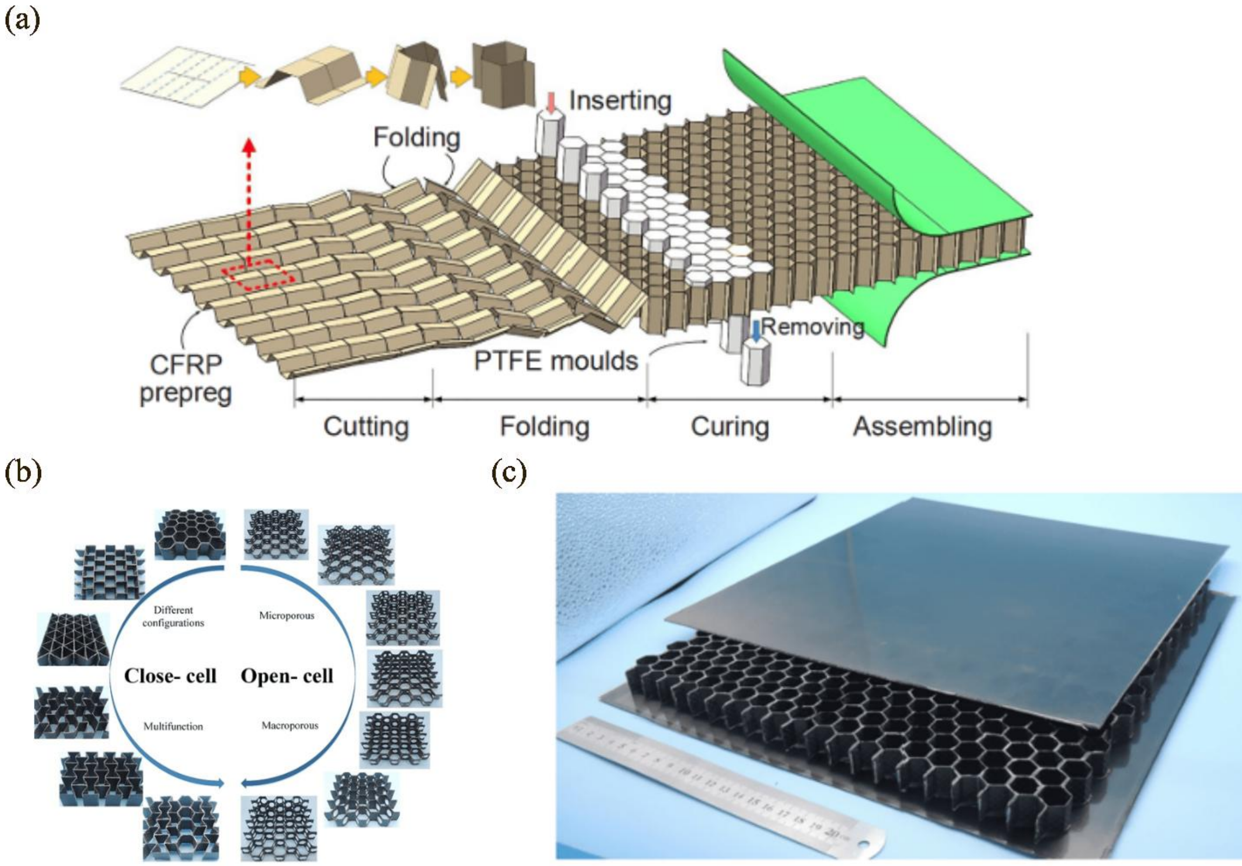

Figure 1. 8. (a) Schematic of the tailor-folding fabrication process [35]. (b) Illustrating two types of fiber-reinforced honeycomb cores: closed-cell honeycombs with various configurations and functions, and open-cell honeycombs ranging from microporous to macroporous structures. (c) Also shown is a 300 mm × 300 mm fiber-reinforced sandwich panel with a hexagonal honeycomb core.

The tailor-folding method offers a significant advantage in continuous manufacturing, unlike traditional hand-based molding techniques. Although its low fault tolerance remains a challenge, automation is feasible with optimized materials and processes. Computer-programmed cutting and folding lines support a streamlined production line, reducing time and labor costs while enhancing fabrication speed and scalability.

1.3.5. 3D Printing Method

Recent advancements in 3D printing provide exceptional flexibility in designing and fabricating complex cellular architectures. While traditional approach of using fused filament fabrication (FFF) for cellular structures using thermoplastic filament, recently a direct ink writing (DIW) 3D printing has been adapted for fabricating fiber-reinforced composites [36-45]. A hierarchical ink formulation, incorporating Epon 826 epoxy resin, nano-clay platelets, and dimethyl methyl phosphonate, was developed for this purpose [10], as shown in figure 1.9 (a) – (b). The nano-clay platelets impart shear-thinning behavior, essential for extrusion-based printing. Silicon carbide whiskers and short carbon fibers were added to enhance stiffness and yield stress, ensuring minimal aggregation or sedimentation due to their solid-like nature at rest. The fiber-filled epoxy ink was printed through a 200 μm nozzle and thermally cured to complete polymerization. Various honeycomb structures with different cell geometries were successfully printed.

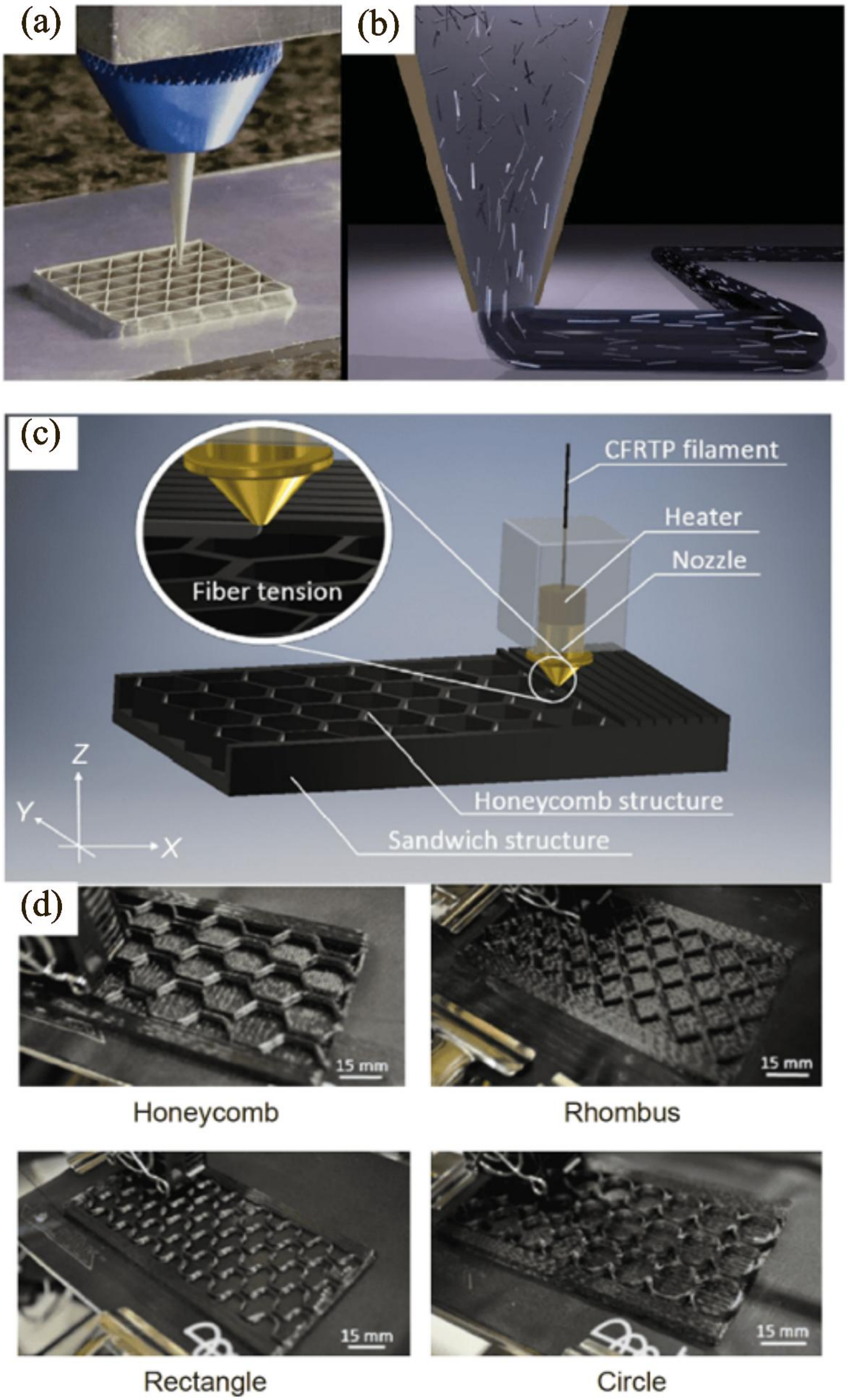
(a)
(b)
(c)
CFRTP filament
Heater
Nozzle
Fiber tension
Honeycomb structure
Sandwich structure
Z
Y
X
(d)
15 mm
Honeycomb
Rhombus
Rectangle
Circle

Figure 1. 9. DIW 3D printing method [10]: (a) DIW-printed triangular honeycomb composite; (b) schematic of composite ink deposition during DIW-printing. 3D printing with continuous carbon fibers [13]: (c) schematic of sandwich structure fabrication; (d) sandwich specimens featuring four different honeycomb core designs.

However, short-fiber-based 3D printing has limitations, including nozzle clogging due to particle aggregation, inconsistent mechanical reinforcement, and anisotropic fiber alignment affecting strength. To overcome these issues, a continuous carbon fiber 3D printing method was developed [13]. As shown in figure 1.9 (c), an FDM-type printer extruded continuous carbon fiber alongside thermoplastics, maintaining fiber tension using a polytetrafluoroethylene tube to prevent filament buckling. The extrusion speed was synchronized with the printer's movement, allowing seamless filament transitions. A one-piece sandwich structure with a honeycomb core was fabricated, along with variations in core geometry (figure 1.9 (d)). Despite these improvements, a major limitation remains: fabrication-induced defects, shape fidelity issues, poor fiber impregnation, voids, fiber pullout, and misalignment persist [13, 46-48], leading to premature failure and limiting the strength of printed parts.

DIW 3D printing, despite using short fiber reinforcement, offers a promising approach for fabricating composite honeycomb structures with viscoelastic thermoset-based inks, while other AM techniques face inherent challenges: FFF suffers from warping and weak filler-matrix bonding, DLP and SLA struggle with filler dispersion and curing, and PBF has difficulties with filler distribution [49]. DIW's selective multi-material ink deposition enables precise geometric control at multiple scales, yet challenges like post-cure shrinkage (2-3%) in DIW-printing of neat thermoset light cure epoxy [50], low fiber volume content (~15 vol%) in fiber-reinforced epoxy [51], high extrusion pressures, and fabrication inaccuracies—such as nodal misalignment and cell wall waviness—limit its effectiveness for high-performance applications.

This study addresses a few challenges including nozzle clogging, low-fiber content, print quality by developing engineered multi-material ink with desired shear-thinning and flow yield characteristics to fabricate sandwich core with different geometries. Addressing these issues by developing a diverse range of printable multi-material composite ink formulations containing 10 – 40 wt.% fiber content to fabricate honeycomb structures with precisely tailored mechanical properties, improved print quality, and reduced extrusion pressure. This advancement not only expands the scalability and efficiency of additive manufacturing for lightweight, high-strength cellular architectures but also allows for the integration of multifunctional materials, paving the way for designing and fabricating composite honeycomb cores with flexible core architecture for next-generation aerospace, automotive, and structural applications.

1.4. Objective

This dissertation presents a comprehensive study on designing and developing composite inks for DIW printing of honeycomb composite cores and sandwich structures with tailored mechanical properties. The research objectives are categorized as follows:

I. Develop, fabricate, and characterize DIW-printed honeycomb composite cores using tunable multi-material inks with carbon fiber concentrations ranging from 10–40 wt.%.

II. Examine the in-plane compression behavior of DIW-printed honeycomb composite cores.

III. Analyze the out-of-plane compression response and energy absorption characteristics of DIW-printed honeycomb composite cores.

IV. Assess the mechanical performance of DIW-printed sandwich structures through three-point bending tests.

Chapter 2: 3D Printable Ink Formulations and Characterizations

2.1. Introduction

3D printing enables the creation of complex three-dimensional structures with virtually unlimited geometric freedom. Among various additive manufacturing techniques, Direct Ink Writing (DIW) has gained prominence as a versatile and efficient method for fabricating high-precision composite structures. DIW offers several key advantages, including (i) compatibility with a diverse range of printable materials, (ii) minimal environmental constraints during printing, and (iii) the ability to tailor mechanical properties through controlled microstructural design.

The DIW process involves extruding viscoelastic inks through a translating nozzle under shear stress, depositing material in a precise layer-by-layer manner to construct the final 3D object. For successful fabrication, three fundamental steps must be ensured: (i) maintaining smooth and uninterrupted ink flow through the syringe and nozzle, (ii) achieving continuous and stable extrusion of the ink, and (iii) ensuring uniform deposition on the printing platform.

A critical factor in DIW printing is the formulation of inks with desired rheological properties that govern their printability. These properties include shear yielding, where carbon fiber-reinforced epoxy inks transition from a gel-like to a fluid-like state under applied stress, and shear thinning behavior, which facilitates smooth extrusion under increasing shear rates. The precise tuning of these rheological characteristics dictates the suitability of a material for DIW-based 3D printing, directly impacting print resolution, structural integrity, and overall fabrication efficiency.

This chapter presents an advanced manufacturing strategy for designing and formulating 3D-printable inks composed entirely of short carbon fibers, epoxy resin, and specialized additives. The formulated composite inks integrate short carbon fibers as the primary reinforcement, epoxy as the binding matrix, and fumed silica along with a rheology modifier to fine-tune the ink's viscoelastic behavior. This tailored formulation enables precise extrusion-based additive manufacturing via Direct Ink Writing (DIW). A critical aspect of this approach is the precise control of rheological properties to ensure printability and structural integrity of the printed constructs. The ink's viscoelastic characteristics are systematically adjusted by varying the weight fractions of fumed silica, carbon fibers, and the rheology modifier. This enables the material to exhibit essential flow properties, including shear yielding—allowing the ink to transition from a solid-like to a flowable state under applied stress—and shear thinning—facilitating smooth extrusion and deposition while maintaining structural stability post-printing. By leveraging these rheological principles, the developed composite inks achieve a balance between flowability and mechanical robustness, making them highly suitable for fabricating complex, high-performance carbon fiber-reinforced structures through DIW.

2.2. Experimental

2.2.1. Materials

A two-part, low-viscosity infusion-grade epoxy (Part A resin and Part B hardener) was obtained from PRO-SET, alongside milled carbon fibers (7 µm diameter and 71.14 ± 11.66 mm length) from Teijin Carbon, and fumed silica from Evonik Corporation, all of which were used as received. The epoxy served as the matrix material, while fumed silica was incorporated to modify the ink's viscosity. This addition enhanced the shear-thinning behavior of the ink, which is crucial for ensuring smooth extrusion during the printing process, and also improved the interfacial adhesion between the carbon fibers and the epoxy matrix. Furthermore, fumed silica imparted thixotropic properties to the ink, allowing it to maintain its shape post-extrusion and contributing to better control over print resolution. The carbon fibers acted as the primary reinforcement in the composite, while the fumed silica also acted as a rheology modifier to optimize the ink's flow characteristics, enabling improved printability and fiber-matrix bonding during the DIW process.

2.2.2. Ink Preparation

The printable inks were prepared by first combining Part A epoxy with fumed silica in a planetary mixer at 2000 rpm for 2 minutes to achieve a uniform mixture. Carbon fibers were then added in incremental 1g batches, with each batch mixed for 1 minute at 2000 rpm to ensure thorough dispersion. This process continued until the desired carbon fiber concentration was reached. Following this, Part B epoxy was introduced and mixed at 2000 rpm for 1 minute, followed by the addition of a rheology modifier. The final mixture was carefully defoamed and degassed to remove any air bubbles that could affect the printing quality.

Four distinct ink formulations, labeled I1-I4, were developed, with variations in silica content (ranging from 2 wt.% to 6 wt.%) and carbon fiber content (10, 20, 30, and 40 wt.%), while maintaining a constant rheology modifier concentration of 2 wt.%. These formulations were specifically engineered to enable the direct ink writing (DIW) of honeycomb structures with customizable core geometries and mechanical properties. The ability to adjust both silica and carbon fiber content allowed for fine-tuning of the inks' rheological properties, which were crucial for the successful 3D printing of high-performance, lightweight composite structures with tailored mechanical characteristics.

2.2.3. Rheological Characterization of the Inks

The rheological properties of the inks I1-I4, as designed in Section 2.2.2, were evaluated using a Discovery HR-3 Rheometer (TA Instruments). The rheometer was equipped with a 40 mm flat geometry at the top and a temperature-controlled Peltier stainless steel plate at the bottom to maintain a consistent test environment. A gap of 1000 µm was carefully maintained between the top and bottom fixtures to secure the ink during testing. Steady-state flow tests were conducted to assess the inks' viscosity and flow behavior over a shear rate range of 10^{-2} to 30 s^{-1}. These tests were carried out at a controlled temperature of 22°C, with a 1-minute preconditioning period to stabilize the inks before measurement. This thorough rheological analysis provided critical data on the inks' flow characteristics, enabling better understanding and optimization of the printable inks for DIW applications.

2.2.4. 3D Printing Process

A customized direct ink writing (DIW) 3D printer was utilized to fabricate tensile test specimens following ASTM D638 Type-V standards using inks I1–I4. Two print orientations were implemented: “longitudinal (L),” where the print paths and fibers aligned parallel to the applied load, and “transverse (T),” where they aligned perpendicular to the load. The DIW printer comprised key components, including an extrusion head, a build platform, a control system, a pneumatic pressure controller, and an X-Y-Z motion system. Ink formulations, as detailed in figure 2.1 (a), were used for fabricating tensile test specimens with longitudinal and transverse print paths as shown in figure 2.1 (b) and (c). The extrusion speed was maintained at 10 mm/min for all specimens unless otherwise noted. Post-printing, specimens underwent an initial curing phase at room temperature for 8 hours, followed by a post-curing process at 82 °C for an additional 8 hours.

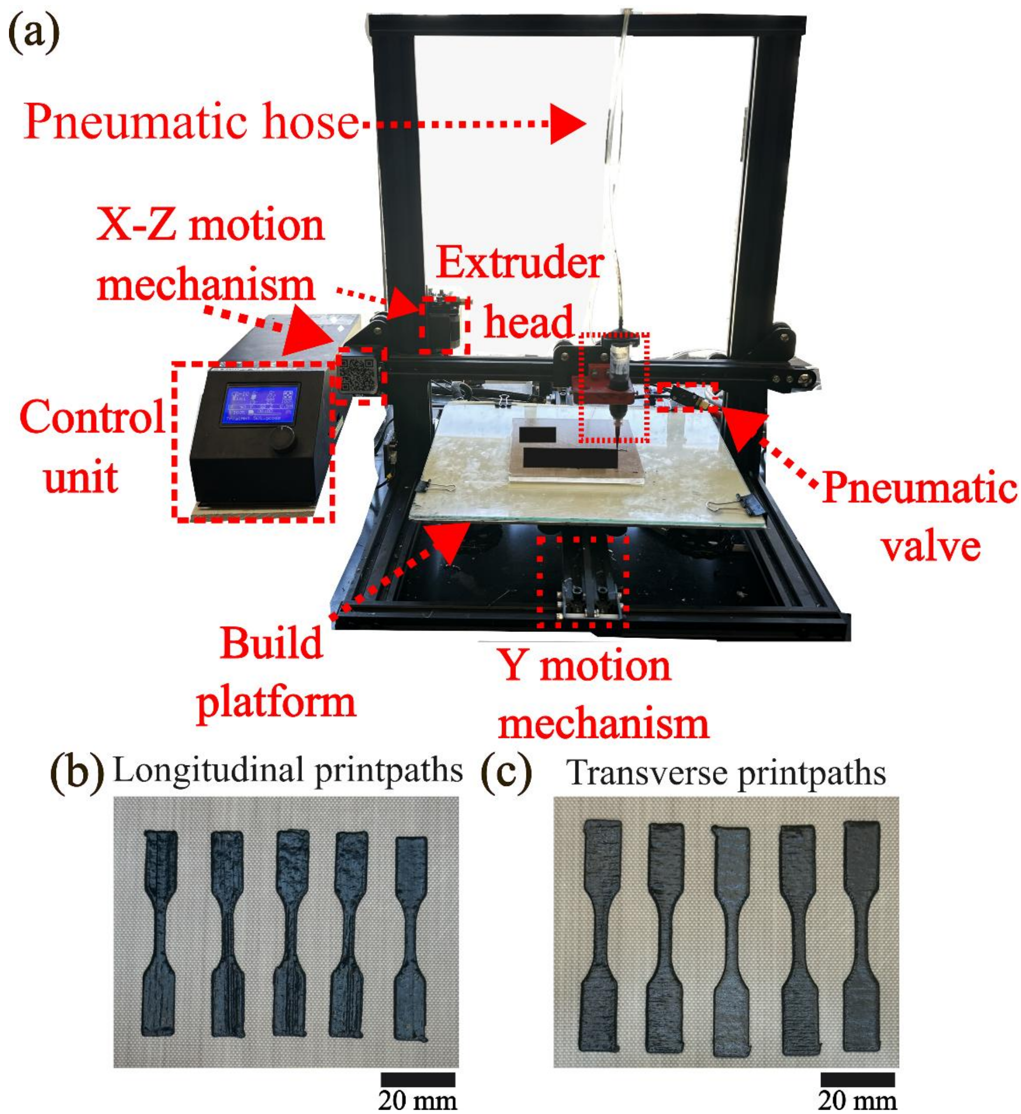

Figure 2. 1. (a) DIW print set-up. DIW-printed specimens with (b) longitudinal and (c) transverse print paths.

2.2.5. Characterizations of Mechanical Properties

The tensile properties of all four variants of inks (Ink 1 - 4), each comprising longitudinal and transverse printed tensile specimens with their respective inks, were evaluated through tensile testing. A minimum of ten specimens (five longitudinal and five transverse) per ink variant were tested using a displacement-controlled dual-column Instron 5969 tensile testing system at a strain rate of 1 mm/min.

2.2.6. Microstructural and Fiber Orientation Characterization

This study conducted microstructural characterization of composite tensile specimens fabricated using DIW inks. The composite samples were sectioned and embedded in quick-cure acrylic, followed by polishing with an automated Struers Labopol-5 polisher using DiaPro Largo and Dur polishing agents. This process exposed the carbon fiber surfaces embedded within the epoxy matrix for analysis.

High-resolution scanning electron microscopy (SEM) was employed to examine three distinct polished surfaces: the top surface (x-y plane), bottom surface (x-y plane), and cross-section (x-z plane). SEM images of the top and bottom surfaces were used to evaluate fiber alignment along the extrusion direction, while cross-sectional images provided insights into fiber orientation distribution throughout the specimen thickness.

To quantify fiber orientation, second-order orientation tensors (a_{11}, a_{22}, a_{33}, a_{12}, a_{13}, a_{23}) were calculated using an in-house script developed in ImageJ. The spatial orientation of a single fiber and its unit vector $\vec{\rho}$ is defined in a spherical coordinate system by ($r = 1$, θ, ϕ) as shown in figure 2.1 (a). The second-order representation (p_1, p_2, p_3) of the unit vector $\vec{\rho}$ in the cartesian coordinate system is given in equation (2.1):

$$\begin{aligned} p_1 &= \sin\theta\cos\phi \\ p_2 &= \sin\theta\sin\phi \\ p_3 &= \cos\theta \end{aligned} \tag{2.1}$$

The orientation tensors are calculated as the dyadic product of the unit vector $\vec{\rho}$. The orientation tensor T is a symmetric second-order tensor and is expressed in equation (2.2).

$$T = \begin{pmatrix} a_{11} & a_{12} & a_{13} \\ a_{12} & a_{22} & a_{23} \\ a_{13} & a_{23} & a_{33} \end{pmatrix} = \begin{pmatrix} p_1^2 & p_1\,p_2 & p_1\,p_3 \\ p_1\,p_2 & p_2^2 & p_2\,p_3 \\ p_1\,p_3 & p_2\,p_3 & p_3^2 \end{pmatrix} \tag{2.2}$$

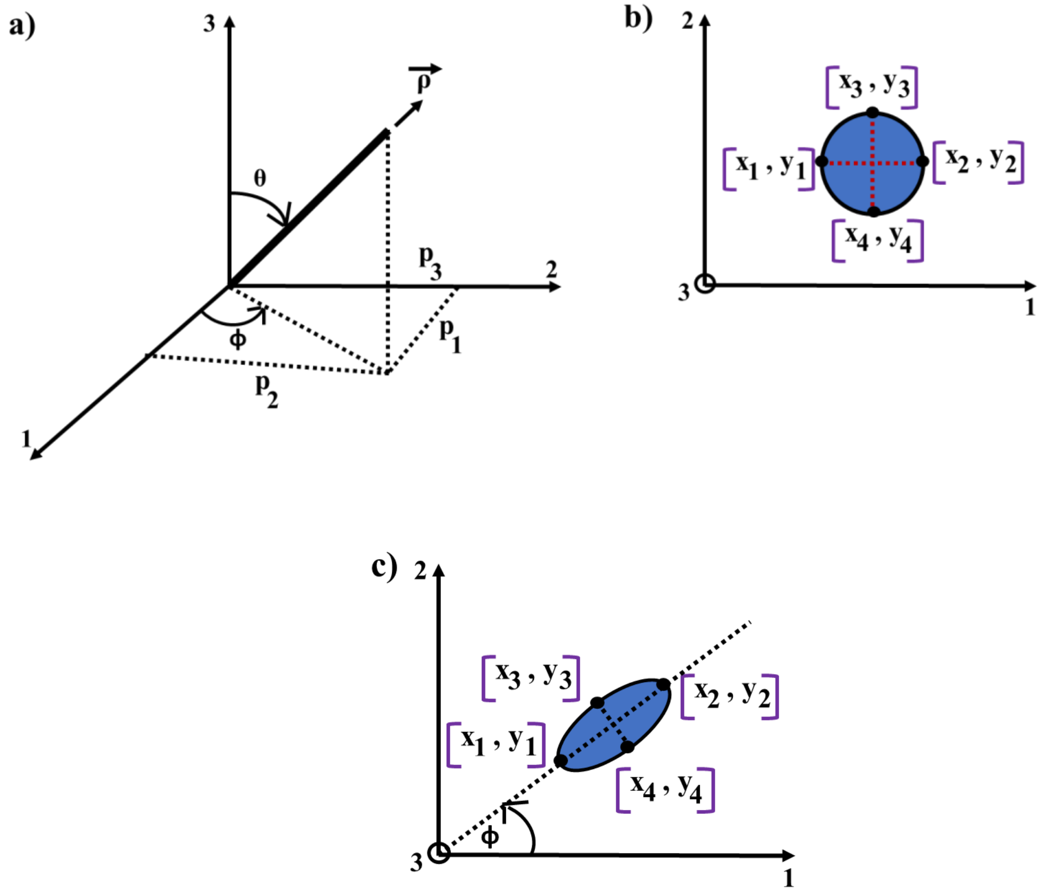

Figure 2. 2. (a) Coordinate system defining the components of the unit vector $\vec{\rho}$. (b) Circular, and (c) elliptical cross-section of the cylindrical fibers defining the axes endpoints and in-plane angle.

Thus, the orientation tensors ($a_{11}, a_{22}, a_{33}, a_{12}, a_{13}, a_{23}$) were used to detect and measure the cross-section information of the individual carbon fiber from the SEM micrographs (2D) and present 3D information about the orientation of fibers within the epoxy matrix. This method was illustrated by Bay and Tucker [52]. Figures 2.1 (b) and 2.1 (c) highlight the procedure to determine the diameter of the circular cross-section and the major and minor axis of the elliptic cross-section with the aid of the endpoints. Thus, allowing to determine the in-plane and out-of-plane angle ϕ and θ. This multi-plane imaging and analysis approach enabled a comprehensive understanding of fiber orientation both on the surface and within the bulk of the composite specimens.

2.3. Results and Discussion

2.3.1. Rheological Characteristics of the Printable Inks

The rheological properties of DIW ink are critical for precise control during the printing process, enabling smooth and continuous extrusion through the syringe barrel and nozzle without requiring excessive extrusion forces. The ink must exhibit shear-thinning behavior, allowing it to flow easily through a high-resolution nozzle under applied pressure. Additionally, the ink must maintain its printed shape after deposition, closely aligning with the digital design and preserving geometric fidelity across stacked layers until curing. Therefore, DIW inks should exhibit solid-like, elastic behavior below a specific stress threshold, known as the shear yield stress (τ_0), and transition to a flow state when this threshold is surpassed. The raw materials, such as silica and carbon fibers, play a pivotal role in designing the rheological parameters of the ink. Silica fillers enhance the ink's lubrication effect, while carbon fibers increase flow resistance during extrusion. Increasing silica content raises the shear yield stress, a critical parameter for ensuring the printability of fresh ink, ultimately preserving the structural integrity of printed layers by maintaining their shape post-extrusion. Similar observations have been reported in previous studies [53, 54].

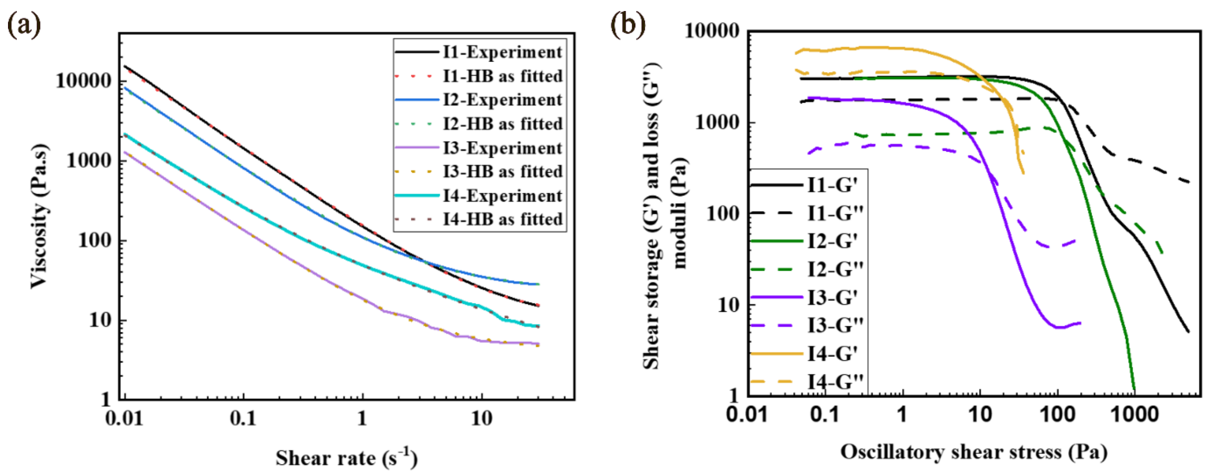

Figure 2. 3. Log-log plots of (a) viscosity as a function of shear rate and (b) storage and loss moduli as a function of oscillatory shear stress for fiber-reinforced epoxy inks of varying compositions, showing shear thinning and yielding behaviors, which are critical for 3D printability.

Figure 2.2 (a) presents the viscosity profiles of composite inks (Ink 1–4) obtained through steady-state flow analysis. All inks exhibit pronounced shear-thinning behavior, with viscosity decreasing by approximately two to three orders of magnitude as the shear rate increases from 0.01 to 30 s^{-1}—conditions typical in 3D printing. For example, Ink 2, composed of 5.25 wt.% silica and 20 wt.% carbon fibers, shows an initial viscosity of around 8,208 Pa·s at a low shear rate (0.01 s^{-1}), which sharply decreases to approximately 28 Pa·s at a higher shear rate (30 s^{-1}). This behavior is attributed to the 3D network formed by silica nanofillers [55, 56] and carbon fiber micro-fillers [57, 58] within the epoxy matrix, which increases the ink's viscosity. Under applied shear or external stress (e.g., pneumatic pressure during extrusion), this network temporarily breaks down, reducing the apparent viscosity and facilitating flow. Once the stress is removed (e.g., as the ink exits the nozzle), the network reforms, restoring the viscosity. This reversible process, characteristic of shear-thinning materials, allows extrusion through fine nozzles while maintaining the printed structure's integrity. The viscosity profiles also reveal that initial viscosity decreases with reduced silica content, indicating that nanoparticles have a more substantial impact on viscosity compared to microfillers. The viscosity and shear rate data were further analyzed using the Herschel-Bulkley (HB) fluid model (equation (2.3)) [59], shown in figure 2.2 (a). Parameters such as shear yield stress (τ_0), consistency index (K), and flow index (n) were derived via nonlinear regression analysis, with the model demonstrating excellent agreement with the experimental data. These results are summarized in table 2.1.

$$\eta = \frac{\tau_0}{\dot{\gamma}} + K\dot{\gamma}^{(n-1)} \quad (2.3)$$

Viscosity and shear rate are represented by η (Pa.s), and $\dot{\gamma}$ (s^{-1}) respectively.

Further, the relationship between shear stress (τ), shear rate ($\dot{\gamma}$), printing speed (v), and nozzle size (r) is described by equation (2.4) [49], where τ_0, K, and n represent the yield stress, flow consistency factor, and power-law index, respectively, as detailed in table 2.1. Additionally, equation (2.5) [60] defines the shear rate ($\dot{\gamma}$) at the nozzle tip as a function of printing speed (assuming print speed is numerically equal to the velocity of the ink at the nozzle tip, v = 10 mm/min) and nozzle size (r = 0.20 mm and 0.29 mm) [60]. Results obtained using equations (2.4) and (2.5) show strong agreement with experimental data as shown in table 2.1.

$$shear\ stress\ \tau = \tau_0 + K\dot{\gamma}^{(n)} \quad (2.4)$$

$$shear\ rate\ at\ nozzle\ tip, \dot{\gamma} = \frac{4\ v}{\pi r} \qquad (2.5)$$

Table 2. 1. Summary of rheological parameters for all ink material formulations.

Inks	r	Shear rate ($\dot{\gamma}$)	*K*	*n*	τ_0	τ	τ_0 - Experimental (Cross-over point between G' and G")
	mm	s^{-1}	Pa.s		Pa	Pa	Pa
Ink 1	0.21	1.03	10.24	0.98	144.49	155.08	122.53
Ink 2	0.21	1.03	32.04	0.93	78.16	111.25	119.29
Ink 3	0.29	0.73	5.11	0.95	12.93	16.73	12.71
Ink 4	0.29	0.73	30.21	0.59	18.86	43.99	25.21

Dynamic oscillatory tests were conducted to assess the viscoelastic properties of the composite inks, as shown in figure 2.2 (b). The results demonstrate that all inks exhibit predominantly elastic behavior at low shear stresses, where the shear storage modulus (G′) exceeds the shear loss modulus (G″). This ensures the shape-retaining characteristics of the printed structures. When the applied shear stress surpasses the ink's yield shear stress (τ_0), G″ exceeds G′, marking a transition from solid-like to liquid-like behavior, which is essential for smooth extrusion during 3D printing. Inks with appropriate τ_0 are particularly advantageous for the direct ink writing (DIW) of freestanding structures, as they maintain structural integrity under low stresses from self-weight and gravity. The inclusion of silica nanofillers and carbon fibers enhances the shear storage modulus, improving the shape fidelity of the printed structures. The study reports G′ values ranging from 1,857 to 6,326 Pa and τ_0 values between 12 and 144 Pa, indicating satisfactory performance across all tested inks. Notably, Ink 4 exhibits a higher G′ compared to Ink 1, attributed to its increased carbon fiber content.

While absolute parameters such as viscosity (η), viscoelastic properties (G′, G″), and shear yield stress may vary across different DIW inks, their overall rheological trends align closely with those observed for Inks 1–4 in this study [10, 61, 62]. This consistency ensures both extrudability and the ability to maintain geometric fidelity in the printed structures.

2.3.2. Mechanical Properties

The tensile test results are illustrated in figure 2.3. As expected for short fiber composites, specimens with fibers aligned perpendicular to the loading axis display reduced stiffness (figure 2.3 (b)) and strength (figure 2.3 (c)), with only marginal improvements as the fiber weight fraction increases. In contrast, specimens with fibers aligned parallel to the loading direction exhibit a substantial enhancement in stiffness as fiber content increases (figure 2.3 (b)), alongside a continuous rise in strength with increasing fiber weight (figure 2.3 (c)). For example, tensile test samples printed with Ink 4 demonstrate a 183% increase in stiffness and a 36.9% increase in strength compared to those fabricated with Ink 1.

Figure 2.3 (d) presents a schematic representation of the tensile test specimen, indicating the locations where micrographs were captured to evaluate fiber alignment induced by shear during the DIW process. This schematic provides insight into how extrusion parameters influence fiber orientation. Figures 2.3 (e) and (f) display micrographs of specimens printed with longitudinal and transverse print paths, respectively, demonstrating the effect of DIW on fiber alignment. These images highlight the capability of DIW to control and engineer microstructural orientation, which can be strategically leveraged to tailor the mechanical properties of the printed composites in this study

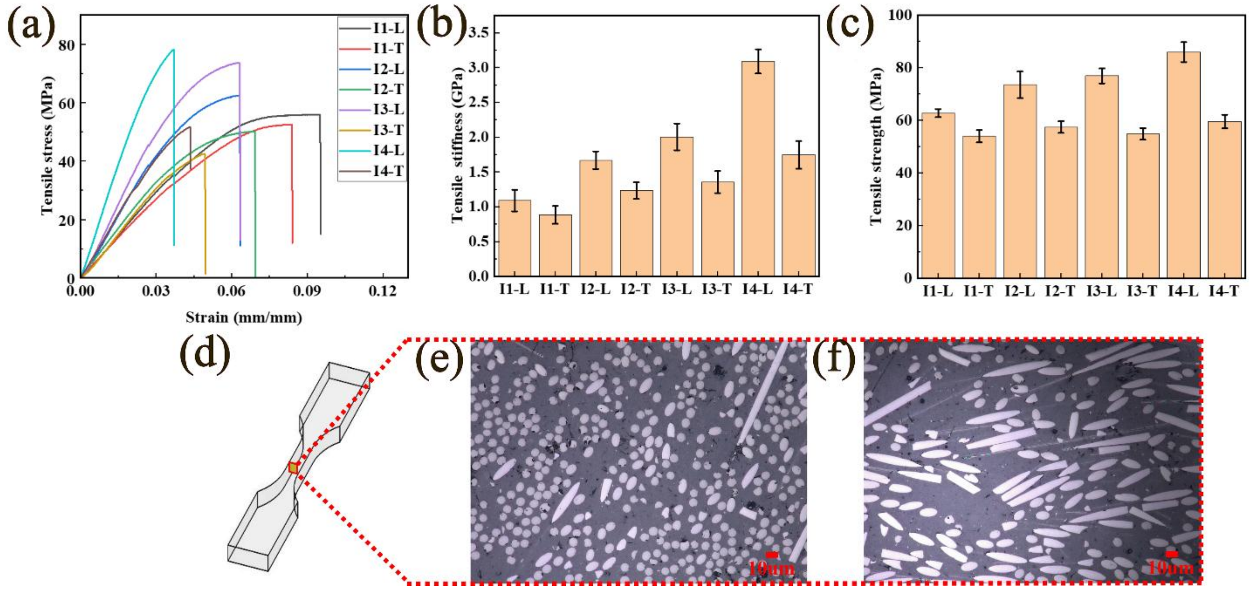

Figure 2. 4. Mechanical Properties of DIW-Printed Specimens Fabricated with Inks 1–4. (a) Representative stress-strain curves of tensile specimens printed using Inks 1–4. (b) Bar plot showing the average Young's modulus of the specimens. (c) Bar plot depicting the average tensile strength of the printed specimens. (d) Schematic representation of a tensile test specimen, indicating the micrograph locations used for assessing print-induced fiber alignment. (e) Micrographs show fiber alignment in longitudinally printed tensile specimens. (f) Micrographs illustrate fiber orientation in transversely printed tensile specimens.

Figures 2.4 (a) and (b) present representative SEM images of the top and bottom surfaces of DIW-printed specimens, illustrating the fiber alignment induced during the printing process. Figures 2.4 (c) and (d) depict the statistical orientation distribution of fibers on both surfaces, reinforcing the effectiveness of DIW in aligning fibers along the extrusion direction. Additionally, the statistical analysis in figures 2.4 (c) and (d) and table 2.2 reveals reduced fiber alignment on the bottom surface, likely due to the deposition of the soft ink material onto the substrate. This results in the flattening of the lower portion of the extruded filament, causing partial realignment of fibers initially aligned by shear during extrusion.

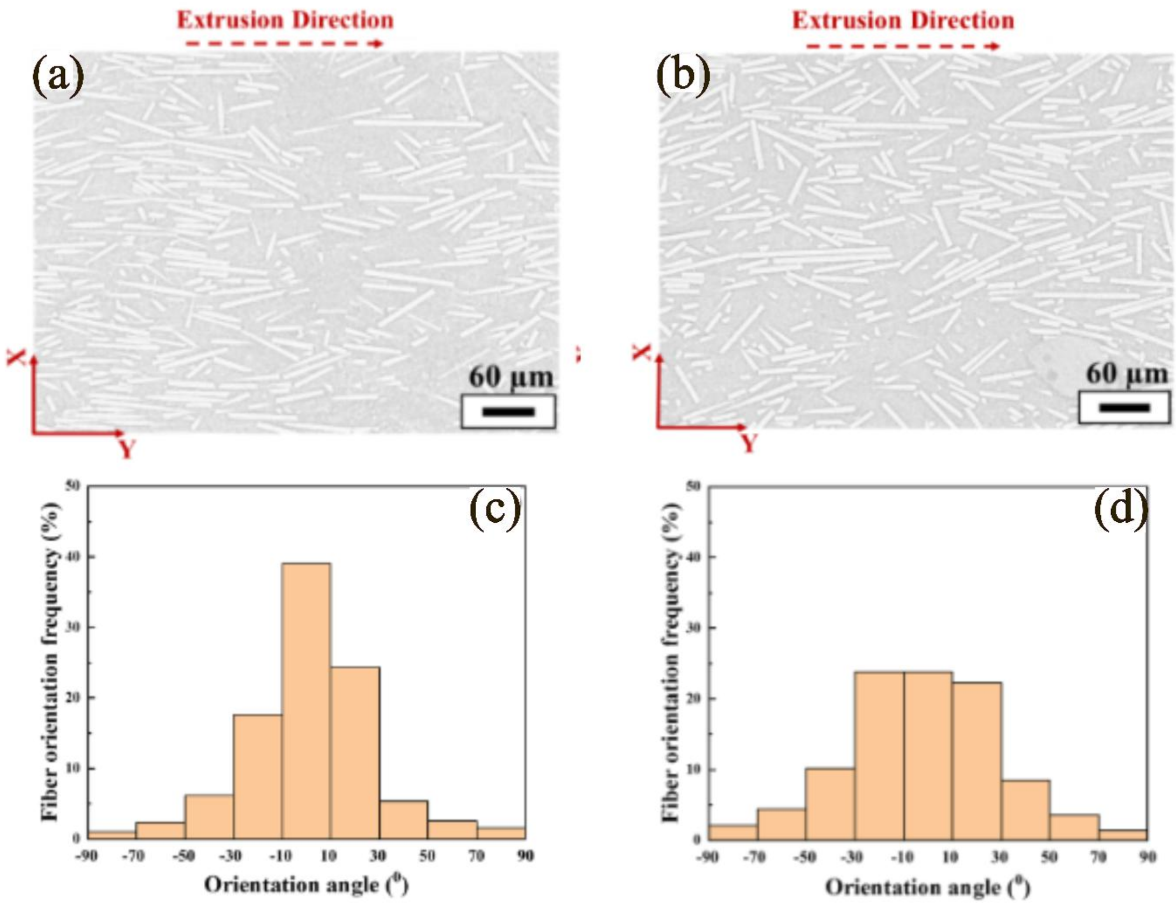

Figure 2. 5. SEM micrographs showing DIW print-induced fiber alignment on the (a) top and (b) bottom surfaces of the printed specimens. Statistical distribution of fiber alignment at the (c) top and (d) bottom surfaces, highlighting variations in fiber alignment due to the printing process.

Table 2. 2. Typical fiber alignment distribution at the top and bottom surface of DIW printed specimens.

Fiber alignment	**0 ≤ ±10°**	**0 ≤ ±20°**	**0 ≤ ±30°**
Top surface	39.00%	64.20%	81.00%
Bottom surface	23.80%	48.30%	69.90%

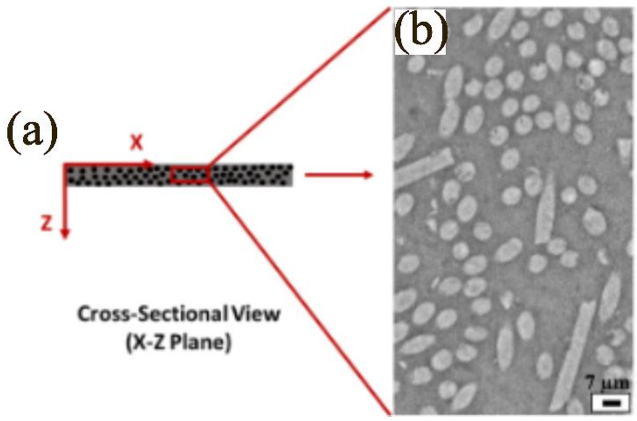

Figure 2. 6. (a) Schematic illustration of the cross-sectional view of the DIW-printed composite samples. (b) SEM images of the cross-section of the DIW-printed composite samples.

Table 2. 3. Components of second-order orientation tensor of the DIW printed specimens at the cross-section.

Cross-section of DIW printed specimens	a_{11}	a_{12}	a_{13}	a_{22}	a_{23}	a_{33}
Specimen	0.157	0.096	0.159	0.280	0.331	0.563

Figure 2.5 (a) presents a schematic representation of a representative cross-sectional region in the x-z plane, while figure 2.5 (b) displays SEM images of the cross-section of DIW-printed specimens. The fiber morphology in figure 2.5 (b) varies, appearing as circles, slender strips, or ellipses with different major-to-minor axis ratios, depending on the print parameters. Additionally, table 2.3 quantifies fiber orientation tensor components, showing a dominant alignment along a_{33} (extrusion direction, y-axis) with a notable distribution of fibers along a_{23} (yz-plane), a_{22} (z-axis), a_{13} (xy-plane), and a_{11} (x-axis), demonstrating the influence of the DIW process on fiber orientation.

2.4. Chapter Conclusion

In conclusion, we successfully developed 3D-printable fiber-reinforced epoxy inks suitable for DIW-based fabrication of tensile test composite specimens. Rheological characterization confirmed that the formulated inks exhibited the necessary shear thinning and yielding properties, ensuring smooth extrusion and structural integrity post-printing. Tensile testing demonstrated that increasing fiber concentration enhanced the stiffness and strength of specimens printed with longitudinal print paths. Additionally, microstructural analysis revealed print-induced fiber alignment, further highlighting the influence of DIW on composite microstructure and mechanical performance.

Chapter 3: In-Plane Compression of 3D-Printed Carbon Fiber-Reinforced Honeycomb Cores with Tailored Cellular Designs

3.1. Introduction

Additive manufacturing (AM), commonly referred to as 3D printing (3DP), has transformed rapid prototyping by facilitating the fabrication of cellular structures with customized geometries and material properties [63]. AM offers several advantages, including design flexibility, automation, efficiency, and cost-effectiveness [64]. The mechanical performance of cellular structures, such as honeycombs, can be engineered by modifying unit cell geometry [12, 13, 28, 65] and microstructure [10]. These structures are particularly effective under out-of-plane loading conditions but often exhibit lower in-plane strength [12]. Since practical applications typically involve multi-directional forces, a thorough investigation of in-plane mechanical properties is essential for accurately predicting structural behavior under complex loading scenarios. Although significant advancements have been achieved in the development of 3D-printed metallic honeycomb and truss structures for energy absorption applications [66], they often lack the lightweight characteristics and tunability provided by composite materials. Research on polymer-based cellular structures fabricated through fused filament fabrication (FFF), one of the most widely used AM techniques, has identified several challenges [67-69]. These include limited mechanical strength, poor surface quality, void formation, and restricted material options [70, 71]. Addressing these limitations is critical for advancing the performance of polymer-based cellular structures in engineering applications.

To address the limitations associated with FFF-printed thermoplastics, the incorporation of short carbon fibers has emerged as a promising solution, significantly improving the stiffness and strength of the printed structures. These fiber-reinforced composites offer enhanced design flexibility, enabling the creation of more robust and lightweight parts [72, 73]. Studies have shown that the addition of carbon fibers can lead to mechanical property enhancements of 2 to 3 times compared to unreinforced polymers, making them a valuable addition for applications requiring improved performance [74, 75].

Research has also focused on tailoring the properties of carbon fiber-reinforced composites, particularly in relation to infill density in CF/PEKK composites. The results indicate that increased infill density can improve stiffness but may reduce the material's ability to absorb energy, highlighting a trade-off between structural rigidity and energy dissipation in certain applications [15]. Furthermore, the performance of fiber-reinforced structures, particularly in 3D printing, is influenced by several challenges, including poor fiber-matrix bonding [76, 77], the formation of voids [15], and fiber misalignment [78]. These issues can weaken the material, reducing the overall strength and leading to premature failure of printed parts [63, 76]. Despite these challenges, research continues to explore methods for improving the quality of 3D-printed fiber-reinforced composites, aiming to overcome these limitations and enhance their applicability in more demanding engineering fields.

To enhance the mechanical properties and energy absorption capabilities of materials beyond traditional metals and soft polymers, there is an increasing focus on using short fiber-reinforced and unreinforced thermoplastics, as well as continuous fibers, in Fused Filament Fabrication (FFF) processing [79]. The integration of continuous fibers has been a key advancement in improving the strength, stiffness, and impact resistance of 3D-printed structures. In particular, co-extrusion techniques for creating continuous fiber-reinforced thermoplastic composite (CFRTPC) honeycomb structures have been developed, offering a promising route for fabricating lightweight yet high-strength materials [46-48]. One notable method, introduced by Sugiyama et al., uses pre-impregnated filaments to control fiber tension, which ensures consistent fiber alignment and improves the overall mechanical properties of the composite [13].

Additionally, a free-hanging 3D printing technique for CFRTPC lattice truss structures has been explored, providing an alternative approach for fabricating complex, high-performance composites in additive manufacturing [79]. While these advancements hold great potential, they are still plagued by several challenges that limit their performance and widespread application. Fabrication-induced defects such as poor fiber impregnation, voids, fiber pullout, and fiber misalignment during the printing process often undermine the quality of the printed parts [13, 46-48]. These issues lead to reduced strength and premature failure, restricting the durability and reliability of the parts and limiting their use in high-performance applications. Therefore, continued research is needed to refine the fabrication processes, improve fiber-matrix bonding, and address these defects to unlock the full potential of continuous fiber-reinforced thermoplastic composites in 3D printing.

To overcome the challenges faced by traditional additive manufacturing methods, direct ink writing (DIW), an advanced extrusion-based additive manufacturing technique, has emerged as a promising solution [49]. DIW enables the precise and controlled fabrication of 3D structures using a variety of materials, including thermosets, polymers, carbon nanotubes (CNT), and graphene oxide (GO) solutions [10, 63, 80-83]. The versatility of DIW lies in its ability to handle a wide range of materials, paired with the ability to design print-ready inks with tailored rheological properties such as viscosity, shear yield stress, and viscoelasticity [45, 49]. These properties ensure the accurate extrusion and shape retention of the printed structures, allowing for the rapid and precise creation of high-resolution, multi-material geometric features [10, 49, 51, 64]. This capability is particularly useful for fabricating filler-reinforced honeycomb structures [10, 51, 84]. Despite its potential, comprehensive research on designing and formulating multi-material printable inks remains limited. Challenges such as low fiber content [10, 51], print accuracy [85], geometric fidelity [10, 85], and the limitations of DIW-printed honeycomb composite cores—especially for in-plane mechanical properties—remain significant obstacles [10].

This study seeks to overcome these challenges by utilizing a series of engineered, print-ready inks with tailored fiber content, as developed in Chapter 2, to fabricate diverse honeycomb composite cores with optimized strength-to-density ratios. These epoxy-based viscoelastic inks enable the fabrication of lightweight, high-strength carbon fiber-reinforced epoxy composite honeycomb structures with customizable core configurations, cell sizes, and infill densities. These customized ink formulations enable the fabrication of nature-inspired cellular composites with intricate geometries, including hexagonal, triangular, and square cores. These structures exhibit superior mechanical properties compared to conventional unreinforced and reinforced thermoplastics, as well as metallic honeycomb cores. This study further investigates the inks capability for high-quality DIW fabrication. The surface quality of the resulting structures are assessed using optical imaging techniques to measure surface roughness. To understand the mechanical properties of the printed structures, in-plane compression tests are performed, and the results are compared with scaling laws and previous studies on 3D-printed composites and metal-based honeycombs. The findings highlight how geometric design, infill concentration, and fiber content play a critical role in tailoring the mechanical performance of DIW-printed honeycombs. Overall, this research demonstrates the potential of combining DIW with engineered inks to create advanced composite honeycombs with highly customizable mechanical properties, making them ideal for innovative, lightweight, and high-strength structural applications.

3.2. Experimental

3.2.1. 3D Printing Process

A customized direct ink writing (DIW) 3D printer was employed to fabricate a diverse range of composite honeycomb core structures and tensile test specimens. This printer included essential components such as an extrusion head, a build platform, a control system, a pneumatic pressure controller, and an X-Y-Z motion system, as illustrated in figure 3.1 (a). The ink formulations, detailed in chapter 2, were used to create various core geometries. Honeycomb core structures, along with integrated peripheral skins, were printed without the need for external adhesives, ensuring proper contact with the test fixture during mechanical testing.

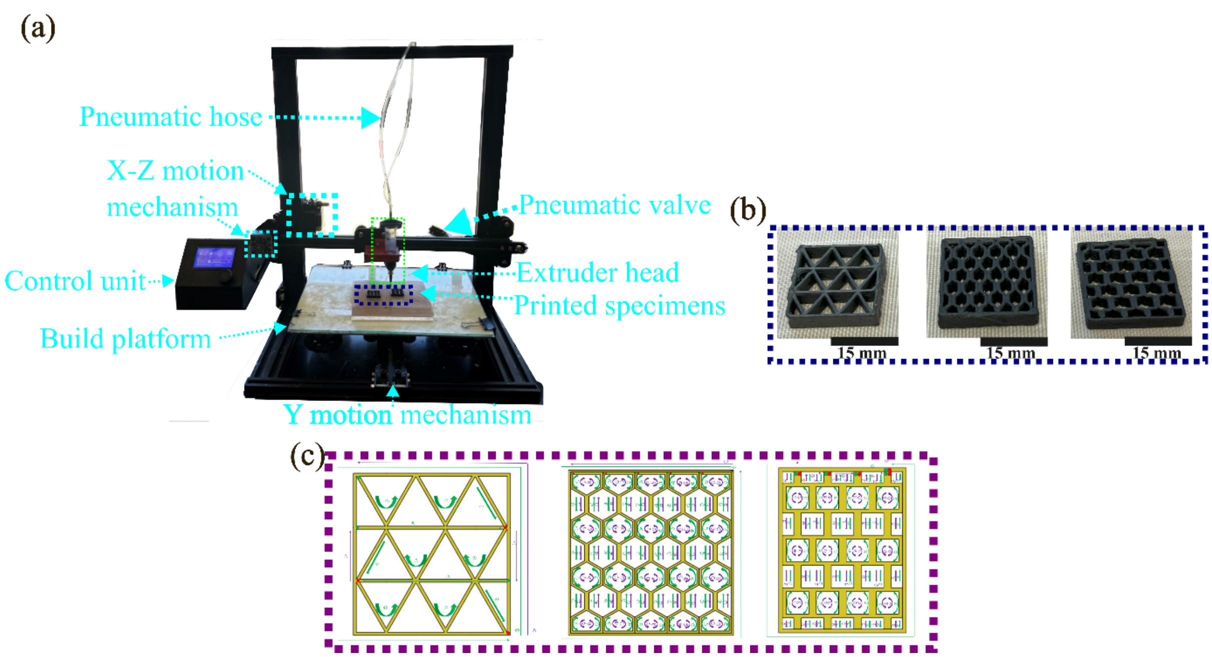

Figure 3. 1. DIW printing setup for short carbon fiber-reinforced honeycomb composite structures: (a) modified DIW printer setup, (b) sample prints of triangular, hexagonal, and square honeycomb structures having infill 40%, and (c) layer-wise print path design for the honeycomb composite structures.

The inks, prepared as described in chapter 2, were loaded into 10 ml luer-lock syringes, degassed, and mounted onto the DIW printer. Ink extrusion was controlled pneumatically via a pressure regulator, using g-code to direct the extrusion process. The printer used tapered tips with inner diameters of 0.41 mm for I1-I2 and 0.58 mm for I3-I4 to control the print resolution. Ink was deposited onto a PTFE-coated glass substrate to facilitate the easy removal of the printed structures. All DIW-printed honeycomb structures, shown in figure 3.1 (b), were fabricated at room temperature under pneumatic pressures of 6-10 psi.

Three-dimensional models were designed using SOLIDWORKS, and the corresponding STL files were converted into G-code using open-source software such as Slic3r and Repetier-Host. The generated G-code was customized to optimize printing continuity and minimize non-printing movements within and between print layers. Figure 3.1 (c) illustrates the multi-stroke print path strategies used for various core designs, highlighting the flexibility of the DIW process. The print, non-print, and stop actions are indicated in green, purple, and red, respectively, demonstrating the precise control of the deposition process.

This fabrication approach contrasts with the single-stroke continuous print paths typically used in 3D printing of continuous fiber-reinforced thermoplastic structures, which often suffer from print-induced defects [13, 86]. In contrast to common issues like overlap [46, 87] and unnecessary extrusion [13, 61] during non-print moves, the engineered print paths in this study, along with computer-controlled deposition, ensure accurate and defect-free fabrication of 3D parts, eliminating material waste.

The fabrication process was carried out under ambient conditions, followed by pre-curing and post-curing of the entire structure at 82°C for 8 hours. This curing process results in strong bonds among the cell edges and between adjacent printed layers, mitigating the interlaminar failure commonly observed in fiber-reinforced FFF structures [88]. The printing parameters included layer thicknesses of 0.41 mm and 0.58 mm, with a print speed of 10 mm/min. All configurations were fabricated with ten sequential print passes stacked in a bottom-up approach.

3.2.2. Compression Testing of Honeycomb Cores

In-plane quasi-static compression tests were performed to evaluate the compressive properties of the honeycomb core structures using an INSTRON 3345 testing machine, equipped with a 5000 N load cell. Each specimen was subjected to compression between two circular steel fixtures, applying a constant crosshead speed of 1 mm/min. Tests were conducted for each unique core configuration, with at least three specimens tested per configuration. This resulted in a total of 27 specimens for each ink type, amounting to 108 samples across four different ink formulations to ensure reliable and repeatable results.

Throughout the quasi-static compression tests, the deformation behavior of the honeycomb cores was meticulously captured using a high-resolution camera, with a 1920 x 1080 pixel resolution and a recording speed of 240 frames per second, providing detailed visual data on the material's response to compression. The nominal compressive stresses (σ) and strains (ϵ) of the fiber-reinforced honeycomb specimens were calculated based on the established formulas in equations

(3.1) and (3.2), ensuring accurate determination of their mechanical behavior under the applied loads.

$$\sigma = \frac{F}{A} = \frac{F}{WT} \quad (3.1)$$

$$\epsilon = \frac{\delta}{H} \quad (3.2)$$

The in-plane compressive stress (σ) and strain (ϵ) were determined using the following parameters: F represents the applied force, A is the cross-sectional area, W denotes the specimen width, T stands for the specimen thickness, H indicates the height of the specimen, and δ refers to the axial displacement. Stiffness was quantified by calculating the initial slope of the stress-strain curve, while the strength was determined based on the first peak stress observed in the curve during compression.

To ensure robust results, the average mechanical properties were derived from at least three independent tests for each variant. Specific stiffness and strength were computed by normalizing the measured values with respect to the specimen density, providing a clearer understanding of the material's performance under compression relative to its mass. This approach enabled the detailed evaluation of the mechanical characteristics and their variations across different core configurations.

3.2.3. Imaging

The surface roughness of the printed honeycomb cores were evaluated using a Keyence VHX-7000 digital microscope, providing high-resolution imaging for detailed surface inspection. To assess fiber alignment, specimens were first embedded in acrylic epoxy resin to preserve their structure, then polished sequentially with SiC grit papers (ranging from 800 to 4000) using a Struers Labopol 5 polisher. For finer resolution, the final polishing step was carried out manually with diamond slurries of 3 μm and 1 μm, followed by a colloidal silica solution (0.02 μm SiO_2) to achieve an ultra-smooth surface finish.

Before imaging, the samples underwent thorough preparation. They were sonicated in deionized water to remove any debris, degreased with ethanol and methanol to eliminate organic contaminants, and subsequently dried at 60°C for 24 hours to ensure moisture removal. This meticulous process allowed for a precise qualitative evaluation of fiber orientation and the overall surface characteristics of the printed cores.

3.3. Results and Discussion

3.3.1. DIW Printed Honeycomb Structures with Varied Core Designs

The scalability and applicability of the newly developed DIW-printable inks (I1-I4) as outlined in chapter 2 were evaluated through the fabrication of triangular (T), hexagonal (H), and square (S) honeycomb core structures with varying infill densities, as illustrated in figure 3.2. (a) – (f). These honeycomb structures, characterized by periodic prismatic cellular patterns, exhibit mechanical behavior governed by factors such as cell geometry [12, 89], infill density [90], and the properties of the base material [14, 15].

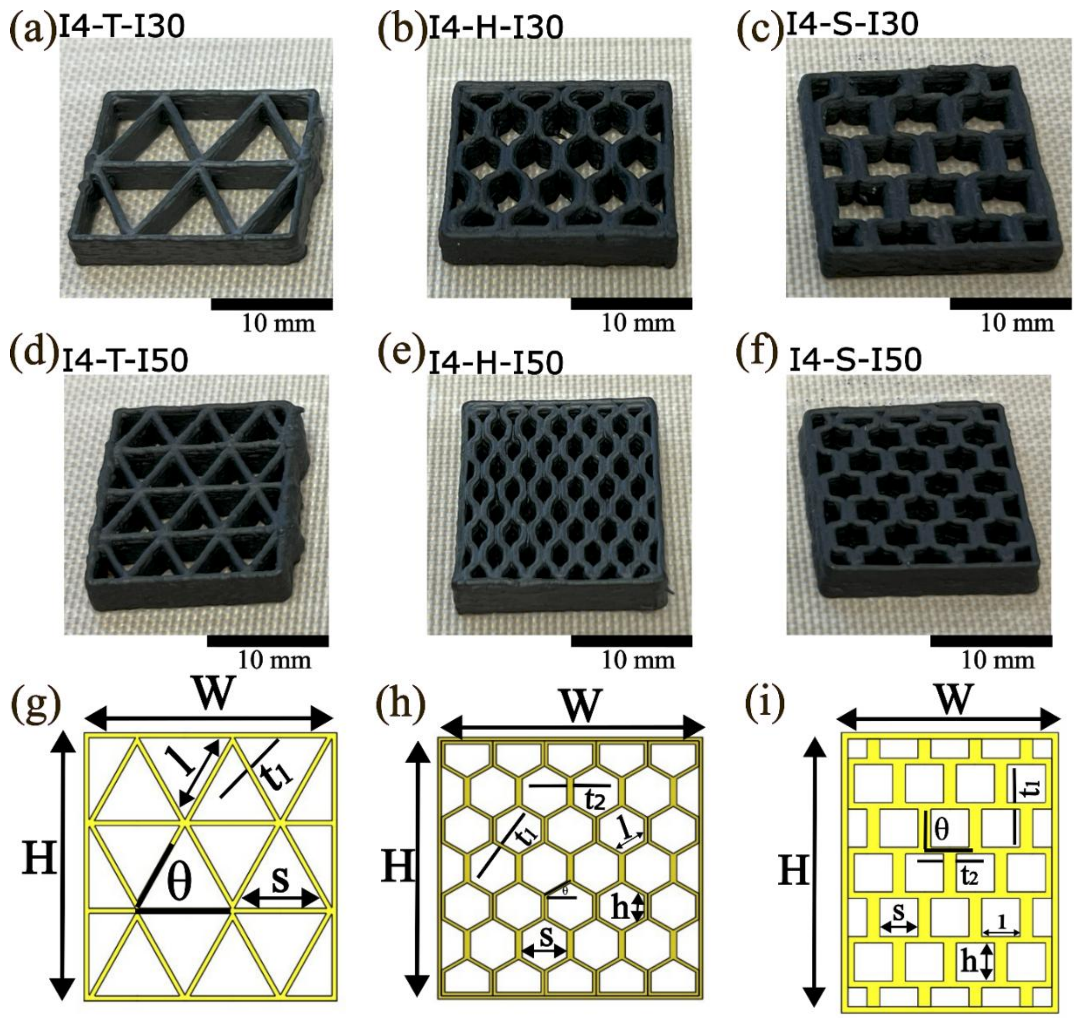

Figure 3. 2. Optical images of DIW-printed triangular, hexagonal, and square honeycomb cores using I4 at different infill densities: (a) I4-T-I30, (b) I4-H-I30, (c) I4-S-I30, (d) I4-T-I50, (e) I4-H-I50, and (f) I4-S-I50. Schematics in (g) - (i) illustrate geometric parameters of the core and unit cell.

Triangular cells with single-wall configurations generally display in-plane isotropy, while hexagonal and square cells with double-wall configurations exhibit in-plane anisotropy [8, 16]. Increasing the infill density reduces the cell size, enhances relative density, and improves crushing strength [90]. Additionally, the properties of the base material play a significant role in influencing the structural stability, shear strength, and compressive resistance of honeycomb cores [14, 91, 92]. In this study, relative densities of DIW-printed honeycomb structures were controlled by varying cell geometry, infill density, and base material composition, as depicted in figure 3.2. (a) – (f). The focus was on systematically analyzing the compressive properties of honeycomb structures fabricated with triangular (T), hexagonal (H), and square (S) cells, three infill concentrations (30%, 40%, and 50%), and four different base materials (I1-I4). The geometric parameters of the DIW-printed honeycomb specimens are shown in figure 3.2 (g) – (i). These include width (W), height (H), cell size (s), cell wall thicknesses (t_1 for inclined walls and t_2 for vertical walls), core density (ρ_h), relative density (ρ_r), density of base material (ρ_s) and cell wall angle (θ), as outlined in table S3.1. Also, overall thickness (T) is shown in table S3.1 (Supplementary Information 1). The nominal density (ρ_h) of the honeycomb structures was determined using the measured mass and volume of the specimens, based on their nominal dimensions, as shown in equation (3.3):

$$\rho_h = \frac{M}{WHT} \qquad (3.3)$$

Where M, W, H, and T are the nominal specimen mass, width, height, and thickness respectively. The density of the base material (ρ_s) was measured using a gas pycnometer (AccuPyc II 1340). A total of 108 specimens were tested, encompassing three replicates for each combination of infill density, cell geometry, and ink type. The specimens were categorized based on the type of ink, cell geometry, and infill density. For example, "I3-T-I40" denotes a triangular honeycomb core printed with Ink 3 at a 40% infill density.

This comprehensive approach ensures scalability and provides a robust understanding of the mechanical performance of DIW-printed honeycomb cores across diverse geometries, materials, and infill densities.

3.3.2. Evaluation of Surface Roughness in the DIW-Printed Core Structures

Surface roughness is a critical metric for evaluating print quality, particularly in assessing the uniform stacking of layers during DIW printing. Figure 3.3 (a) highlights the surface morphology of the peripheral skin of DIW-printed honeycomb cores (T, H, and S) post-printing and curing. The surface roughness of these cores, fabricated using different inks (I1–I4), was systematically compared with 3D-printed PLA and continuous fiber-reinforced thermoplastic composites. These comparisons address print-induced defects, including surface warping and voids, often caused by fiber stiffness and the repetitive heating-cooling cycles associated with fused filament fabrication (FFF) processes [93, 94].

Figures 3.3 (b) – (e) depict 200x magnification contour diagrams of the surface height profiles of DIW-printed honeycomb cores fabricated using inks I1–I4. These contours reveal peak-to-valley distances across the surface, indicating significantly lower roughness (0 to 133 µm) compared to 3D-printed PLA (-453.6 to 446.8 µm) and FFF carbon fiber-reinforced composites (-552.8 to 236.8 µm) [13]. This superior surface quality can be attributed to the consistent rheology of the DIW inks, the absence of print path overlaps, and the semi-elliptical cross-sectional geometry of the deposited filaments. These factors contribute to the smoother and more uniform surfaces of DIW-printed cores. Table 3.1 summarizes the average surface roughness (Sa) values measured across the entire surface. The data indicate that the S_a values for DIW-printed structures are significantly lower than the R_a values reported for 3D-printed PLA structures and are comparable to those observed in 3D-printed continuous carbon fiber-reinforced composites [13]. These findings underscore the capability of the DIW printing process to produce high-quality surfaces with minimal roughness, enhancing the structural integrity and performance of the printed honeycomb cores.

Table 3. 1. Surface roughness (S_a) measurements.

Honeycomb structures	Surface roughness Sa (um)	Surface roughness Ra (um) - PLA [13]	Surface roughness Ra (um) -Continuous fiber-reinforced thermoplastic composites [13]
I1-T/H/R-I30/40/50	21.42	32 ± 5.2	19 ± 2.6
I2-T/H/R-I30/40/50	24.54		
I3-T/H/R-I30/40/50	26.37		
I4-T/H/R-I30/40/50	30.74		

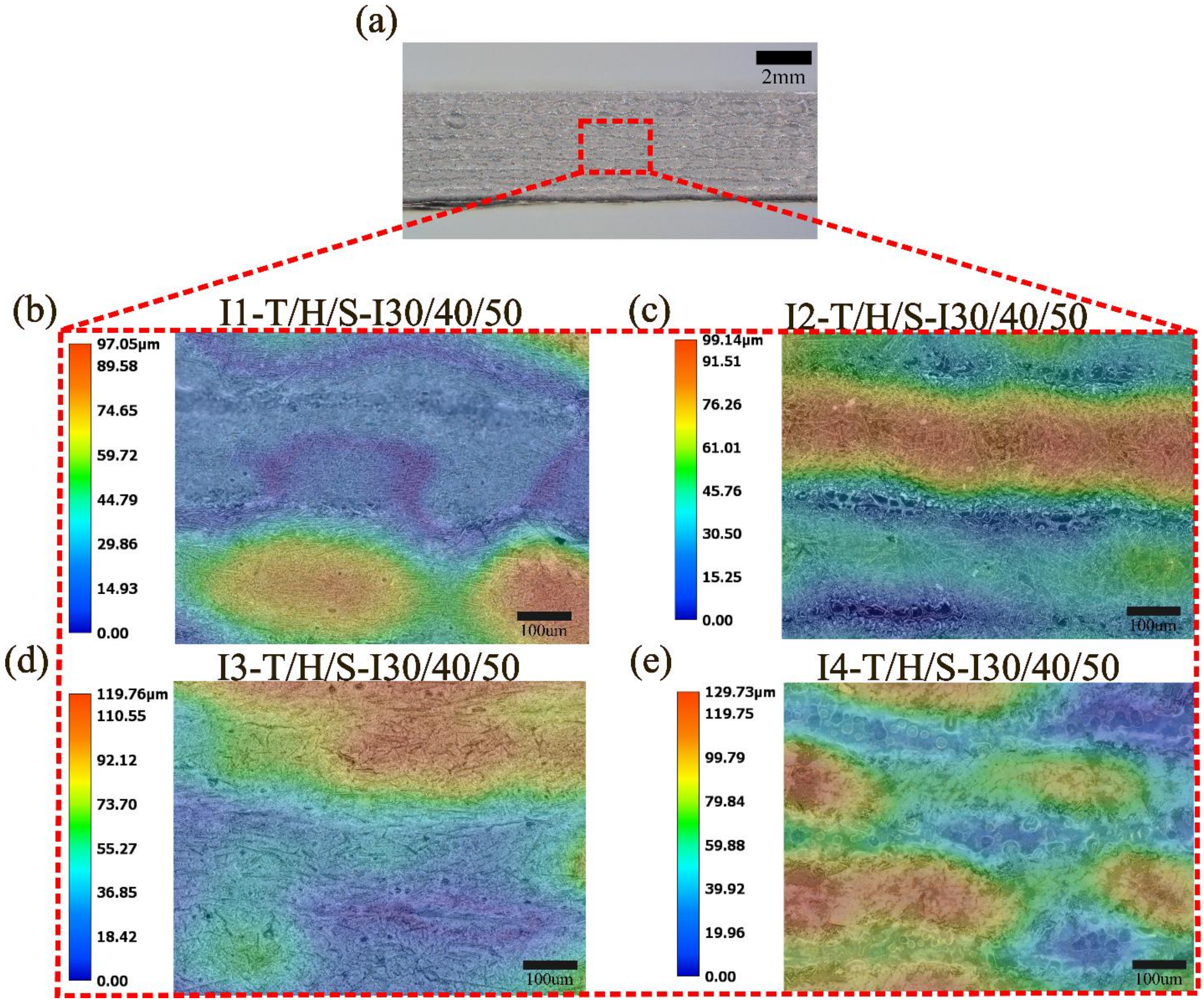

Figure 3. 3. Print quality evaluation of DIW-fabricated honeycomb composites: (a) Optical image of printed skin layers, (b) - (e) surface height contour maps of the DIW printed specimens fabricated using I1-I4.

This analysis method, adapted from previous studies [52], provides an objective framework for assessing the print quality of the DIW-printed structures. The results confirm the effectiveness of the DIW process in producing honeycomb cores with smooth surfaces without any print-induced defects such as print surface irregularities and warping, particularly when employing print-ready ink formulations and printing parameters.

3.3.3. In-plane Compression Properties of Honeycomb Cores

To assess the mechanical properties of DIW-printed honeycomb composite cores, in-plane compression tests were performed on specimens with triangular (T), hexagonal (H), and square (S) geometries. These cores were fabricated with varying infill densities (30%, 40%, and 50%) and base materials incorporating different carbon fiber contents (Inks I1–I4). The typical stress-strain curves, presented in figure 3.4 (a) – (c), exhibit a characteristic response: an initial peak stress followed by a decline due to cell wall buckling and brittle fracture. The corresponding fracture patterns are shown in figure 3.4 (d) – (f).

For triangular cores, fractures predominantly occurred at the inclined and horizontal cell walls across all infill densities, indicating structural weaknesses in these areas. Hexagonal cores demonstrated fractures primarily at the junctions of inclined and vertical walls, followed by a stress recovery phase due to the realignment of vertical walls, especially in specimens with higher infill densities. In square cores, progressive failure was observed, with stress drops corresponding to the sequential collapse of horizontal and vertical wall junctions.

The mechanical performance of DIW-printed cores improved significantly with increasing infill density and carbon fiber content in the base material. Figures 3.5 (a) – (f) show that higher infill densities resulted in enhanced relative density, reduced cell size, and an increased number of unit cells, leading to improved stiffness and strength. For instance, cores fabricated with I4 at 50% infill (I4-T-I50, I4-H-I50, and I4-S-I50) exhibited stiffness enhancements of 59%, 43%, and 47%, respectively, compared to their 30% infill counterparts. Similarly, their strength increased by 106%, 93%, and 162%, respectively.

The carbon fiber content in the base material also played a critical role in improving mechanical properties. Specimens fabricated with Ink I4 showed significant gains in stiffness and strength compared to those made with Ink I1. For example, I4-T-I50, I4-H-I50, and I4-S-I50 exhibited stiffness improvements of 70%, 13%, and 81% and strength enhancements of 49%, 36%, and 84% compared to their respective I1 counterparts. These trends were consistent across other geometries and infill densities (I30 and I40), demonstrating the reinforcing effect of carbon fibers in enhancing the structural performance of DIW-printed composite cores.

Hexagonal cores consistently outperformed triangular and square cores in both stiffness and strength, as shown in figures 3.5 (a) - (f). This superior performance stems from the unique structural configuration of hexagonal cores, where the periodic arrangement of inclined and vertical double cell walls (anisotropic in-plane core structure) with unequal cell wall lengths (Table S1) enhance load distribution and load-bearing capacity along the loading axis. As a result, hexagonal cores exhibit superior mechanical properties compared to triangular and square counterparts. For instance, the stiffness and strength of I3-H-I50 increased by 20% and 43% in stiffness and 96% and 135% in strength compared to I3-T-I50 and I3-S-I50, respectively. Similar trends are observed across different base materials (I1, I2, and I4), highlighting the mechanical advantages of hexagonal cores due to their combined cell wall configurations and load distribution.

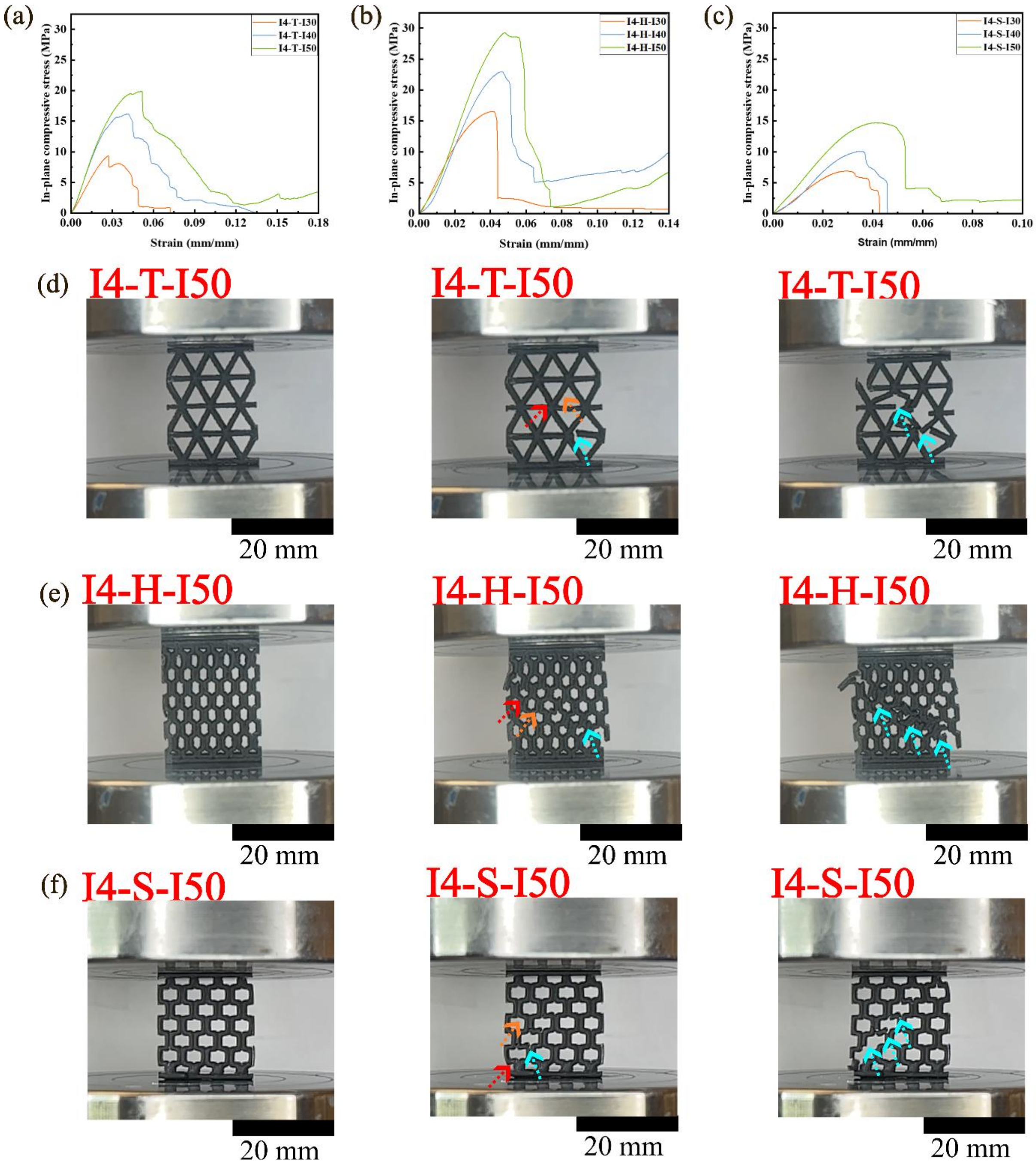

Figure 3. 4. In-plane compression behavior of DIW 3D-printed carbon fiber-reinforced honeycomb cores fabricated using I4: (a) - (c) stress-strain curves for triangular, hexagonal, and square cores. (d) - (f) Images show failure events of the composite honeycomb cores during in-plane compression testing: node rotation (red), cell wall buckling (orange), and brittle fracture

(blue). Stress-strain curves for triangular, hexagonal, and square cores made with I1–I3 are provided in the figure S3.1 (supplementary information 1).

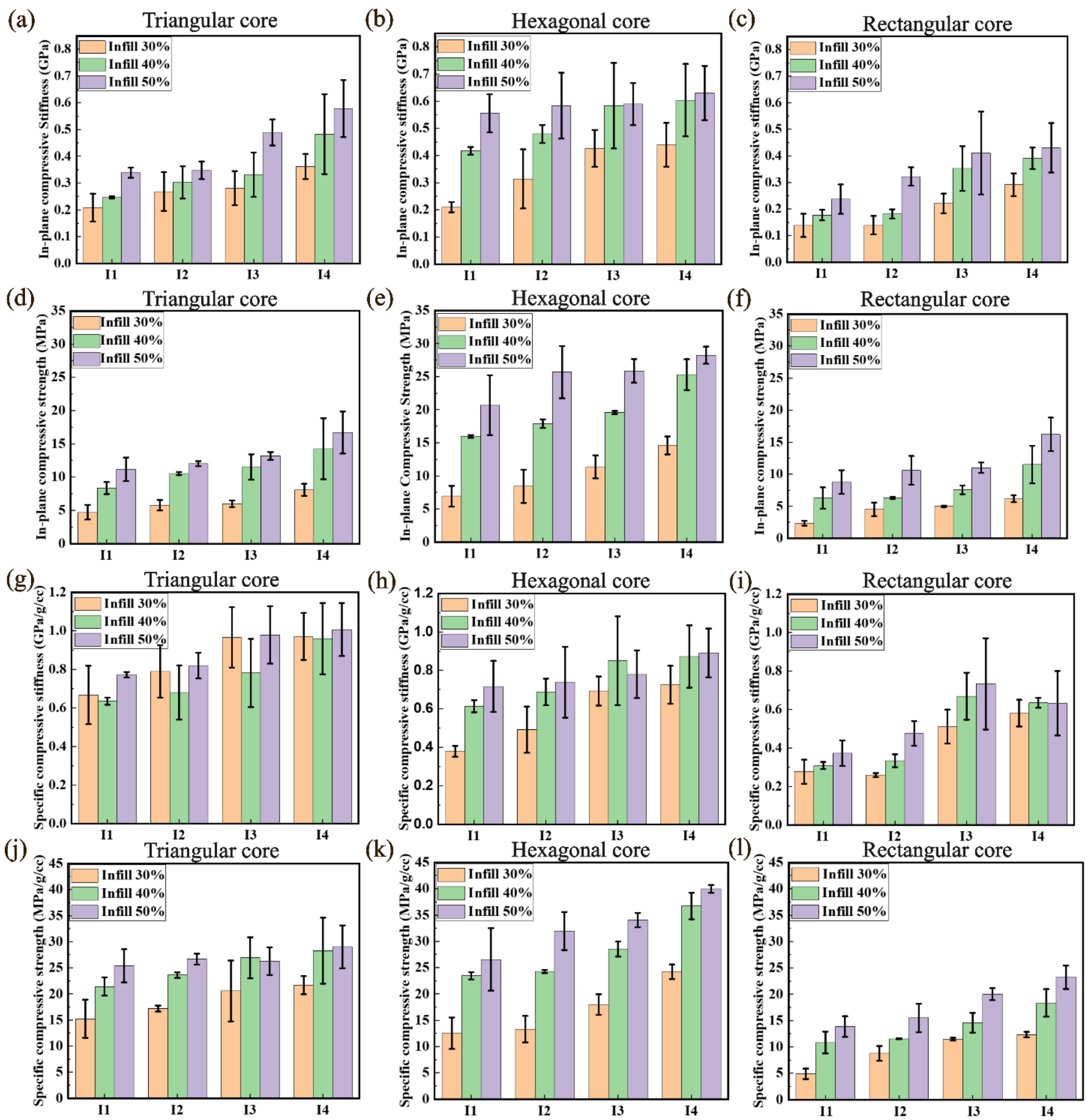

Figure 3. 5. In-plane compressive properties of DIW 3D-printed fiber-reinforced epoxy honeycomb cores with varying fiber content: (a) - (c) stiffness, (d) - (f) strength, (g) - (i) specific stiffness, and (j) - (l) specific strength for triangular, hexagonal, and rectangular cores.

The study also assessed the specific stiffness and strength of honeycomb cores, which are critical parameters for lightweight structural applications. As illustrated in figures 3.5 (h), (i), (k), and (l), specific stiffness and strength generally increased with higher infill densities. For instance, the I4-H-I50 and I4-S-I50 specimens exhibited 22% and 8% gains in specific stiffness, respectively, while achieving 65% and 88% improvements in specific strength compared to their 30% infill counterparts. However, these enhancements diminished as carbon fiber content increased from 10 wt.% to 40 wt.%, attributed to the corresponding rise in material density.

Triangular cores showed less consistent trends in specific stiffness (figure 3.5 (g)). For example, the I3-T-I30 specimen demonstrated 23% higher specific stiffness than I3-T-I40, indicating that while increasing infill density raises the overall density of the structure, it does not necessarily improve specific stiffness. This suggests that I3-T-I40 has a heavier build compared to I3-T-I30. Despite these anomalies, specific strength generally improved with increased relative density due to reduced cell size, except for minor deviations in some cases (figure 3.5 (h)). Overall, hexagonal and triangular honeycomb specimens demonstrate comparable specific stiffness and strength, both exceeding those of square honeycomb core specimens. Finally, the combined effect of cell geometry, higher infill density, and improved base material properties reinforces the potential of DIW-printed honeycomb cores for lightweight structural applications requiring high mechanical performance.

The stiffness (E) and strength (σ) of the triangular, hexagonal, and square honeycomb cores were evaluated and compared using classical cellular mechanics scaling laws [95], as outlined in equations (3.4) and (3.5).

$$E = B\left(\frac{\rho}{\rho_s}\right)^b E_s \tag{3.4}$$

$$\sigma = C\left(\frac{\rho}{\rho_s}\right)^c \sigma_s \tag{3.5}$$

The constants for the cores are as follows: for triangular cores, B = 1/3, b = 1, C = 1/3, and c = 1; for hexagonal cores, B = 3/2, b = 3, C = 1/3, and c = 2; and for square cores, B = 1/2, b = 1, C = 1/2, and c = 1. The parameters $E_s, \sigma_s,$ and ρ_s represent the stiffness, strength, and density of the base material, respectively. These values were determined through tensile testing of DIW-printed specimens fabricated using inks I1–I4, adhering to ASTM D638 Type-V standards.

Specimens were printed in a longitudinal (L) orientation to ensure fiber alignment along the loading direction during testing. The tensile test results, including scaling law values for $E_s, \sigma_s,$ and ρ_s, are summarized in table 3.2.

Table 3. 2. Summary of tensile test results.

Specimen name	Tensile Stiffness (E_s) (GPa)	Tensile Strength (σ_s) (MPa)	Density (ρ_s) (g/cc)
I1-L	1.08 ± 0.15	62.75 ± 1.55	1.1
I2-L	1.66 ± 0.12	73.57 ± 5.07	1.05
I3-L	2.00 ± 0.19	76.92 ± 2.80	0.89
I4-L	3.08 ± 0.17	85.94 ± 3.73	0.92

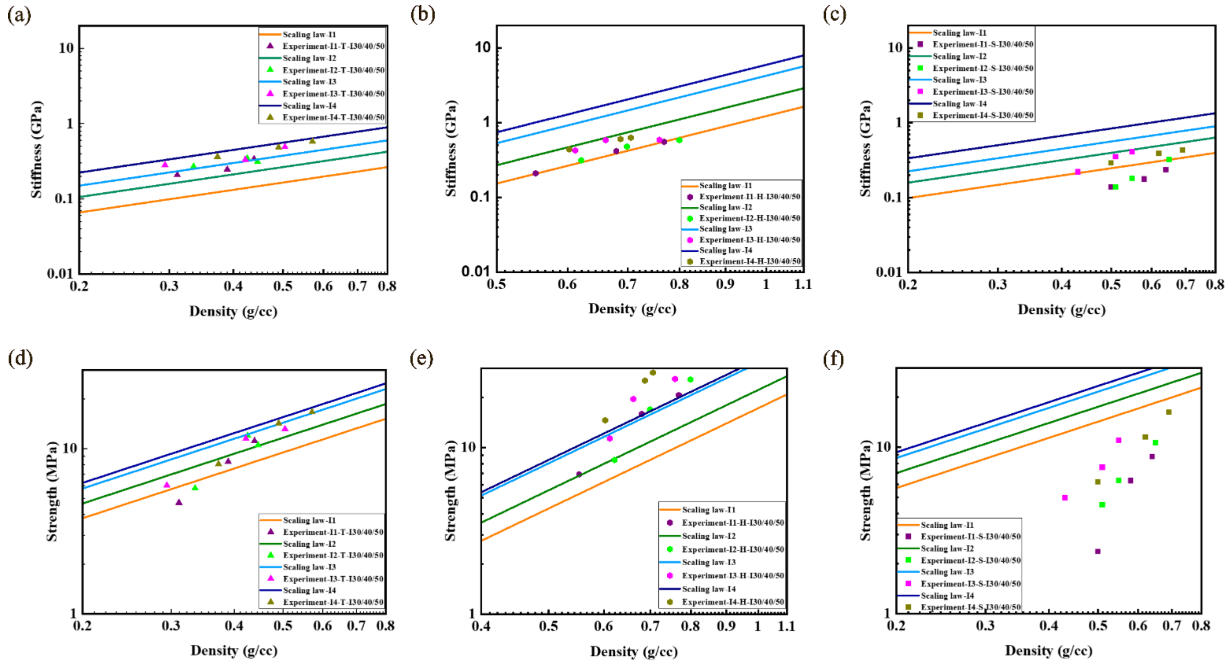

Figure 3. 6. Experimental vs. scaling law predictions for composite honeycomb structures: (a)-(c) stiffness and (d)-(f) strength as functions of density under in-plane compression of triangular, hexagonal, and square honeycomb cores.

Figure 3.6 (a) – (c) presents the experimentally determined stiffness of triangular, hexagonal, and square honeycomb cores, showing a close correlation with scaling law predictions for all structures fabricated using Inks 1–4. The strength measurements for triangular cores, depicted in figure 3.6 (d), also align well with scaling law predictions. However, hexagonal cores consistently surpass these predictions, as shown in figure 3.6 (e). This discrepancy arises from the structural design differences: triangular cores have a single-wall, in-plane isotropic configuration with angled fiber alignment (figure 3.7 (a)), while hexagonal cores possess a double-wall, in-plane anisotropic design where fibers remain aligned along the loading direction (figure 3.7 (b)), resulting in a significantly higher load-bearing capacity. In contrast, square honeycomb cores exhibit lower strength than scaling law predictions, as shown in figure 3.6 (f). This reduction in strength is attributed to the limited load-bearing capacity of the horizontal walls. Figure 3. 7 (c) further illustrates the in-plane anisotropy of the square cores, where fibers in the double walls are aligned with the load, while fibers in the horizontal walls, oriented perpendicular to the load, hinder effective load-bearing and distribution compared to hexagonal and triangular cores. All microstructures (figure 3.7 (a) – (c)) demonstrate strong fiber-matrix bonding, enhancing their mechanical performance. This bonding is notably superior to honeycombs printed with continuous carbon fiber-reinforced thermoplastics, which often suffer from poor fiber impregnation [92].

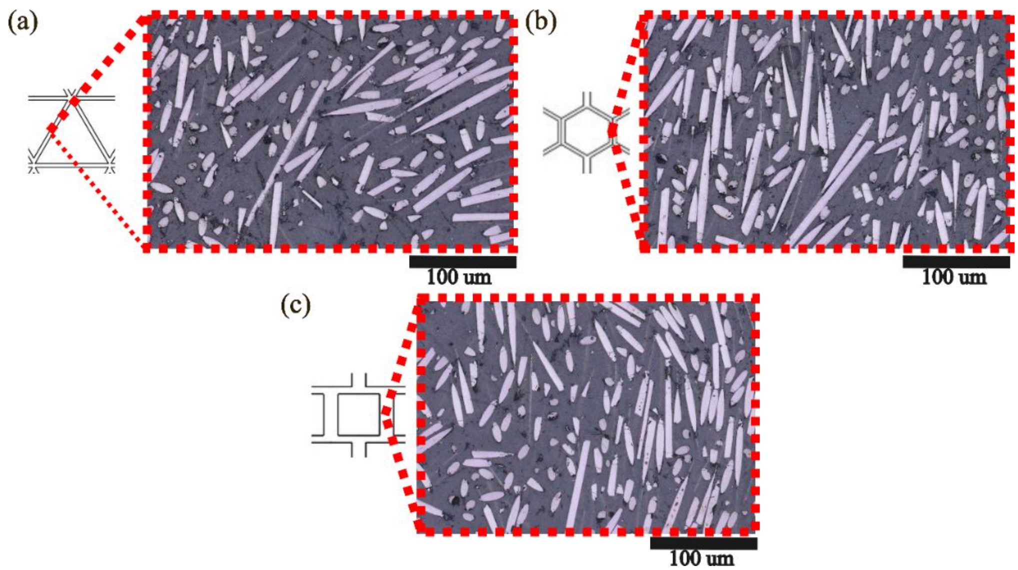

Figure 3. 7. Optical microscopy images of carbon fiber alignment in cell walls for (a) triangular, (b) hexagonal, and (c) square honeycomb cores.

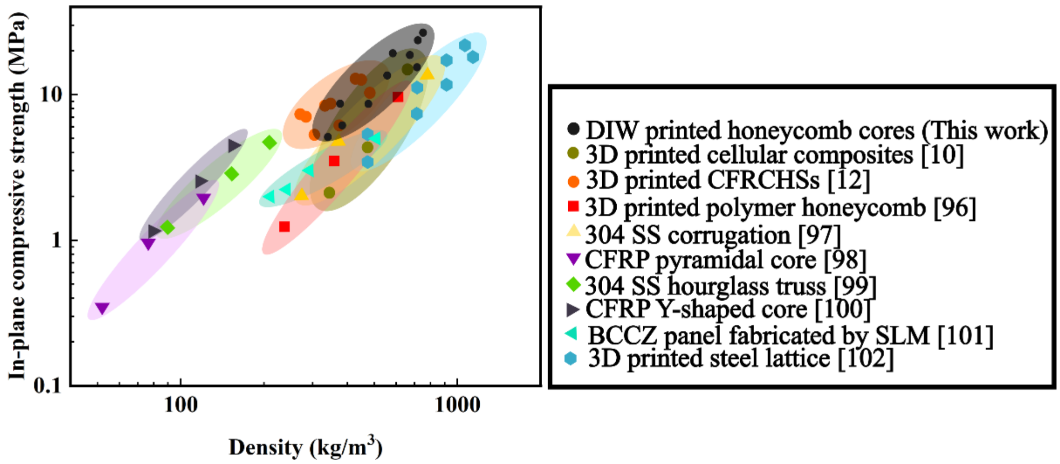

Figure 3. 8. In-plane compressive strength comparison of DIW-printed carbon fiber-reinforced honeycomb structures with other honeycomb designs.

The in-plane mechanical strength of honeycomb structures with various core architectures, fabricated using DIW 3D printing, was compared to honeycombs produced through different manufacturing techniques and materials. As illustrated in figure 3.8, DIW-printed honeycomb cores demonstrate superior in-plane compressive strength compared to DIW-printed cellular structures [10], 3D-printed continuous fiber-reinforced composite honeycombs (CFRCHSs) [12], polymer-based honeycombs [96], 304 stainless steel corrugated cores [97], carbon fiber-reinforced plastic (CFRP) pyramidal cores [98], 304 stainless steel hourglass trusses [99], CFRP Y-shaped cores [100], BCCZ panels fabricated via selective laser melting (SLM) [101], and 3D-printed steel lattices [102]. In addition to their enhanced mechanical performance, the DIW-printed hexagonal honeycombs exhibit a significantly lower density compared to 3D-printed steel lattices. This combination of lightweight properties and high in-plane strength highlights their potential for applications demanding structurally efficient, high-performance materials.

3.4. Chapter Conclusion

In summary, this chapter highlights the ability of the previously designed and developed multi-material, carbon fiber-reinforced viscoelastic inks (10–40 wt.% fiber content) with customized rheological properties (chapter 2) to facilitate the rapid and precise DIW 3D printing of high-quality honeycomb composites featuring various core designs. These inks facilitated superior print quality, tunable mechanical properties, and consistent fiber-matrix bonding, outperforming prior work on 3D-printed fiber-reinforced epoxy composites, continuous carbon fiber-reinforced thermoplastics, and metal-based cellular structures. Using this innovative ink formulation and DIW technique, honeycomb structures with varying core configurations, cell geometries, sizes, and densities were fabricated, achieving exceptional surface finish and shape fidelity compared to 3D-printed PLA and continuous fiber-reinforced composites. In-plane compression tests revealed performance trends driven by core geometry, base materials, and infill densities. Compressive stiffness and strength increased with higher infill, smaller cell sizes, customized geometries, and greater relative density. Ink formulations incorporating customized carbon fiber content further enhanced mechanical properties. Specific compressive strength improved with increased infill and base material properties. Among core designs, hexagonal honeycombs exhibited superior mechanical and specific properties, outperforming triangular and square counterparts. While stiffness results for all core geometries aligned with scaling laws, hexagonal cores exceeded strength predictions. Overall, the DIW-printed honeycomb structures demonstrated exceptional compressive performance, highlighting the potential of viscoelastic inks and DIW 3D printing for producing high-performance, customizable composite honeycombs suitable for lightweight structural applications.

Chapter 4: Out-of-Plane Compression and Energy Absorption of Carbon Fiber-Reinforced Epoxy Honeycomb Cores with Diverse Geometric Configurations fabricated via Direct Ink Writing (DIW)

4.1. Introduction

Honeycomb structures, known for their exceptional specific stiffness and strength under out-of-plane (axial) loading [16, 103-105], have garnered significant attention in various industries, including aerospace, marine, sports, and transportation [4-7], due to their low density, high energy absorption capacity, and excellent thermal insulation properties [103, 106, 107]. The macroscopic performance of these structures can be customized through fabrication methods [8-11, 35], geometry [12, 13], microstructure [10], and material selection [14, 15]. Typically, honeycomb cores are designed to convert external work into internal energy via deformation, making them ideal for energy absorption applications [16]. Materials such as metals [17], ceramics [108], polymers [109], and composites [8, 10] have been used to fabricate honeycomb cores, with fiber-reinforced composites (FRCs) offering lightweight, customizable properties and superior flexibility. Conventional manufacturing techniques, such as hot press molding, interlocking assembly, and vacuum-assisted resin infusion [110-113], have enabled the fabrication of various honeycomb topologies but are often constrained by high costs, geometry-specific molds, and limited automation.

Additive manufacturing (AM), particularly 3D printing, has revolutionized the production of honeycomb structures, offering extensive design freedom, geometric complexity, and material customization [49, 114-116]. Fused Filament Fabrication (FFF), a popular AM technique, has been extensively studied for producing polymer honeycombs. However, FFF-printed components often suffer from inadequate mechanical properties, limited energy absorption efficiency, and challenges in incorporating reinforcing fibers [117, 118].

Recent advances in 3D printing have focused on continuous fiber-reinforced thermoplastic composite (CFRTPC) structures, employing co-extrusion [12, 46, 86, 87], fiber tensioning [13], and free-hanging methods [79]. Despite improvements, these techniques face challenges such as poor fiber-matrix bonding, inter-layer voids, and limited energy absorption performance [48, 63, 86]. Furthermore, research on short fiber-reinforced thermoplastic honeycombs remains limited due to insufficient mechanical and energy-absorbing capabilities arising from poor fiber-matrix interaction [15, 76].

Direct Ink Writing (DIW), an emerging AM technique, offers unique advantages for fabricating lightweight, intricate cellular structures with tailored material properties [10, 36, 37, 41, 44, 45, 80, 83, 119]. DIW enables the extrusion of concentrated viscoelastic inks with shear-thinning behavior, maintaining shape fidelity post-extrusion. While DIW has been used to produce polymeric scaffolds and functional structures [120-122], its application in fabricating carbon fiber-reinforced epoxy honeycombs with superior out-of-plane performance remains underexplored.

This study utilizes epoxy-based viscoelastic inks containing carbon fiber and silica fillers as outlined in chapter 2 for DIW 3D printing of biomimetic cellular composites. The inks exhibit tunable rheological properties, enabling the fabrication of lightweight honeycomb structures with diverse cell geometries (hexagonal, square, triangular), infill percentages (I30, I40), and material formulations (I1, I2, I3, I4). A comprehensive analysis of print quality, deformation modes, and energy absorption characteristics highlights the superior performance of DIW-printed honeycombs compared to conventional methods. The results underscore the potential of DIW and tailored inks to advance lightweight structural applications, offering unparalleled flexibility in design and fabrication.

4.2. Experimental

4.2.1. DIW Printing of Honeycomb Structures

The scalability of inks (I1-I4) was validated by DIW printing hexagonal (H), square (S), and triangular (T) honeycomb structures with 30% and 40% infill (figure 4.1 (a) – (c)). These cellular structures exhibit mechanical properties influenced by cell geometry [8], infill density [90], and base material [15]. Triangular cores offer in-plane isotropy [90, 123], while hexagonal and square cores exhibit anisotropy [16, 123]. Higher infill density increases relative density and strength [90], while base material properties impact stability, shear strength, and compressive resistance [14, 91, 92].

The geometric parameters of DIW-printed honeycomb cores are illustrated schematically in figure 4.1 (a) – (c) and include width (W), length (L), cell size (s), wall thicknesses (t_1, t_2), core density (ρ_h), relative density (ρ_r), base material density (ρ_s), cell wall angle (θ), and overall thickness (T), as detailed in table S4.1 (Supplementary Information 2). Multilayered honeycomb structures with varying cell geometries and infill percentages were fabricated using customized G-code, ensuring precise print control. Infill variations affected cell size and density, and the interplay between geometry, infill, and base material influenced mechanical and energy absorption properties [16, 28, 89, 105, 123, 124].

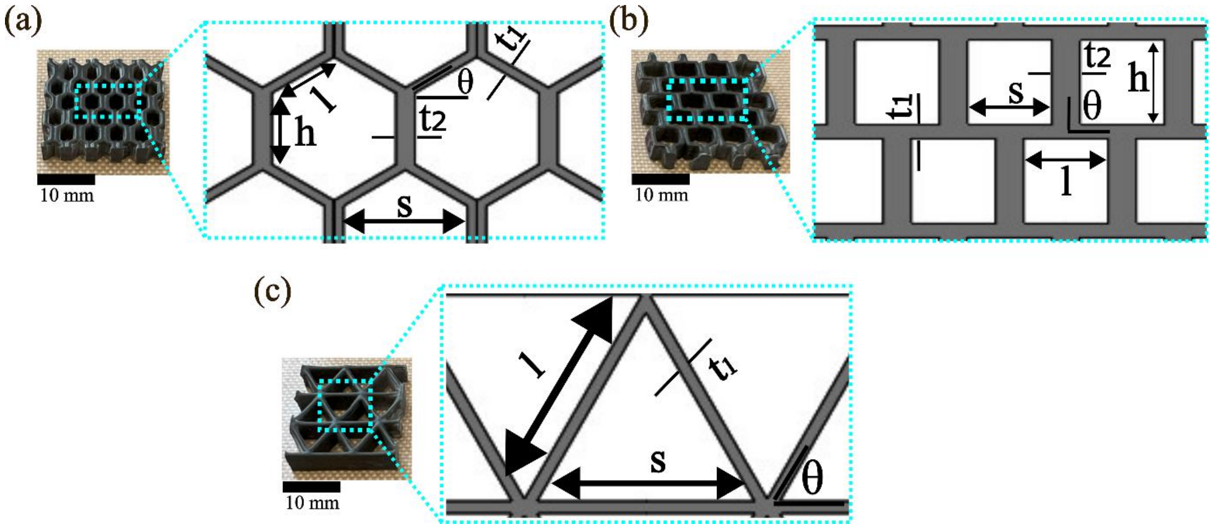

Figure 4. 1. Optical images of DIW-printed and cured carbon fiber-reinforced honeycomb composite cores: (a) hexagonal, (b) square, and (c) triangular designs using I4, with schematics showing unit cell geometric parameters.

Printing was performed on a custom DIW pneumatic printer using a Nordson syringe as the dispensing unit, with inks loaded into 10 cc syringes, degassed, and extruded through 410 µm (I1, I2) and 580 µm (I3, I4) nozzles at 10 mm/min under 4-10 psi. Designs and print paths were generated in SOLIDWORKS, Repetier-Host, and Slic3r, with G-code modifications enhancing print continuity. Unlike single-stroke paths in continuous fiber printing [13, 86], this DIW process enables complex geometries. Printed specimens were pre-cured at room temperature (8 h) and post-cured at 82 °C (8 h) to ensure strong interlayer bonding and prevent failure typical in FFF structures [12, 88]. A 0.410/0.580 mm layer height resulted in 3.85-4.25 mm thick honeycomb cores after 10 cycles.

Honeycomb specimens were classified by ink type (I1–I4), cell geometry (hexagonal "H", square "S", triangular "T"), and infill (30% "I30", 40% "I40"). For instance, I1-H-I30 represents a hexagonal honeycomb printed with Ink 1 at 30% infill. Each ink variant included 18 specimens (3 geometries × 2 infill levels × 3 replicates), totaling 72 specimens (18 × 4 inks) tested in this study.

4.2.2. Out-of-Plane Compression Testing

DIW-printed honeycomb structures with varying topologies and cell configurations underwent quasi-static out-of-plane compression tests to assess their crushing behavior, deformation, and load-displacement response. These tests quantified crashworthiness parameters, including total energy absorption (EA), specific energy absorption (SEA), peak crushing force (PCF), and crushing force efficiency (CFE).

Compression tests were conducted using an MTS 810 universal testing machine with a 100 kN load cell. Specimens were compressed to 80% of their original height at a displacement rate of 1 mm/min. Nominal compressive stress (σ) and strain (ε) were calculated using the following equations (4.1) and (4.2):

$$\sigma = \frac{F}{A} \qquad (4.1)$$

$$\varepsilon = \frac{\delta}{H} \qquad (4.2)$$

where F is the crushing force, A is the nominal cross-sectional area, δ is the displacement, and H is the initial specimen height.

Total energy absorption (EA) was computed by integrating the force-displacement curve (equation (4.3)):

$$EA = \int_a^b F.d\delta \qquad (4.3)$$

where a = 0 and b marks the densification onset. Specific energy absorption (SEA) was calculated as the ratio of total energy absorption to specimen mass (m) (equation (4.4)):

$$\mathrm{SEA} = \frac{\mathrm{EA}}{\mathrm{m}} \qquad (4.4)$$

Crushing force efficiency (CFE) was determined as the ratio of mean crushing force (MCF) to peak crushing force (PCF) (equation (4.5)):

$$CFE = \frac{MCF}{PCF} \qquad (4.5)$$

The MCF is defined as (equation (4.6)):

$$MCF = \frac{1}{\delta_b}\int_a^b F.d\delta \qquad (4.6)$$

The PCF represents the maximum force on the load-displacement curve prior to the onset of densification.

The effective density (ρ_h) of the honeycomb specimens was calculated using the equation (4.7). The density of the base materials (ρ) was measured using a gas pycnometer, specifically the AccuPyc II 1340.

$$\rho_h = \frac{M}{LWT} \qquad (4.7)$$

where M, L, W, and T represent the mass, length, width, and thickness of the specimens, respectively. The relative density (ρ_r) of the honeycomb structures was determined using the following equation (4.8):

$$\rho_r = \frac{\rho_h}{\rho} \qquad (4.8)$$

where ρ_h is the density of the honeycomb specimen, and ρ_r is the density of the base material.

4.2.3. Imaging

To analyze the microstructure, including print-induced fiber alignment, specimens were embedded in acrylic epoxy resin, polished with SiC grit papers (800–4000), and finished with 3 μm and 1 μm diamond slurries using a Struers Labopol 5 polisher. Samples were then sonicated in deionized water, degreased with ethanol and methanol, dried at 60°C for 24 hours, and imaged using the same microscope.

4.3. Results and Discussion

4.3.1. Out-of-Plane Compression Behavior and Energy Absorption of Honeycomb Cores

The typical stages of experimental out-of-plane compression tests for DIW-printed fiber-reinforced epoxy composite honeycomb cores, including hexagonal (H), square (S), and triangular (T) specimens, are illustrated in figure 4.2 (a) – (c). During testing, all cell walls initially bear the compressive load uniformly, with failure typically initiating through axial or buckling deformation, followed by densification.

The force-displacement and nominal stress-strain responses of honeycomb specimens made from different base materials (I1–I4) are shown in figure 4.2 (d) – (i). These curves generally exhibit three distinct deformation stages: initial elastic deformation (O–A), plateau stage (A–B), and densification (B–C). The elastic stage (O–A) corresponds to the linear axial deformation of honeycomb walls at the onset of compression. The plateau stage (A–B) follows once the compressive load reaches the walls' load-bearing capacity, leading to wall collapse through brittle fracture or buckling while maintaining relatively steady stress. The densification stage (B–C) occurs when cell walls fully collapse, causing a sharp stress increase with minimal additional deformation.

Figure 4.2 (d) – (i) highlights that hexagonal and square honeycomb cores exhibit higher load and stress bearing capacities compared to triangular cores due to their geometric configurations. Hexagonal (six sides) and square (four sides) cores feature periodic double walls and stronger surface contacts between adjacent walls, enhancing their structural stability and strength. Conversely, triangular cores (three sides) rely on limited line contacts between walls, making them structurally weaker. Additionally, figure 4.2 (d) – (f) shows improved load-bearing capacity across all core variants fabricated with I1–I4 as infill increases from 30% to 40%, due to reduced cell size and increased wall density.

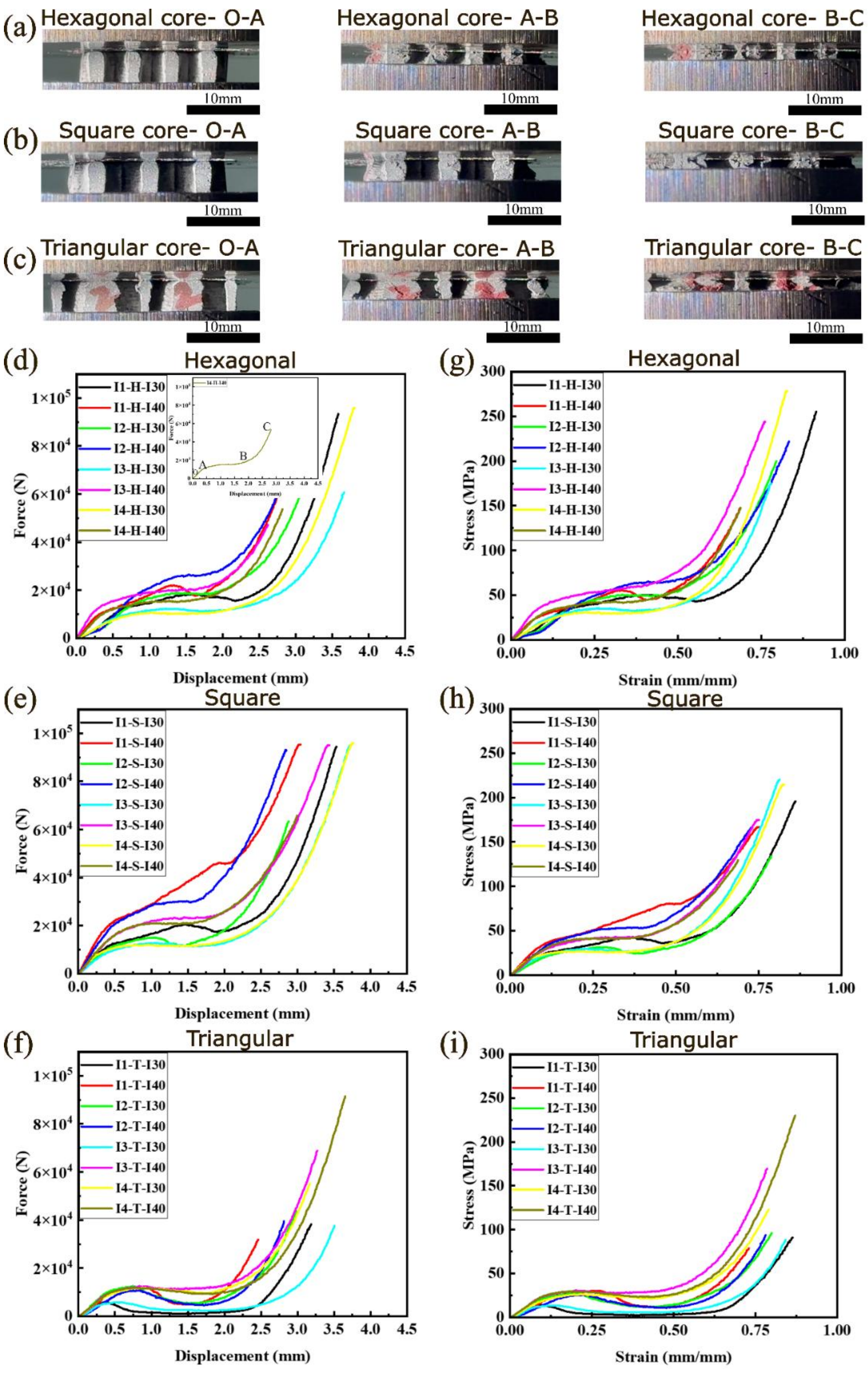

Figure 4. 2. Out-of-plane compression testing of DIW 3D-printed carbon fiber-reinforced epoxy composite honeycomb cores (H, S, and T) fabricated using I4: Images illustrates (a) - (c) elastic

deformation (O-A), plateau stage (A-B), and densification (B-C) during testing. Similar behavior was demonstrated by specimens fabricated using I1-I3. Post-testing images of hexagonal, square, and triangular cores are provided in the figure S4.1 (supplementary information 2). (d) - (i) Force-displacement and stress-strain curves for hexagonal, square, and triangular cores fabricated using I1-I4 with infill 30% and 40%. Insert showing different stages of deformation in the force-displacement curves.

Failure modes also vary with geometry and base materials. Hexagonal and square cores predominantly fail via axial deformation, whereas triangular cores exhibit both buckling and axial deformation depending on infill concentration, base material, and wall thickness. For example, triangular honeycomb cores with I1–I2 at 30% and 40% infill show buckling failure, while those fabricated with I3–I4 fail through axial deformation. The presence of voids in I3–I4 specimens further influences force and stress curves, reducing wall strength and affecting deformation resistance.

The initial and progressive compressive forces required for hexagonal, square, and triangular cores made with I3–I4 are comparable to or lower than those with I1–I2 due to voids (figure S4.2-Supplementary Information 2). These voids negate the benefits of higher carbon fiber content in I3–I4 cores, lowering wall strength and deformation resistance under out-of-plane compression.

Overall, square and hexagonal cores demonstrate higher crushing forces and strengths than triangular cores due to their geometric design, which provides more bonding surfaces and structural reinforcement. Among these, hexagonal cores exhibit slightly lower crushing forces than square cores due to their combination of inclined and horizontal walls. Triangular cores show the weakest crushing force and strength due to their reliance on unstable line contacts, leading to premature failure.

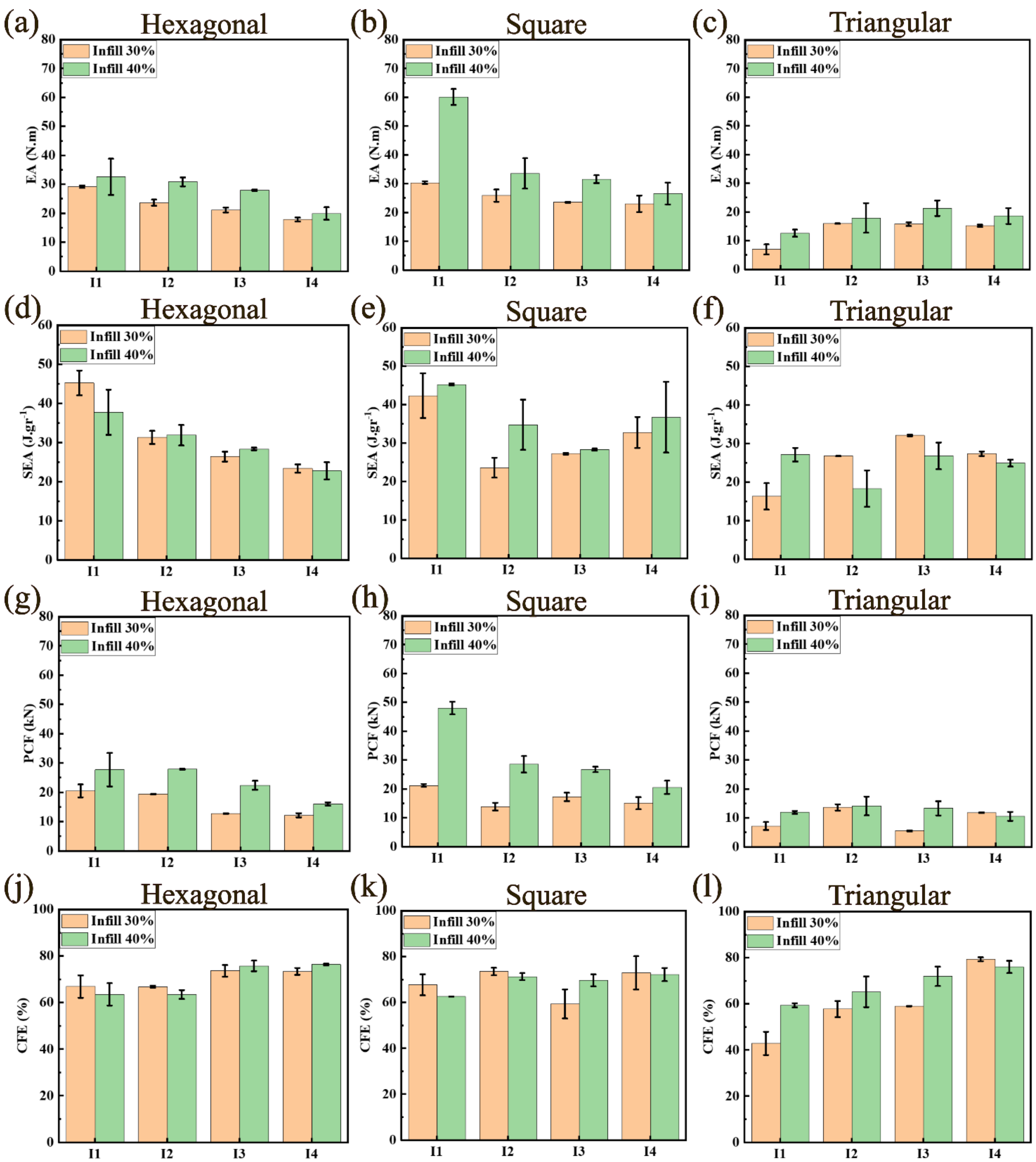

Figure 4. 3. Comparison of the crashworthiness parameters of DIW-printed carbon fiber-reinforced honeycomb cores (hexagonal, square, triangular) with 30% and 40% infill under out-of-plane compression: (a) - (c) total energy absorption (EA), (d) - (f) specific energy absorption (SEA), (g) - (i) peak crushing force (PCF), and (j) - (l) crushing force efficiency (CFE).

DIW-printed discontinuous fiber-reinforced honeycomb structures have potential applications in energy absorption systems. While higher densities enhance structural strength, they may reduce weight efficiency. Therefore, optimizing honeycomb parameters is crucial for achieving high energy absorption while maintaining minimal weight, meeting the requirements for advanced lightweight structural designs. In this study, crashworthiness parameters such as EA, SEA, PCF, and CFE were derived from force-displacement curves. The crashworthiness performance metrics for all DIW-printed honeycomb specimens are presented in figure 4.3 (a) – (l). Figure 4.2 (d) – (f) indicates that densification begins at compressive deformations of 2–2.25 mm for hexagonal cores, 2–2.15 mm for square cores, and 2.25–2.5 mm for triangular cores fabricated with I1–I4 at 30% and 40% infill.

As shown in figure 4.3 (a) – (c), EA increases for hexagonal, square, and triangular cores fabricated with I1–I4 as infill rises from 30% to 40%, due to additional walls and increased mass. For example, cores made with I1 show EA increases of 11.7% (hexagonal), 98% (square), and 80.8% (triangular) as infill concentration increases. However, EA for hexagonal and square cores decreases across I1–I4 due to voids, which reduce load-bearing capacity and diminish carbon fiber reinforcement effects. Interestingly, triangular cores show an EA improvement trend, likely due to differences in nozzle size (0.410 mm for I1 and I2 vs. 0.58 mm for I3 and I4), affecting wall thickness and energy absorption.

Figure 4.3 (d) – (f) presents SEA values, which measure energy absorption per unit mass. Hexagonal cores exhibit similar or slightly lower SEA with increasing infill across I1–I4 due to mass increase. Square cores show an SEA increase with higher infill, as the energy absorption rise outweighs the mass gain. I1 specimens with 30% and 40% infill exhibit higher SEA than square cores made with I2–I4. Triangular cores with I2–I4 at 30% infill display higher SEA than those at 40% due to their lower mass. However, triangular cores with I1 at 30% infill show a 66.4% SEA decrease compared to 40% infill, attributed to buckling-induced wall collapse.

Figure 4.3 (g) – (i) shows that all DIW-printed composite cores exhibit increased PCF with higher infill for I1–I4 due to greater mass and improved load distribution. Hexagonal and square cores fabricated with I1 at 30% and 40% infill exhibit higher PCF compared to I2–I4 counterparts, likely due to reduced wall strength in I2–I4 caused by voids. Triangular cores made with I2 show higher PCF than those made with I1, I3, and I4 due to fewer voids and relatively thicker walls.

CFE, which characterizes compressive force uniformity, is another key crashworthiness parameter. Higher CFE values minimize acceleration variations and structural damage. Figure 4.3 (j) – (l) indicates moderate to high CFE values: 59–76 for hexagonal cores, 59–73 for square cores, and 42–79 for triangular cores fabricated with I1–I4. Notably, DIW-printed fiber-reinforced epoxy honeycomb structures demonstrate comparable or superior SEA and CFE values relative to honeycombs made from neat thermoplastics, discontinuous fiber-reinforced thermoplastics, and continuous fiber-reinforced epoxy composites.

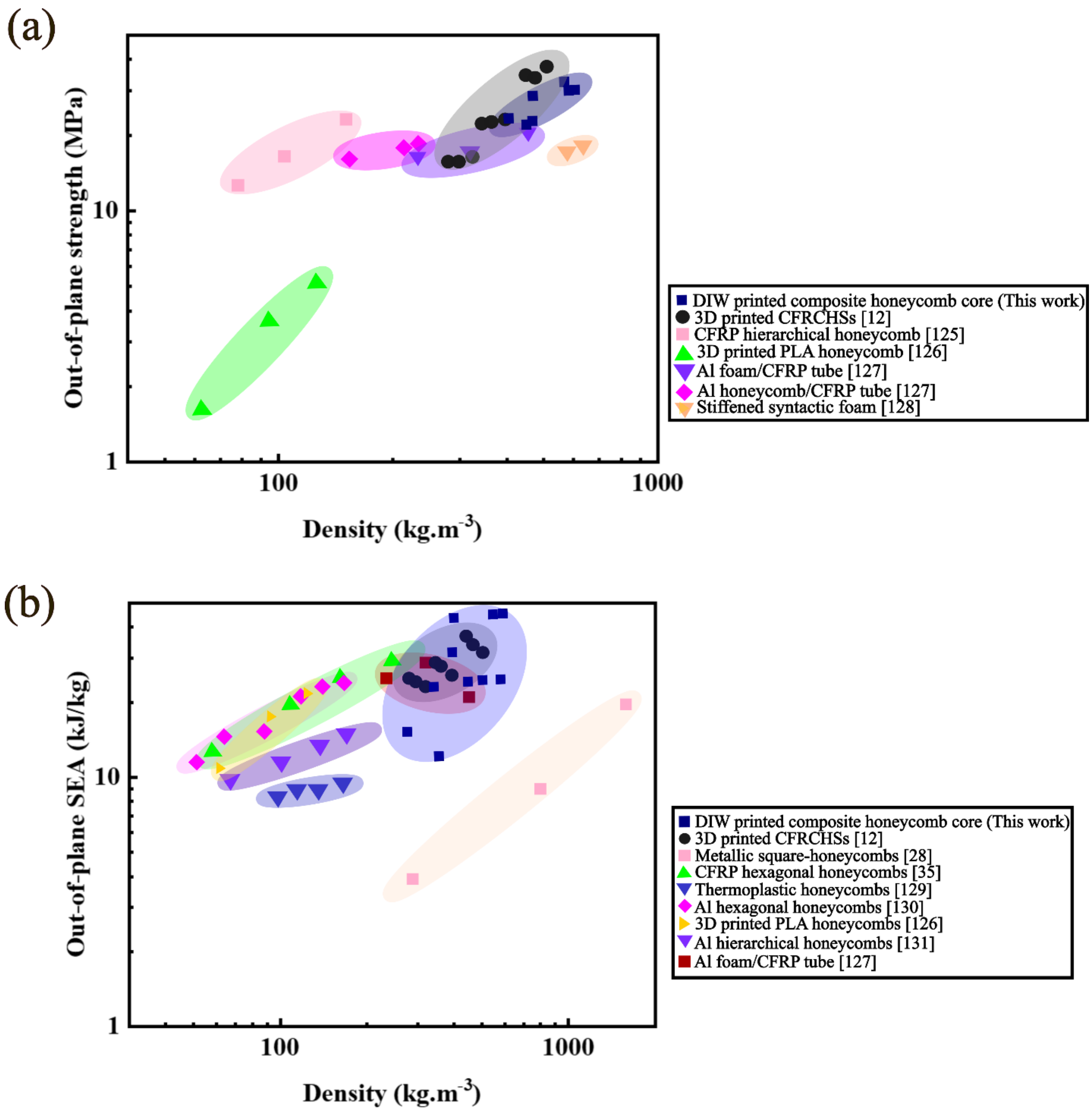

Figure 4. 4. Comparison of out-of-plane compression properties of DIW-printed fiber-reinforced epoxy honeycombs with other cellular designs: (a) Strength, and (b) SEA.

Finally, comparing DIW-printed honeycomb structures with cellular topologies fabricated via different methods offers valuable insights. Figure 4.4 (a) – (b) contrasts the out-of-plane compression strength and SEA of DIW-printed honeycombs with various cellular designs, including 3D-printed CFRCHSs [12], CFRP hierarchical honeycombs [125], 3D-printed PLA honeycombs [126], Al foam-filled CFRP tubes [127], Al honeycomb-filled CFRP tubes [127], stiffened syntactic foam [128], metallic square-honeycombs [28], CFRP hexagonal honeycombs [35], hierarchical thermoplastic honeycombs [129], Al hexagonal honeycombs [130], and Al hierarchical honeycombs [131].

DIW-printed fiber-reinforced epoxy composites outperform 3D-printed PLA honeycombs in compression strength and SEA, demonstrating their potential in lightweight, high-strength energy absorption structures. Although their density is relatively higher than traditional CFRP, thermoplastic, and aluminum honeycombs, their exceptional strength and SEA make them viable candidates for energy absorption applications. Notably, DIW-printed cores show comparable strength and higher SEA than 3D-printed CFRCHSs, highlighting their potential as an alternative to continuous carbon fiber honeycomb cores.

4.4. Chapter Conclusion

This study investigated the out-of-plane compressive behavior and energy absorption characteristics of honeycomb cores fabricated using short carbon fiber-reinforced epoxy composite viscoelastic inks, formulated with print-ready rheological properties for DIW 3D printing. Hexagonal, square, and triangular honeycomb cores with carbon fiber content ranging from 10–40 wt.% were successfully printed. The study also assessed shape fidelity, surface roughness, print-induced fiber alignment, and fiber-matrix bonding to evaluate print quality. Comparisons with existing literature on 3D-printed neat thermoplastic and continuous fiber-reinforced PLA honeycombs demonstrated that engineered inks (I1–I4) and the DIW technique enabled superior print quality, customizable geometries, and tailored infill configurations (30% and 40%).

Out-of-plane compression tests revealed performance trends based on base material, infill level, and geometric design. Hexagonal, square, and triangular cores fabricated with I3–I4 exhibited comparable or lower initial and progressive compressive forces than I1–I2 cores due to voids. Square and hexagonal cores showed higher crushing forces and strengths than triangular cores due to their more stable geometric configurations. Increased infill enhanced the energy absorption capacity of all honeycomb cores. Crashworthiness analysis indicated that EA increased with infill from 30% to 40%, while hexagonal, square, and triangular cores exhibited comparable strength, SEA, and CFE to literature values. These results highlight the potential of DIW-printed fiber-reinforced composite honeycomb cores for lightweight, high-performance energy absorption applications in industries such as automotive, aerospace, maritime, construction, and sports.

Chapter 5: Experimental Investigation and Characterization of 3D-Printed Short Carbon Fiber-Reinforced Epoxy Composite Sandwich Structures with Tailored Core Geometries

5.1. Introduction

Sandwich structures, a class of laminated composites, consist of two thin, high-strength face sheets separated by a lightweight periodic honeycomb or foam core. This configuration enhances shear stiffness, increases the moment of inertia, and significantly improves bending stiffness without adding substantial weight. Owing to their superior performance over conventional monolithic materials, sandwich structures are widely used in aerospace, automotive, naval, biomedical, civil, and sporting industries. Their advantages include high specific stiffness [91, 132] and strength [32], effective energy dissipation [133], microwave absorption [134], thermal insulation [135], noise reduction, and active cooling [136]. Inspired by natural structures such as bird wings, plant stems, and the human skull, researchers continue to develop bioinspired cellular composites that exhibit superior mechanical properties compared to their natural counterparts [10, 137].

The mechanical performance of sandwich structures is influenced by several factors, including core geometry [13, 138], cell dimensions [8, 13], wall thickness [8], and anisotropic properties [9]. The choice of materials, ranging from metals [17, 138] and ceramics [108] to polymers [109] and composites [8, 11], further determines their structural behavior. Among these, fiber-reinforced composites (FRCs) are particularly attractive due to their lightweight nature, tunable mechanical properties, and greater design flexibility compared to metallic counterparts.

Traditional fabrication techniques for fiber-reinforced sandwich structures, such as hot press molding [9], vacuum-assisted molding [11], filament winding [139], and tailor-folding [35], often involve complex molds, adhesives, and multi-step curing processes. These methods are labor-intensive, costly, and limit design flexibility. While advanced techniques like vacuum-assisted resin infusion (VARI) and continuous fiber prepregs improve mechanical performance, they remain constrained by mold-based designs, which restrict geometric complexity and increase manufacturing expenses.

Additive manufacturing (AM) presents a promising alternative, offering design freedom, enhanced customization, and the ability to fabricate complex geometries through layer-by-layer material deposition. Key AM techniques include fused filament fabrication (FFF) [74, 140], selective laser sintering (SLS) [141], stereolithography (SLA) [142], and direct ink writing (DIW) [10, 55]. Among these, DIW of thermosetting epoxy composites reinforced with discontinuous fibers offers a highly efficient approach for fabricating advanced sandwich structures. Unlike continuous fiber-reinforced AM methods, which often suffer from fiber misalignment, interfacial weaknesses, and geometric limitations [13, 86], DIW enables the fabrication of self-supporting structures with optimized viscoelastic inks.

DIW relies on specially formulated inks composed of thermoset polymers, discontinuous fillers, and rheological modifiers. These inks exhibit shear thinning and yield stress behavior, ensuring printability and structural integrity. Additionally, incorporating nanofillers such as carbon nanotubes and graphene can enhance composite performance. However, challenges remain, including edge smoothing [143], print imperfections [10], nozzle clogging [144], and limited fiber content [10, 85] for mechanical efficiency.

This study addresses these challenges by utilizing four epoxy-based viscoelastic inks (chapter 2) with varying carbon fiber (10–40 wt.%) and silica (6–2.75 wt.%) concentrations to produce lightweight, high-strength sandwich structures with controlled filler alignment. Bioinspired honeycomb core designs were printed with customized print paths to maximize shape fidelity and minimize material waste. The mechanical performance of the fabricated structures was evaluated through three-point bending tests, with results compared against theoretical models. The DIW-fabricated sandwich structures demonstrated superior or comparable performance to conventional counterparts, underscoring the potential of DIW for scalable, automated manufacturing of advanced composite sandwich structures.

5.2. Experimental Section

5.2.1. DIW Printing of Sandwich Structures

To validate the scalability and practical application of the DIW-printable composite inks, sandwich structures with closed-cell core topologies, consisting of interconnected networks of repeated 2D unit cells, were fabricated as benchmarks. Figure 5.1 (a) – (f) presents optical images of sandwich structures with various core geometries and cured specimens. These images confirm that DIW enables accurate fabrication of diverse core shapes, including straight-edged rectangular cores, angled triangular cores, and hybrid corrugated core designs. Notably, all structures retained their intended shapes without sagging or deviations from the digital models.

These structures exhibit increased porosity and reduced density compared to their base materials, with core cell geometries and corrugation patterns significantly influencing deformation and structural performance. The number of unit cell layers directly impacts core height, affecting moment of inertia (MOI), stability, shear, compression, and bending response [12]. Thus, the printable inks (chapter 2), cell geometry, and core height were considered key design variables.

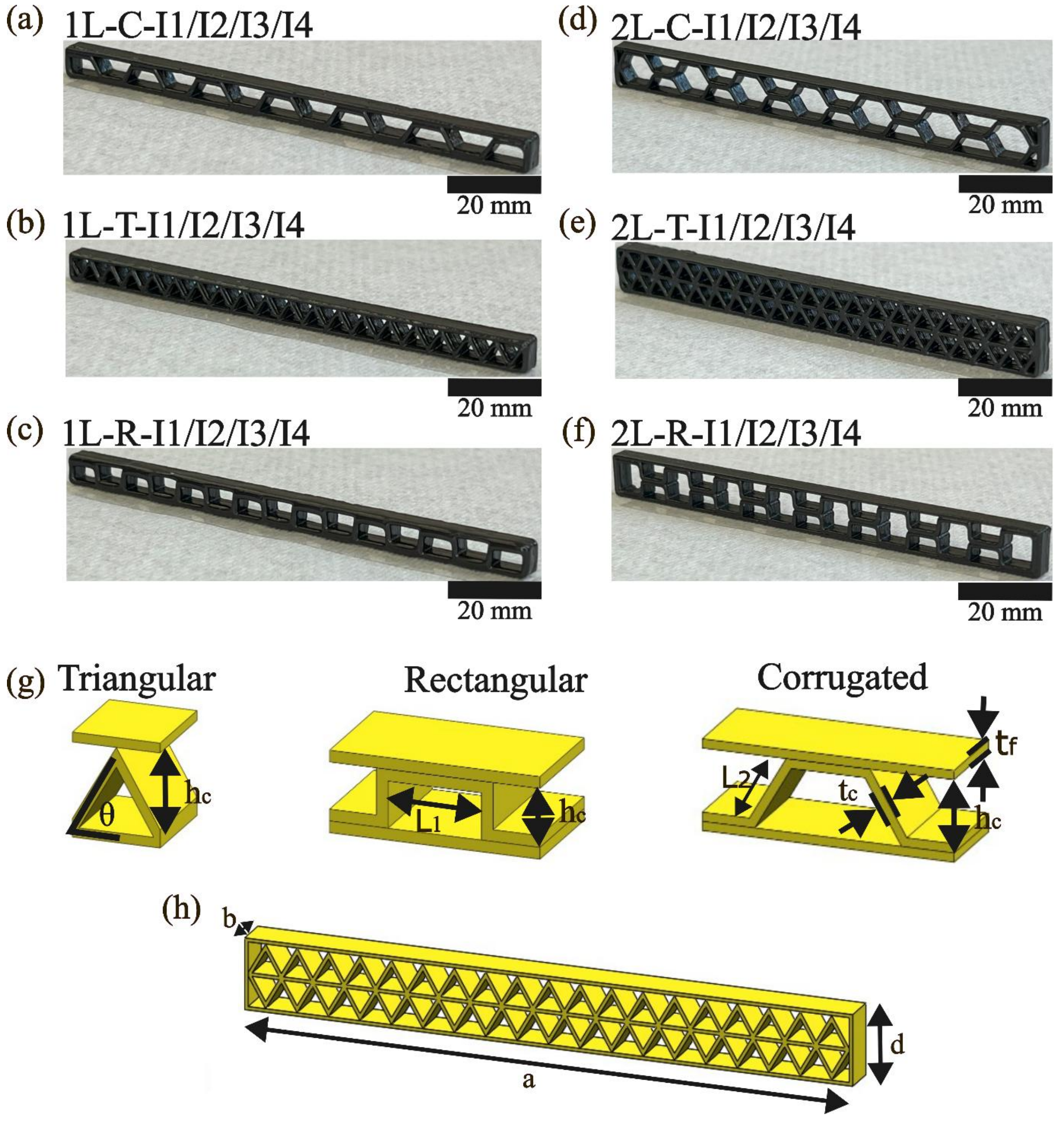

Figure 5. 1. Optical images of DIW-printed CFRECSSs with I1-I4 having various layer and core geometries: (a) IL-C-I1/I2/I3/I4, (b) IL-T-I1/I2/I3/I4, (c) IL-R-I1/I2/I3/I4, (d) 2L-C-I1/I2/I3/I4,

(e) 2L-T-I1/I2/I3/I4, (f) 2L-R-I1/I2/I3/I4, (g) unit cell schematics, (h) 2L beam geometry. (g) - (h) Schematics depict the geometric parameters of the unit cell and CFRECSSs.

The DIW-fabricated sandwich structures featured three core configurations based on repeated unit cells, as shown in figure 5.1 (g). The single-layer (1L) configurations were designed with corrugated (C), triangular (T), and rectangular (R) unit cells, while the two-layer (2L) configurations consisted of two identical unit cells arranged side by side, as illustrated with triangular cores in figure 5.1 (h). Consequently, six sandwich structure designs were fabricated using each ink formulation. These conventional honeycomb configurations were selected for their lightweight and high specific stiffness/strength properties. The use of standard geometric patterns in DIW fabrication facilitates direct comparisons with prior studies in terms of print path design, printability, shape fidelity, surface roughness, and mechanical performance, highlighting the advantages of this approach.

The figure 5.1 (g) illustrates the geometric parameters of the unit cell of different cores, detailing parameters such as L_1 and L_2 for horizontal and inclined/vertical strut lengths respectively, along with t_c for core thickness and θ representing the angle of the inclined strut. Similarly, the dimensions of the sandwich structure block are outlined using length (a), width (b), and height (d), depicted in the figure 5.1 (h). Additionally, parameters such as height of core (h_c) and face sheet thickness (t_f), are also presented in the figure 5.1 (g). The nominal density (ρ_h) of the sandwich structures fabricated in this study was calculated based on the measured mass (m) and volume (V) of each specimen, as indicated by the following equation (5.1). The density of the base material (ρ_s) was measured by the gas pycnometer AccuPyc II 1340. Furthermore, a comprehensive overview of the geometric dimensions for all DIW printed CFRECSSs is provided in the table S5.1 (Supplementary Information 3).

$$\rho_h = \frac{Mass\ of\ the\ sandwich\ structure\ (m)}{Volume\ (a*b*d)} \tag{5.1}$$

The CFRECSSs were classified by unit cell layers (1L, 2L), core geometries (R, T, C), and ink type (I1–I4). For instance, "2L-C-I1" denotes a DIW-printed, two-layer corrugated core using Ink 1. This study defined 24 groups (6 designs × 4 inks), with at least three specimens per group, totaling a minimum of 72 printed samples.

Multi-stroke print paths were employed to fabricate all specimens in this study to seamlessly integrate print and non-print movements, ensuring accurate ink deposition, enhanced print quality, and reduced material waste. Unlike continuous fiber printing, DIW-printed layers maintained precise alignment, avoiding path overlap and unintended ink extrusion during non-print moves—effectively addressing common challenges in continuous fiber composite 3D printing [86, 87]. The printing process was conducted with layer thicknesses of 0.41 mm and 0.58 mm, a printing speed of 10 mm/min, and nozzle diameters of 0.41 mm for Inks 1 and 2, and 0.58 mm for Inks 3 and 4. Each configuration was constructed through ten successive print passes using a bottom-up approach.

5.2.2. Flexural Testing of the Sandwich Structures

Quasi-static three-point flexure tests were conducted to evaluate the mechanical properties of CFRECSSs. Testing was performed under ambient conditions using a single-column Instron 3345 equipped with a 5 kN load cell and a three-point flexure test fixture. A span (L) of 60 mm and a loading rate of 1.0 mm/min were maintained, with load-displacement data recorded via Bluehill software. Each sandwich structure variant was tested three times, totaling a minimum of 72 specimens. Flexural modulus (E), strength (σ), and strain (ε_f) were calculated using equations (5.2), (5.3) and (5.4) following ASTM D790-10 standards. Specific flexural modulus and strength were obtained by normalizing these values with the sandwich structure density (ρ_h). The peak load was defined as the maximum load causing brittle fracture in the outer skin of the CFRECSSs.

$$E = \frac{L^3 m}{4bd^3} \tag{5.2}$$

$$\sigma = \frac{3\ PL}{2\ bd^2} \tag{5.3}$$

$$\varepsilon_f = \frac{6Dd}{L^2} \tag{5.4}$$

In the Equations (5.2), (5.3), and (5.4), E (GPa), σ (MPa), ε_f (mm/mm), D (mm), δ (N/mm), and P (N) denote the modulus of elasticity, flexural stress, flexural strain, maximum central deflection of the beam, slope of the initial straight-line segment of the load-deflection curve (i.e., flexural stiffness in a three-point flexure test), and the applied load at a given point on the load-deflection curve, respectively. Anisotropic material properties of the base material such as stiffness and strength were obtained experimentally from tensile testing. Table 5.1 summarizes tensile test results for DIW specimens with longitudinal (L) and transverse (T) print paths fabricated as per ASTM D638 Type V.

Table 5. 1. Summary of tensile test results.

Specimen name	Tensile Stiffness (GPa)	Tensile Strength (MPa)
I1-L	1.08 ± 0.15	62.75 ± 1.55
I1-T	0.88 ± 0.12	54.02 ± 2.32
I2-L	1.66 ± 0.12	73.57 ± 5.07
I2-T	1.23 ± 0.11	57.47 ± 2.24
I3-L	2.00 ± 0.19	76.92 ± 2.80
I3-T	1.35 ± 0.15	54.85 ± 2.18
I4-L	3.08 ± 0.17	85.94 ± 3.73
I4-T	1.74 ± 0.19	59.58 ± 2.57

5.2.3 Numerical Simulation

To analyze the flexural behavior of the sandwich beam, a finite element analysis (FEA) was performed using the commercial software ANSYS Mechanical. The sandwich configuration was modeled utilizing eight-node solid elements, and after conducting mesh convergence tests, three elements were generated across the width. Furthermore, a mesh convergence test was executed to determine the suitable element size for the simulation model.

For the bending analysis, displacement loading was applied at the midpoint of the loading nose, while the two supports at the base were fixed. Surface-to-surface contact was assumed to be perfectly bonded between interacting surfaces, such as between the facesheets and core, and between the loading nose/supports and facesheets, facilitating load transmission. Anisotropic material properties such as stiffness and strength were obtained experimentally from tensile testing were directly introduced into ANSYS to simulate the mechanical behavior of the sandwich structure.

5.2.4. Imaging

A Keyence VHX-7000 optical microscope was used to assess the surface roughness of the printed sandwich structures. For qualitative fiber alignment analysis, printed specimens were embedded in epoxy resin and polished with a Struers LaboPol 5 semi-automated polishing wheel using progressively finer SiC grit papers ranging between 800-4000, sourced from Buehler and Allied. Final polishing was done manually on an Allied MetPrep 8" wheel with Buehler Microcloth, using glycol-based 3μm and 1μm diamond slurries, followed by a MasterMet 0.02μm SiO_2 colloidal silica solution. After polishing, the samples were sonicated in deionized water with degreaser, ethanol, and methanol, then dried for 24 hours at 60°C to remove moisture before imaging with the Keyence VHX-7000 microscope.

5.3. Results and Discussions

5.3.1. Print Quality and Microstructure Assessment of DIW-Printed Sandwich Structures

Optical microscopy images of honeycomb cores printed using Inks I1–I4 were captured at 20× magnification using a Keyence VHX 7000 microscope to qualitatively assess print quality, as shown in figure 5.2 (a) – (c). The qualitative analysis indicates superior print quality and consistency across the different core structures. Additionally, optical microscopy was employed to evaluate DIW-induced fiber alignment within the printed sandwich structures. Microstructural analysis as shown in figure 5.2 (d)–(f) reveals distinct fiber alignment patterns in corrugated, triangular, and rectangular beam configurations, highlighting the effectiveness of DIW in controlling and engineering microstructure to enhance mechanical performance.

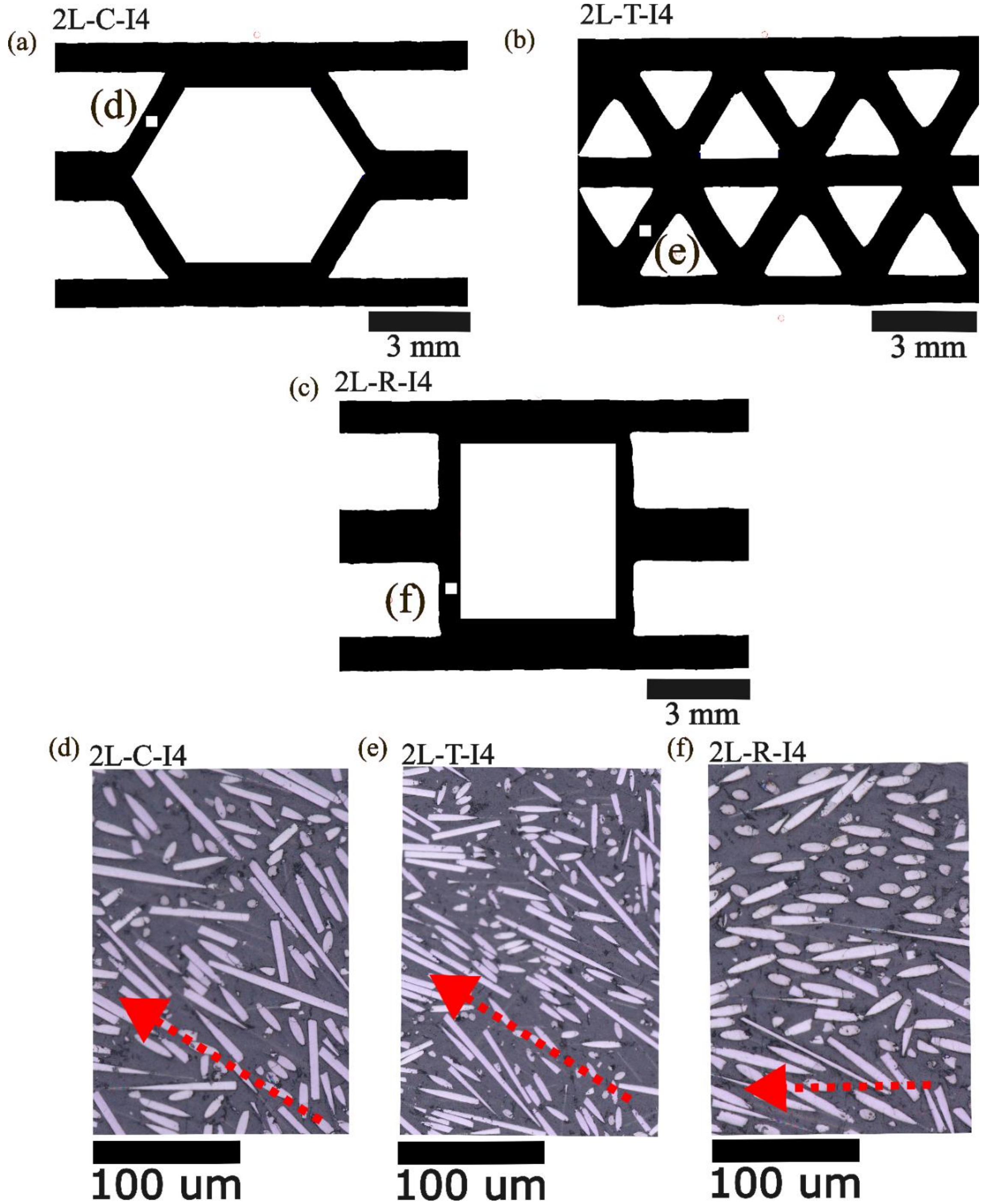
(a)
2L-C-I4
(d)
3 mm
(b)
2L-T-I4
(e)
3 mm
(c)
2L-R-I4
(f)
3 mm
(d) 2L-C-I4
100 um
(e) 2L-T-I4
100 um
(f) 2L-R-I4
100 um

Figure 5. 2. Optical microscopy images of DIW-printed geometries and print-induced fiber alignment in CFRECSS: (a) - (c) honeycomb core profiles, and (d) - (f) DIW print-induced fiber alignment showcasing microstructure tailoring. Red arrow showing the printing direction.

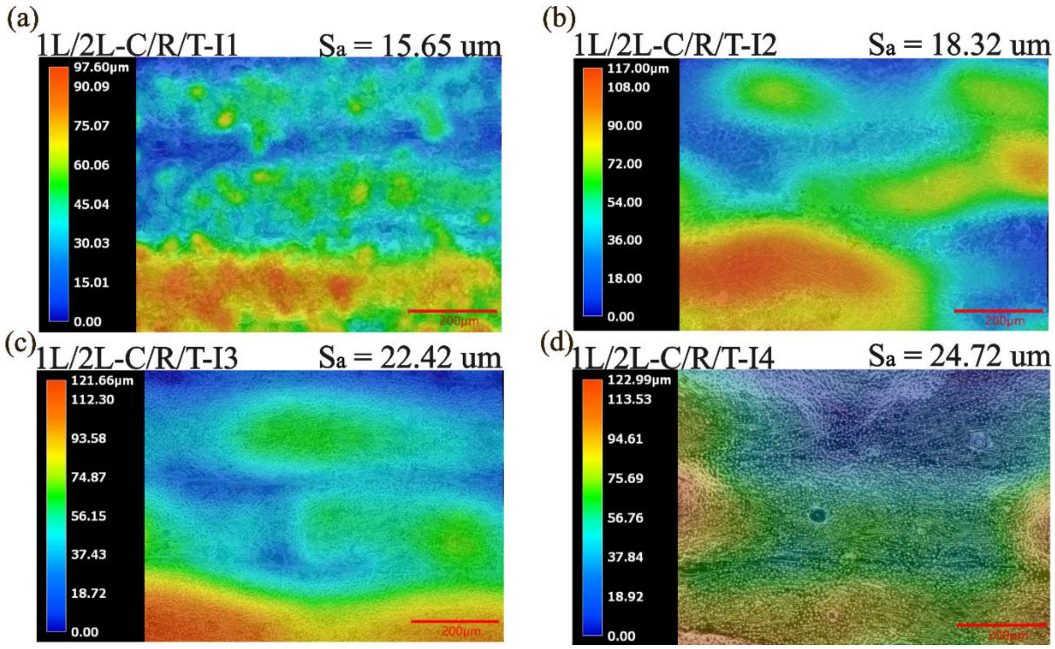

Figure 5. 3. Surface roughness of DIW-printed CFRECSS: (a) - (d) surface height contour maps and S_a values of composite sandwich skins fabricated using I1-I4.

The surface texture of the sandwich structures' skin, printed with different inks, was analyzed post-printing and curing. FFF-printed structures often exhibit poor surface quality, leading to defects that can cause premature failure [93, 94, 145]. Therefore, surface roughness was a key parameter for assessing print quality. Figures 5.3 (a) – (d) present contour diagrams of surface height captured at 200× magnification, illustrating the surface roughness of the skins fabricated using customizable composite inks. The contour patterns appeared consistent across structures printed with Inks 1–4. In this study, S_a (surface area-based roughness) was used instead of R_a (line-based roughness) for a more representative evaluation. The highest peaks and lowest valleys exhibited comparable S_a values across all printed structures, as shown in figures 5.3 (a) – (d). However, the skin of structures printed with Ink 1 had the lowest Sa value, indicating the smoothest surface, attributed to the use of a 410 μm nozzle and higher shear yield modulus, which enhanced print resolution.

The surface contour plots and S_a values were compared with published data for sandwich structures printed with continuous fiber-reinforced thermoplastics and PLA. The S_a values, ranging from 15.65 to 24.72 μm, were comparable to those of CF-reinforced thermoplastics (19 ± 2.6 μm) [13] and lower than PLA (32 ± 5.2 μm) [13] structures. Given the importance of surface roughness in DIW-printed composite sandwich structures, these parameters were analyzed for their impact on fabrication quality and mechanical performance. The findings demonstrated superior surface finish of the DIW-printed CFRECSSs.

5.3.2. Three-Point Flexure Tests Characterization

Three-point flexure tests were conducted on CFRECSSs with single-layer (1L) and double-layer (2L) core configurations (C, R, T) fabricated using inks I1 (10 wt.% carbon fiber) and I4 (40 wt.% carbon fiber) to evaluate their mechanical properties. Figures 5.4 (a) – (d) present the load-displacement and flexural stress-strain responses for each core geometry, ink type (I1 and I4), and layer configuration, showing consistent trends. Figure 5.4 (e) illustrates typical flexural deformation of sandwich beams during testing. Similar responses and deformation patterns were observed for CFRECSSs fabricated with inks I2 and I3, detailed in supplementary figure S5.1 (a) – (f).

As shown in figure 5.4 (a) – (d), all specimens exhibited brittle fracture upon reaching peak load, which was used to compute flexural strength via equation (5.3). No yielding was observed at peak load. High-speed camera images revealed that fracture initiated as a tensile failure at the bottom skin, propagating through the core to the upper skin, leading to a sharp drop in load-bearing capacity (figure 5.4 (f)). Similar fracture patterns were observed in specimens printed with I1–I3 (figure S5.1 (g) – (h)- supplementary information 3). Fracture locations often deviated laterally from the loading point, likely due to the double-wall interface at the load application zone.

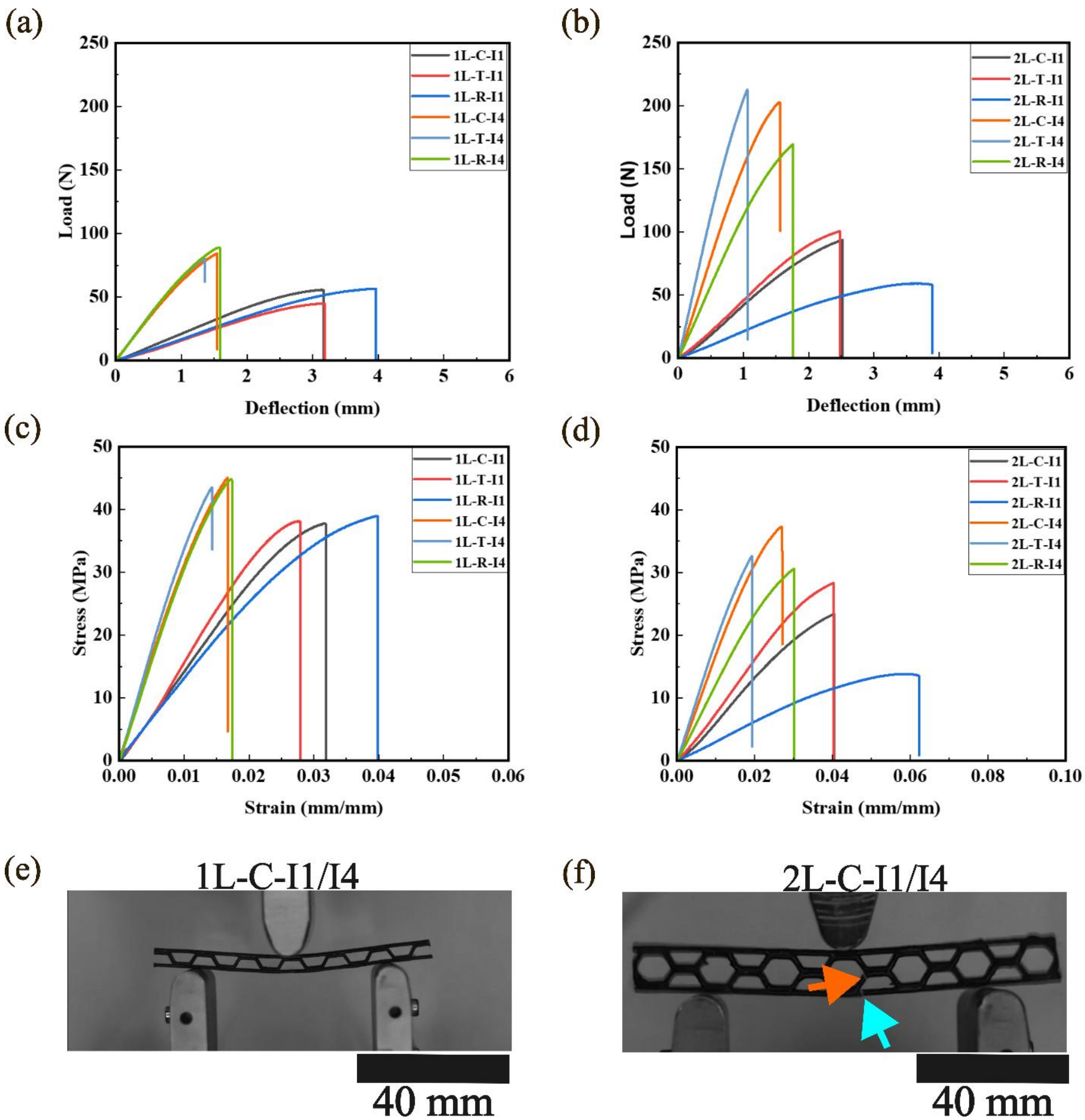

Figure 5. 4. Three-point flexure test results of DIW-printed CFRECSSs. (a) - (b) Load-displacement curves for 1L and 2L beams fabricated with inks I1 and I4. (c) - (d) Stress-strain curves for 1L and 2L beams fabricated using inks I1 and I4. (e) Typical flexural deformation of 1L beams. Similar deformation responses were noted for other 1L and 2Lbeam specimens. (f)

Typical brittle fractures at the skin (cyan) and core (orange) captured during testing of 2L beams. Similar brittle fracture patterns were seen in both 1L and 2L beam specimens. Refer figure S5.1 (a) - (h) in the supplementary information 3 for responses, deformation, and fracture patterns of 1L and 2L beams fabricated using I3 and I4.

As depicted in figure 5.5 (a) – (b), all 2L beams exhibited significantly higher peak load-bearing capacities than their 1L counterparts, attributed to the increased second moment of area. Among all configurations, 2L-T-I1/I2/I3/I4 beams demonstrated the highest load-bearing performance. For instance, the 2L-C-I1, 2L-R-I1, and 2L-T-I1 beams exhibited peak load enhancements of 125%, 84%, and 149%, respectively, compared to 1L beams with the same ink.

Figures 5.5 (c) – (f) show that beams with identical core geometry and layer configurations exhibited increasing flexural stiffness and modulus as fiber content increased from I1 (10 wt.%) to I4 (40 wt.%). For example, 2L-T-I4 beams exhibited 216% and 104% increases in flexural stiffness and modulus, respectively, compared to 2L-T-I1 beams. All 2L beams showed superior flexural stiffness over 1L beams due to their higher moment of inertia; for instance, 2L-C-I4 beams exhibited an 81% increase in flexural stiffness over 1L-C-I4 beams. However, when normalized for flexural modulus, 2L beams showed reduced performance compared to 1L beams, likely due to increased nominal cross-sectional area, which, while enhancing load-bearing capacity, also increased the unsupported span between the skin and core, reducing flexural modulus.

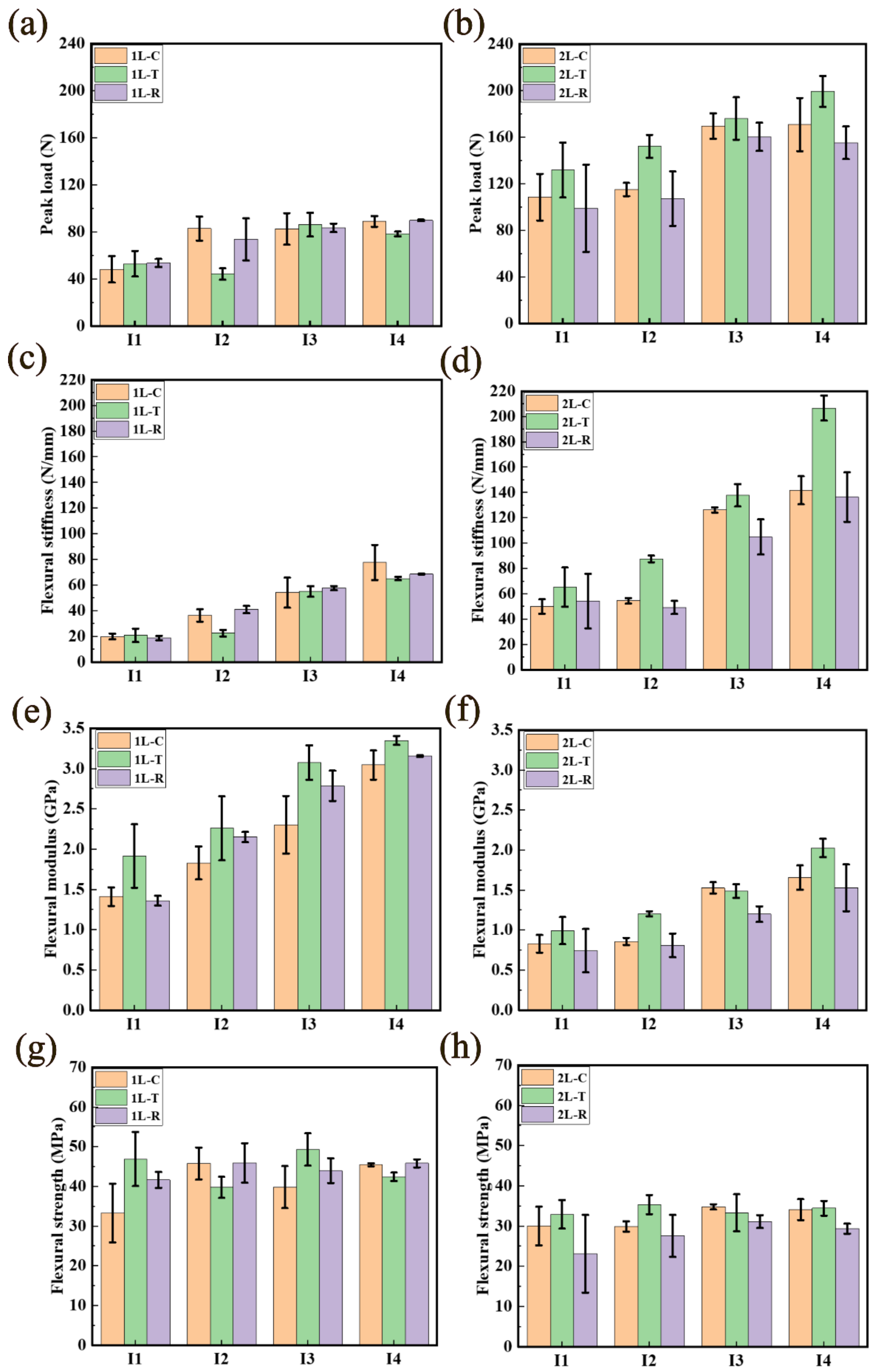

Figure 5. 5. Mechanical properties of 1L and 2L DIW-printed CFRECSSs beams: (a) - (b) peak load, (c) - (d) flexural stiffness, (e) - (f) flexural modulus, and (g) - (h) flexural strength.

Flexural strength was influenced by design (span between skin and core), base material (fiber content), and defects (voids/porosity). As shown in figure 5.5 (g) – (h), sandwich beams fabricated with different inks (I1–I4) exhibited marginal strength variations due to a balance between increased fiber content, which enhances strength, and voids in inks I3 and I4, which degrade performance. A comparison of 1L and 2L beams revealed that 1L beams generally exhibited higher flexural strength, attributed to increased density, reduced cross-sectional area, and smaller unsupported spans, improving bending resistance. For instance, the 1L-C-I4 beam showed a 33% increase in flexural strength over its 2L-C-I4 counterpart. Core geometry also influenced strength due to density variations, voids, cross-sectional area differences, and bending resistance. Further details on specific properties, including specific load, flexural stiffness, modulus, and strength, are provided in figure S5.2 (supplementary information 3).

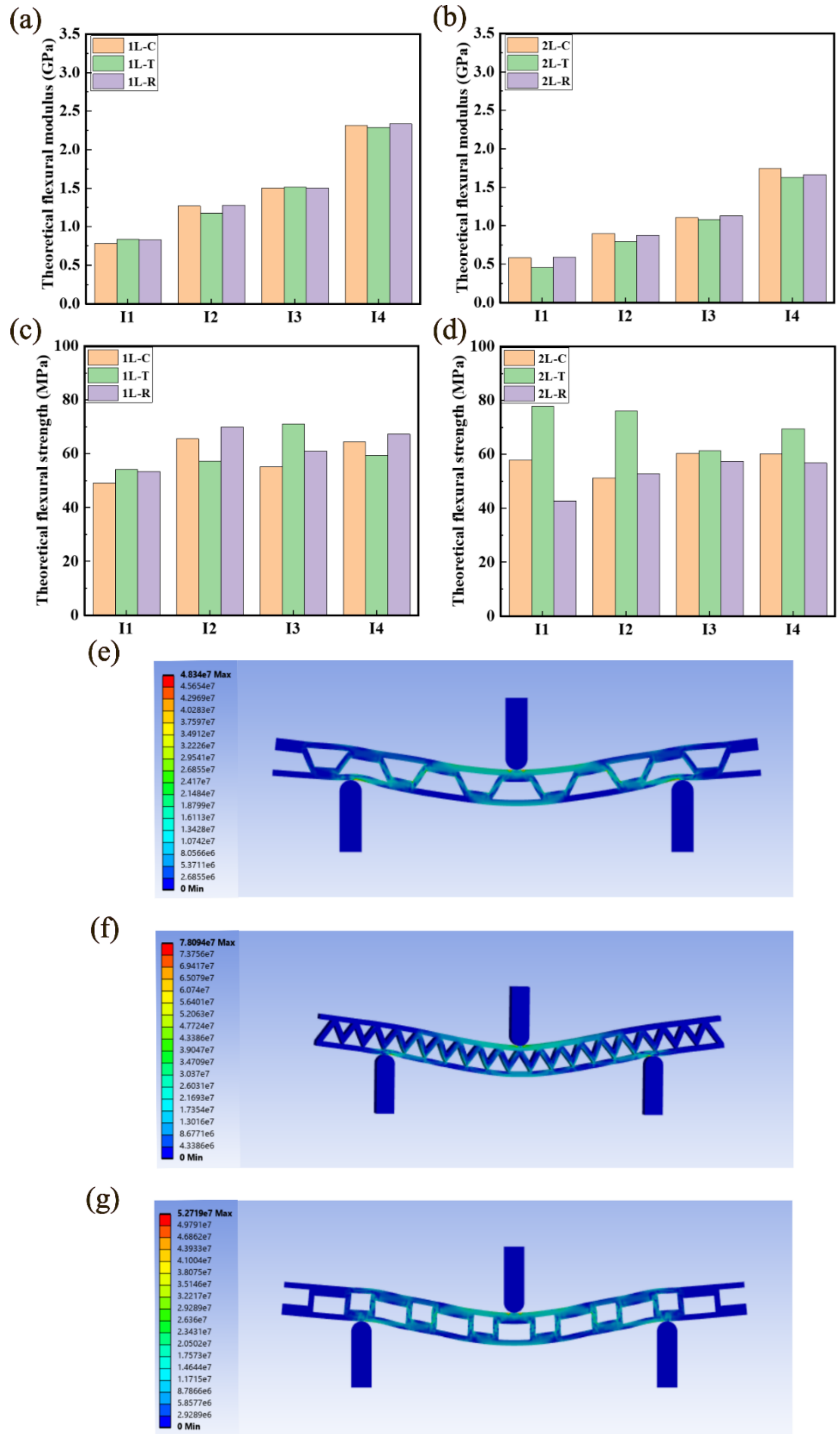

Figure 5. 6. Theoretical and finite element simulation results for DIW-printed CFRECSSs. (a) - (d)Theoretical flexural modulus and strength. (e) – (g) Finite element simulations showing von-

Mises stress distribution and deformation trends of CFRECSSs beams, with stress values presented in pascals (Pa).

The mechanical properties of CFRECSSs obtained from flexure tests were expected to be lower than theoretical predictions due to the use of discontinuous fibers, unlike continuous fiber composites. Thus, the DIW-printed sandwich structures were compared to CFRP sandwich structures. The theoretical flexural modulus (E′) was computed using equation (5.5) [16], assuming a low core modulus relative to the skin and a sufficiently large core-to-skin thickness ratio.

$$E'I = \frac{E_S b t_f^3}{6} + \frac{E_C b h_C^3}{12} + \frac{E_S b t_f (h_c + t_f)^2}{2} \approx \frac{E_S b t_f (h_c + t_f)^2}{2} \qquad (5.5)$$

In the equations provided, E' represents the flexural modulus, I denote the second moment of area, E_S and E_C are the moduli of the skin and core, respectively. Additionally, t_f and h_c represent the thicknesses of the skin and core, while "b" denotes the beam width. The values of E_S were determined from tensile tests as described in section 5.2.2. Based on the equation, the calculated theoretical flexural modulus (E') of 1L and 2L CFRECSSs beams is presented in the figure 5.6 (a) and (b). Upon analysis, E' is consistently lower than the experimentally determined flexural modulus of the CFRECSSs (figure 5.5 (e) – (f)), likely due to the contribution of the core's flexural modulus, suggesting mechanically comparable to the existing CFRP sandwich structures. For the theoretical flexural strength (σ′) calculated using the equation (5.6) [17], the maximum load corresponds to the value at which skin fracture was observed during testing.

$$\sigma' = \frac{M}{b h_c t_f} \qquad (5.6)$$

In the above Equation, M is the bending moment, and σ′ is the theoretical flexural strength. The theoretical strength values (figure 5.6 (c) – (d)) were 1.15 to 2.36 times higher than experimental results, indicating reasonable agreement. Experimental strength reductions were attributed to voids in the base material and defects in bonding between the skin and core, reducing structural integrity. Additionally, finite element analysis, as illustrated in figure 5.6 (e) – (g), reveals similar stress distributions, and deformation trends to those observed experimentally. Overall, DIW 3D printing of CFRECSSs offers potential for novel core geometries with improved mechanical properties, alongside benefits such as batch production and process automation.

5.3.3. Comparison of Competing Sandwich Structures

The material property charts in figure 5.7 (a) – (b) provide a comparative analysis of the mechanical performance of 3D-printed CFRECSSs against various sandwich structures fabricated using different methods and materials. These include 3D-printed continuous fiber-reinforced composite trapezoidal corrugated sandwich structures (CFRCTCSs) [46], all-metallic hybrid-cored sandwiches [146], 3D CFRP honeycomb beams [27], CFRP skin/aluminum core panels [147], GFRP/wooden panels [148], 3D-printed meta-sandwiches [149], GFRP truss cores [150], woven textile panels [151], 3D-printed lattice core beams [152], and GFRP skin/foam core structures [153].

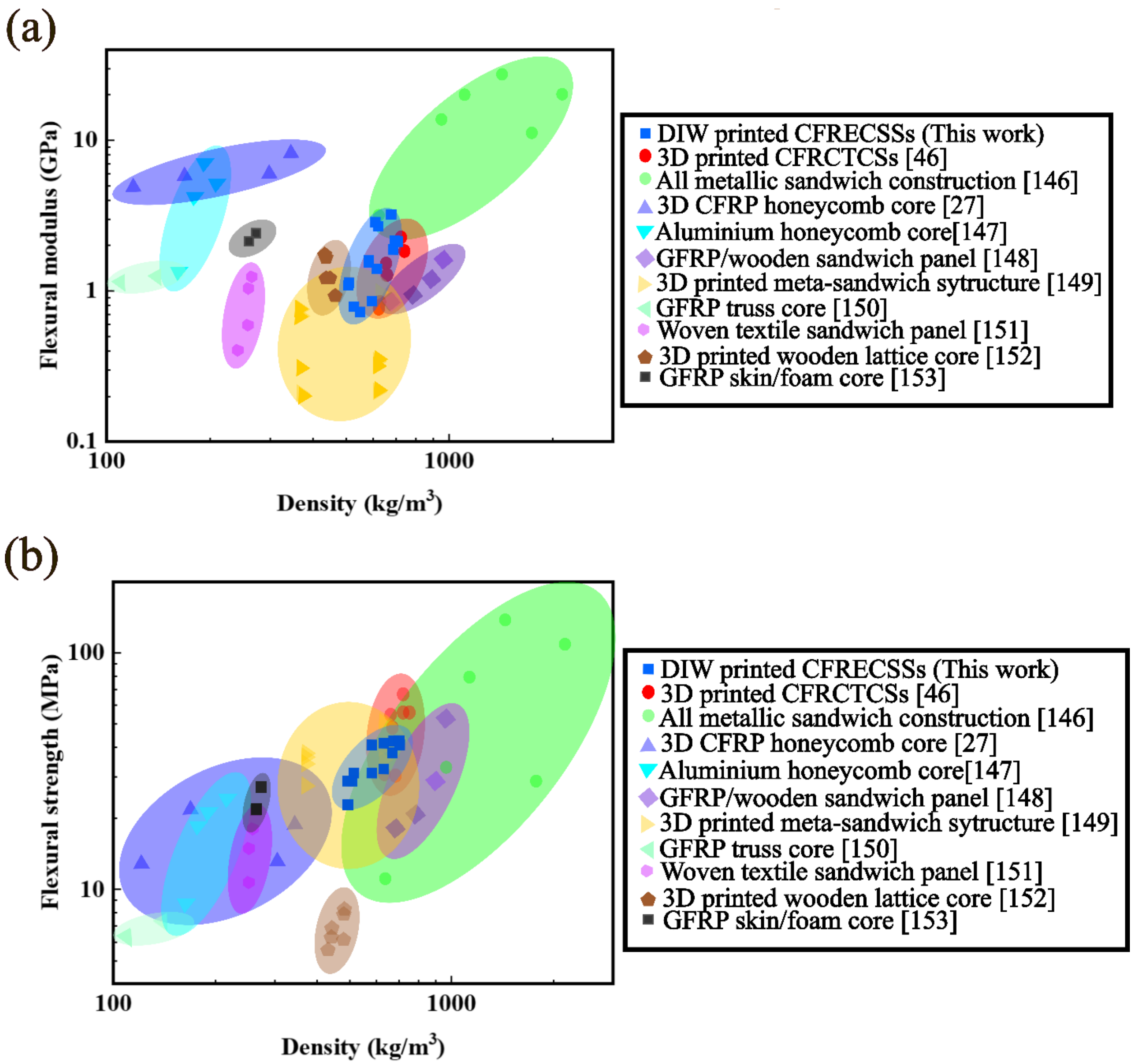

Figure 5. 7. Comparison of three-point flexure (a) modulus and (b) strength between DIW-printed CFRECSSs and other sandwich structures.

Figure 5.7 (a) compares the experimentally measured flexural modulus, showing that CFRECSSs exhibit significantly higher values than 3D-printed CFRCTCSs, polymer meta-sandwich panels, GFRP/wooden panels, woven textile panels, 3D-printed wooden lattice cores, GFRP truss cores, and GFRP skin/foam cores, while being comparable to 3D CFRP and aluminum honeycomb cores.

Figure 5.7 (b) presents the flexural strength comparison, indicating that CFRECSSs outperform woven textile panels, GFRP truss cores, 3D CFRP honeycomb cores, aluminum honeycomb cores, GFRP skin/foam cores, and 3D-printed wooden lattice cores. Additionally, CFRECSSs demonstrate comparable flexural strength to conventional 3D-printed structures such as polymer meta-sandwiches, CFRCTCSs, and GFRP/wooden panels. These results highlight the advantages of DIW with multi-material viscoelastic composite inks in fabricating high-performance sandwich structures. While all-metallic hybrid-cored structures exhibit higher flexural modulus and strength, the lightweight nature of CFRECSSs makes them attractive for various applications.

5.4. Chapter Conclusion

This study successfully fabricated lightweight, high-strength carbon fiber-reinforced epoxy composite sandwich structures (CFRECSSs) using the DIW printing process and viscoelastic inks with tailored fiber content, enabling precise layer-by-layer deposition of complex core geometries—including corrugated, rectangular, and triangular shapes—along with integrated top and bottom skins, eliminating the need for adhesives or custom molds. Using a pneumatic printer and inks with varying mechanical properties (I1–I4) and core layers (1L–2L) resulted in prototypes with exceptional surface quality, surpassing PLA and comparable to 3D-printed continuous carbon fiber composites.

Three-point flexure tests on printed structures with different core shapes, inks, and layer configurations led to the following conclusions:

- Increasing the core layer count from 1L to 2L enhances peak load-bearing capacity, flexural stiffness, and specific flexural stiffness.

- A transition from 1L to 2L reduces both flexural modulus and strength, including their specific counterparts.
- Increasing base material properties (I1–I4) improves flexural stiffness, modulus, and their specific values.
- Comparisons between experimental and analytical predictions show higher modulus values and a reasonable correlation in flexural strength.
- CFRECSSs exhibit competitive flexural properties compared to other advanced sandwich structures.

This research highlights the potential of DIW printing combined with engineered inks to fabricate advanced composite sandwich structures with tailored mechanical properties, paving the way for lightweight, high-performance applications.

Chapter 6: Conclusion and Future Work

6.1. Conclusion

This study successfully developed and implemented a direct ink writing (DIW) 3D printing approach for fabricating lightweight, high-strength short carbon fiber-reinforced epoxy composite honeycomb cores and sandwich structures. By formulating viscoelastic inks with tailored rheological properties and fiber content (10–40 wt.%), precise, mold-free fabrication of bioinspired cellular architectures was achieved with superior print quality, shape fidelity, and consistent fiber-matrix bonding. These DIW-printed structures exhibited enhanced mechanical performance compared to conventional 3D-printed thermoplastics, continuous carbon fiber composites, and metal-based cellular architectures.

In-plane compression testing demonstrated that compressive stiffness and strength improved with increased infill density (30–50%), reduced cell size, customized core geometry, and enhanced base material properties. Hexagonal cores exhibited superior mechanical and specific mechanical properties compared to triangular and square cores. While all geometries aligned with scaling laws for stiffness, hexagonal cores exceeded strength predictions, validating the effectiveness of DIW printing in fabricating high-performance composite honeycombs.

Out-of-plane compression and crashworthiness testing revealed that increasing infill density improved load-bearing capacity, with square cores exhibiting the highest energy absorption (EA). Specific energy absorption (SEA) and crushing force efficiency (CFE) metrics demonstrated that DIW-printed composite cores perform comparably to, or better than, conventional continuous fiber, metal, and polymer-based structures. Despite minor void formation in higher fiber-content inks, DIW-enabled control over material deposition and geometry resulted in robust, crashworthy structures suitable for lightweight impact-resistant applications in aerospace, automotive, and structural engineering.

Three-point bending tests on DIW-printed sandwich structures showed that increasing core layers (1L to 2L) significantly enhanced flexural stiffness and peak load-bearing capacity, although flexural strength decreased. Core geometry variations influenced mechanical properties, with engineered ink formulations further improving flexural modulus and specific flexural stiffness. Experimental results aligned well with analytical predictions, demonstrating the viability of DIW-printed carbon fiber-reinforced epoxy composite sandwich structures as high-performance alternatives to conventional continuous fiber-reinforced thermoplastic composites.

Overall, this research highlights the potential of DIW and engineered viscoelastic inks for producing advanced composite cellular and sandwich structures with tunable mechanical properties. The ability to tailor geometry, material composition, and infill density offers a pathway for designing next-generation lightweight, high-performance structural materials for aerospace, automotive, maritime, and energy absorption applications.

6.2. Recommendations for Future Work

Future research should focus on enhancing the mechanical performance, scalability, and multifunctionality of DIW-printed composite honeycomb and sandwich structures. While this study demonstrated the potential of engineered viscoelastic inks and DIW printing for fabricating lightweight, high-strength cellular architectures, several areas require further exploration. Key recommendations for future work include:

- Advancing Ink Formulations

- Investigate varying fiber-matrix compositions to improve mechanical properties.
    - Explore the inclusion of nano-fillers (e.g., graphene, CNTs) to enhance strength, toughness, and electrical conductivity.
- Enhancing Printing Techniques
    - Implement multi-material DIW printing to create gradient or functionally graded structures for tailored performance.
    - Refine printing parameters (e.g., extrusion rate, layer height, curing conditions) to minimize voids and defects.
- Expanding Mechanical Testing
    - Conduct high-strain-rate impact and dynamic loading tests to evaluate crashworthiness in real-world conditions.
    - Perform fatigue and creep testing to assess long-term structural reliability.
- Exploring Structural and Design Improvements
    - Develop hybrid core designs combining multiple geometric configurations for improved strength-to-weight ratios.
    - Create reconfigurable or adaptive cellular structures for tunable stiffness and energy absorption.
    - Integrate bioinspired hierarchical architectures to enhance load distribution and failure resistance.
- Strengthening Numerical and Analytical Modeling

  - Develop predictive models using FEA and homogenization techniques to refine core design and material selection.
  - Validate computational models with experimental results to improve accuracy in performance prediction.
- Investigating Functional Applications and Scalability
  - Assess large-scale manufacturing feasibility for aerospace and automotive applications.
  - Study thermal and acoustic insulation properties for multifunctional structural applications.
  - Explore sustainability aspects by incorporating recyclable or bio-based resin systems.

By addressing these areas, DIW-printed composite structures can be further developed for high-performance applications in aerospace, automotive, and other engineering industries.

Supplementary Information 1

Table S3.1. Geometric parameters of DIW printed honeycomb core configurations.

Specimens	W mm	T mm	H mm	h mm	L mm	θ deg	t_1 Mm	t_2 mm	s mm	m g	ρ_h g/cc	ρ_s g/cc	ρ_r
I1-H-I30	21.7	3.8	21.3	3.5	2.2	60	0.92	1.84	3.59	0.92	0.53	1.10	0.48
I1-H-I40	20.4	4.0	23.8	2.8	1.4	60	1.18	1.91	2.19	1.37	0.71	1.10	0.65
I1-H-I50	19.0	3.7	24.8	2.3	0.9	60	1.05	1.78	1.43	1.38	0.78	1.10	0.71
I2-H-I30	21.1	3.4	21.6	3.5	2.2	60	1.03	1.88	3.40	0.97	0.62	1.05	0.59
I2-H-I40	20.3	3.6	23.8	2.8	1.4	60	1.03	1.78	2.20	1.21	0.70	1.05	0.67
I2-H-I50	19.1	3.6	25.1	2.3	0.9	60	1.00	1.75	1.49	1.37	0.79	1.05	0.75
I3-H-I30	21.9	3.4	21.8	3.5	2.2	60	1.13	2.08	3.39	1.00	0.61	0.89	0.69
I3-H-I40	20.1	3.6	24.0	2.8	1.4	60	1.13	2.00	2.12	1.16	0.66	0.89	0.74
I3-H-I50	19.4	3.6	25.3	2.3	0.9	60	1.11	1.83	1.46	1.30	0.74	0.89	0.83
I4-H-I30	21.2	4.6	22.2	3.5	2.2	60	1.39	2.51	2.99	1.32	0.62	0.92	0.67
I4-H-I40	19.9	4.4	24.1	2.8	1.4	60	1.28	2.23	1.89	1.44	0.69	0.92	0.75
I4-H-I50	19.3	4.3	25.3	2.3	0.9	60	1.12	1.86	1.38	1.47	0.71	0.92	0.77
I1-T-I30	21.4	3.6	20.2	---	10.2	60	0.87	---	7.72	0.48	0.31	1.10	0.28
I1-T-I40	18.7	3.6	21.4	---	6.9	60	0.77	---	4.98	0.56	0.39	1.10	0.35
I1-T-I50	18.1	3.6	23.3	---	5.5	60	0.75	---	3.83	0.66	0.44	1.10	0.40
I2-T-I30	20.9	3.1	20.5	---	10.2	60	1.20	---	7.53	0.46	0.34	1.05	0.33
I2-T-I40	18.2	3.3	21.9	---	6.9	60	1.05	---	4.88	0.59	0.45	1.05	0.42
I2-T-I50	17.9	3.4	23.4	---	5.5	60	0.82	---	3.92	0.61	0.43	1.05	0.41
I3-T-I30	20.8	3.4	20.6	---	10.2	60	1.13	---	7.45	0.46	0.31	0.89	0.35
I3-T-I40	18.3	3.4	21.8	---	6.9	60	1.11	---	4.78	0.58	0.42	0.89	0.47
I3-T-I50	17.5	3.5	23.8	---	5.5	60	1.06	---	3.66	0.74	0.50	0.89	0.57
I4-T-I30	20.8	4.0	21.1	---	10.2	60	1.31	---	6.95	0.64	0.37	0.92	0.40
I4-T-I40	17.9	4.1	22.3	---	6.9	60	1.33	---	4.29	0.80	0.49	0.92	0.53
I4-T-I50	17.4	4.0	24.1	---	5.5	60	1.16	---	3.37	0.88	0.52	0.92	0.57
I1-S-I30	21.3	3.6	24.4	5.3	5.3	90	1.09	1.97	4.97	0.95	0.50	1.10	0.45
I1-S-I40	22.6	3.8	27.0	4.0	4.0	90	1.23	1.93	3.67	1.35	0.58	1.10	0.53
I1-S-I50	19.2	3.6	21.9	3.2	3.2	90	1.16	1.83	2.94	0.97	0.64	1.10	0.58

I2-S-I30	21.2	3.5	24.4	5.3	5.3	90	1.18	1.98	4.96	0.91	0.51	1.05	0.48
I2-S-I40	22.8	3.4	26.9	4.0	4.0	90	1.00	1.78	3.82	1.12	0.55	1.05	0.52
I2-S-I50	19.5	3.4	22.2	3.2	3.2	90	1.13	1.86	2.94	0.97	0.65	1.05	0.62
I3-S-I30	21.2	3.4	24.3	5.3	5.3	90	1.05	1.85	5.15	0.75	0.43	0.89	0.49
I3-S-I40	22.6	3.6	27.0	4.0	4.0	90	1.14	1.90	3.74	1.13	0.51	0.89	0.57
I3-S-I50	19.3	3.6	22.1	3.2	3.2	90	1.05	1.76	3.11	0.84	0.55	0.89	0.62
I4-S-I30	20.6	4.3	24.9	5.3	5.3	90	1.63	2.59	4.41	1.10	0.50	0.92	0.54
I4-S-I40	22.2	4.4	27.7	4.0	4.0	90	1.85	2.65	3.01	1.66	0.62	0.92	0.67
I4-S-I50	18.8	4.5	22.8	3.2	3.2	90	1.60	2.51	2.50	1.33	0.69	0.92	0.75

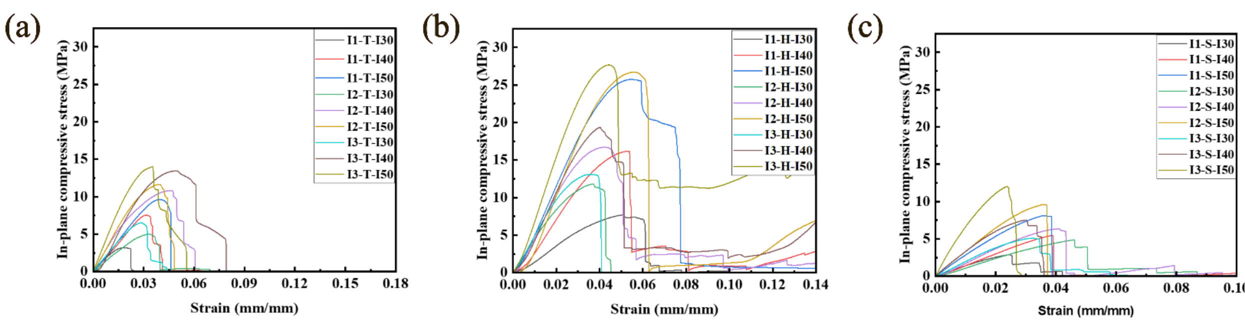

Figure S3.1 In-plane compressive stress-strain curves for (a) triangular, (b) hexagonal, and (c) square honeycomb cores fabricated with I1–I3.

Supplementary Information 2

Table S4.1. Geometric parameters of DIW printed fiber-reinforced epoxy composite honeycomb cores.

Specimens	L mm	W mm	H mm	h mm	L Mm	θ deg	t_1 mm	t_2 mm	s mm	m g	ρ_h g/cc	ρ_s g/cc	ρ_r --
I1-H-I30	21.7	17.4	3.9	3.5	2.2	60.0	0.9	1.7	3.7	0.7	0.4	1.1	0.4
I1-H-I40	20.3	19.6	3.9	2.8	1.4	60.0	0.9	1.7	2.5	0.9	0.6	1.1	0.5
I2-H-I30	21.7	17.3	4.1	3.5	2.2	60.0	1.1	2.0	3.5	0.8	0.5	1.1	0.5
I2-H-I40	20.4	20.0	3.8	2.8	1.4	60.0	1.2	2.1	2.4	1.0	0.6	1.1	0.6
I3-H-I30	21.2	16.7	4.8	3.5	2.2	60.0	1.3	2.2	3.2	0.8	0.5	0.9	0.5
I3-H-I40	20.1	19.6	4.1	2.8	1.4	60.0	1.2	2.1	2.0	1.0	0.6	0.9	0.7
I4-H-I30	20.8	16.4	4.5	3.5	2.2	60.0	1.3	2.3	3.2	0.8	0.5	0.9	0.6
I4-H-I40	19.5	18.3	4.1	2.8	1.4	60.0	1.4	2.2	1.9	0.9	0.6	0.9	0.7
I1-S-I30	22.4	21.5	3.9	5.3	5.3	90.0	1.8	0.9	5.4	0.7	0.4	1.1	0.4
I1-S-I40	25.1	22.8	4.1	4.0	4.0	90.0	2.1	1.2	3.7	1.3	0.6	1.1	0.5
I2-S-I30	20.5	21.9	3.7	5.3	5.3	90.0	1.1	1.1	7.4	0.6	0.3	1.1	0.3
I2-S-I40	21.7	19.0	3.6	4.0	4.0	90.0	1.0	1.0	4.7	0.6	0.4	1.1	0.4
I3-S-I30	21.2	20.7	4.5	5.3	5.3	90.0	2.1	1.4	4.7	0.9	0.4	0.9	0.5
I3-S-I40	24.1	22.5	4.7	4.0	4.0	90.0	2.4	1.6	3.3	1.4	0.5	0.9	0.6
I4-S-I30	21.0	21.1	4.0	5.3	5.3	90.0	1.5	1.5	7.4	0.7	0.4	0.9	0.4
I4-S-I40	22.0	17.7	4.1	4.0	4.0	90.0	1.3	1.2	4.8	0.8	0.5	0.9	0.5
I1-T-I30	20.0	21.2	3.7	--	10.2	60.0	0.8	--	8.0	0.4	0.3	1.1	0.3
I1-T-I40	21.2	19.1	3.3	--	6.9	60.0	0.8	--	5.2	0.5	0.3	1.1	0.3
I2-T-I30	20.5	21.9	3.7	--	10.2	60.0	1.1	--	7.4	0.6	0.3	1.1	0.3
I2-T-I40	21.7	19.0	3.6	--	6.9	60.0	1.0	--	4.7	0.6	0.4	1.1	0.4
I3-T-I30	20.0	20.9	4.1	--	10.2	60.0	1.1	--	8.1	0.5	0.3	0.9	0.3
I3-T-I40	22.0	18.4	4.3	--	6.9	60.0	1.3	--	4.8	0.8	0.5	0.9	0.5
I4-T-I30	21.0	21.1	4.0	--	10.2	60.0	1.5	--	7.4	0.7	0.4	0.9	0.4
I4-T-I40	22.0	17.7	4.1	--	6.9	60.0	1.3	--	4.8	0.8	0.5	0.9	0.5

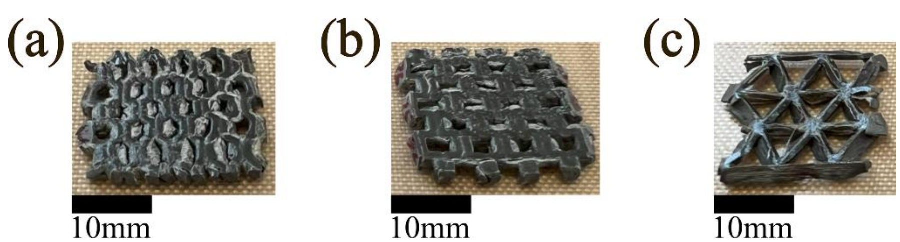

Figure S4.1. Honeycomb core composite specimens post out-of-plane compression testing: (a) hexagonal, (b) square, (c) triangular.

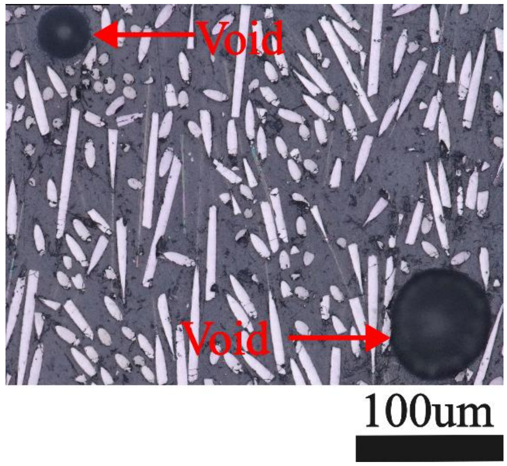

Figure S4.2. Microstructure showing voids in honeycomb core composite cell wall fabricated using I4.

Supplementary Information 3

Table S5.1. Geometric parameters of DIW-printed CFRECSSs with various core geometries and layers.

Specimens	a mm	b mm	d mm	L_1 mm	L_2 mm	θ deg	t_f mm	t_C mm	h_c mm	m g	ρ_h g/cc	ρ_s g/cc	ρ_r
IL-C-I1	90.22	3.78	5.84	5.08	1.85	60.00	1.03	1.06	3.78	1.15	0.58	1.10	0.53
IL-T-I1	90.09	3.80	5.65	−	4.26	60.00	1.14	1.13	3.38	1.41	0.72	1.10	0.66
I1-R-I1	92.44	3.51	5.98	6.50	3.20	90.00	1.18	1.20	3.62	1.20	0.62	1.10	0.56
2L-C-I1	95.05	3.30	9.87	5.08	1.85	60.00	1.12	1.14	7.63	1.49	0.48	1.10	0.44
2L-T-I1	90.10	3.74	9.89	−	4.26	60.00	0.82	0.87	8.24	2.05	0.61	1.10	0.56
2L-R-I1	94.01	3.96	9.93	6.50	3.20	90.00	1.15	1.16	7.64	1.93	0.52	1.10	0.48
IL-C-I2	90.72	4.04	6.27	5.08	1.85	60.00	1.23	1.26	3.81	1.46	0.63	1.05	0.60
IL-T-I2	90.05	3.33	5.57	−	4.26	60.00	0.95	0.90	3.68	1.06	0.64	1.05	0.60
IL-R-I2	92.72	3.34	6.28	6.50	3.20	90.00	1.25	1.22	3.77	1.30	0.66	1.05	0.63
2L-C-I2	95.22	3.78	10.04	5.08	1.85	60.00	1.15	1.17	7.73	1.86	0.51	1.05	0.49
2L-T-I2	90.49	3.63	10.25	−	4.26	60.00	1.00	1.02	8.24	2.26	0.67	1.05	0.64
2L-R-I2	94.13	3.54	9.98	6.50	3.20	90.00	1.11	1.13	7.77	1.78	0.53	1.05	0.51
IL-C-I3	90.91	4.20	6.74	5.08	1.85	60.00	1.29	1.25	4.17	1.54	0.60	0.89	0.67
IL-T-I3	90.35	4.10	6.12	−	4.26	60.00	1.18	1.23	3.76	1.65	0.73	0.89	0.81
I1-R-I3	93.17	4.02	6.58	6.50	3.20	90.00	1.26	1.29	4.07	1.56	0.63	0.89	0.71
2L-C-I3	95.65	4.21	10.53	5.08	1.85	60.00	1.24	1.26	8.04	2.36	0.55	0.89	0.62
2L-T-I3	90.87	4.42	10.49	−	4.26	60.00	1.21	1.28	8.07	2.83	0.67	0.89	0.76
2L-R-I3	94.46	4.39	10.17	6.50	3.20	90.00	1.24	1.26	7.69	2.27	0.54	0.89	0.60
IL-C-I4	90.76	4.21	6.45	5.08	1.85	60.00	1.23	1.26	3.98	1.47	0.60	0.92	0.65
IL-T-I4	90.10	4.20	6.34	−	4.26	60.00	1.19	1.21	3.97	1.65	0.69	0.92	0.75
I1-R-I4	92.85	4.07	6.44	6.50	3.20	90.00	1.25	1.26	3.95	1.48	0.61	0.92	0.66
2L-C-I4	95.25	4.35	10.29	5.08	1.85	60.00	1.26	1.23	7.77	2.10	0.49	0.92	0.54
2L-T-I4	90.74	4.57	10.43	−	4.26	60.00	1.16	1.22	8.11	3.02	0.70	0.92	0.76
2L-R-I4	94.25	4.57	10.08	6.50	3.20	90.00	1.15	1.18	7.77	2.14	0.49	0.92	0.54

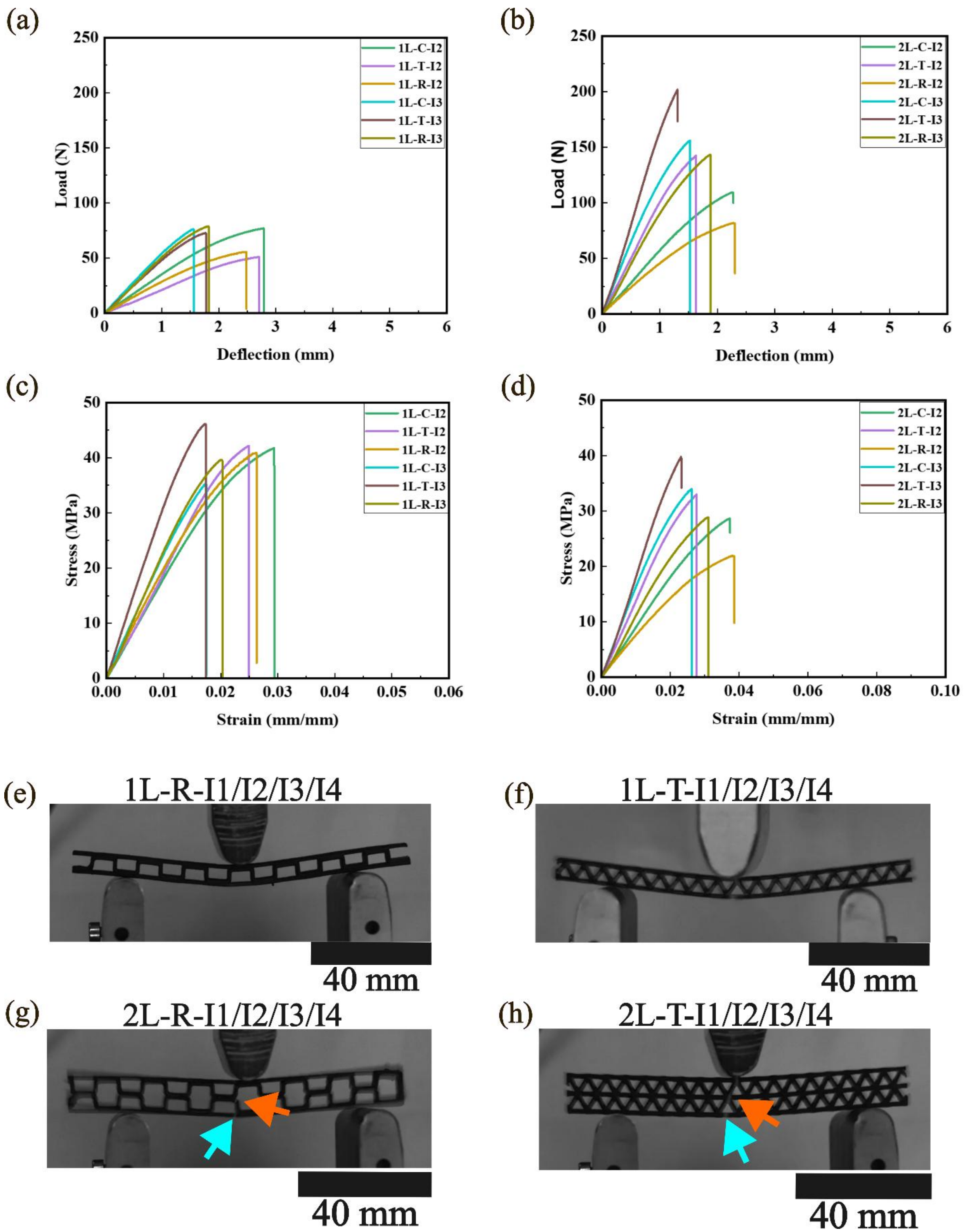

Figure S5.1. Three-point flexure test of DIW-printed CFRECSSs: (a) - (b) Load-displacement for 1L and 2L beams with I2 and I3. (c) - (d) Stress-strain for 1L and 2L beams with I2 and I3. (e) -

(f) Flexural deformation of 1L beams (rectangular and triangular core). (g) - (h) Brittle fractures in 2L beams (skin: cyan, core: orange).

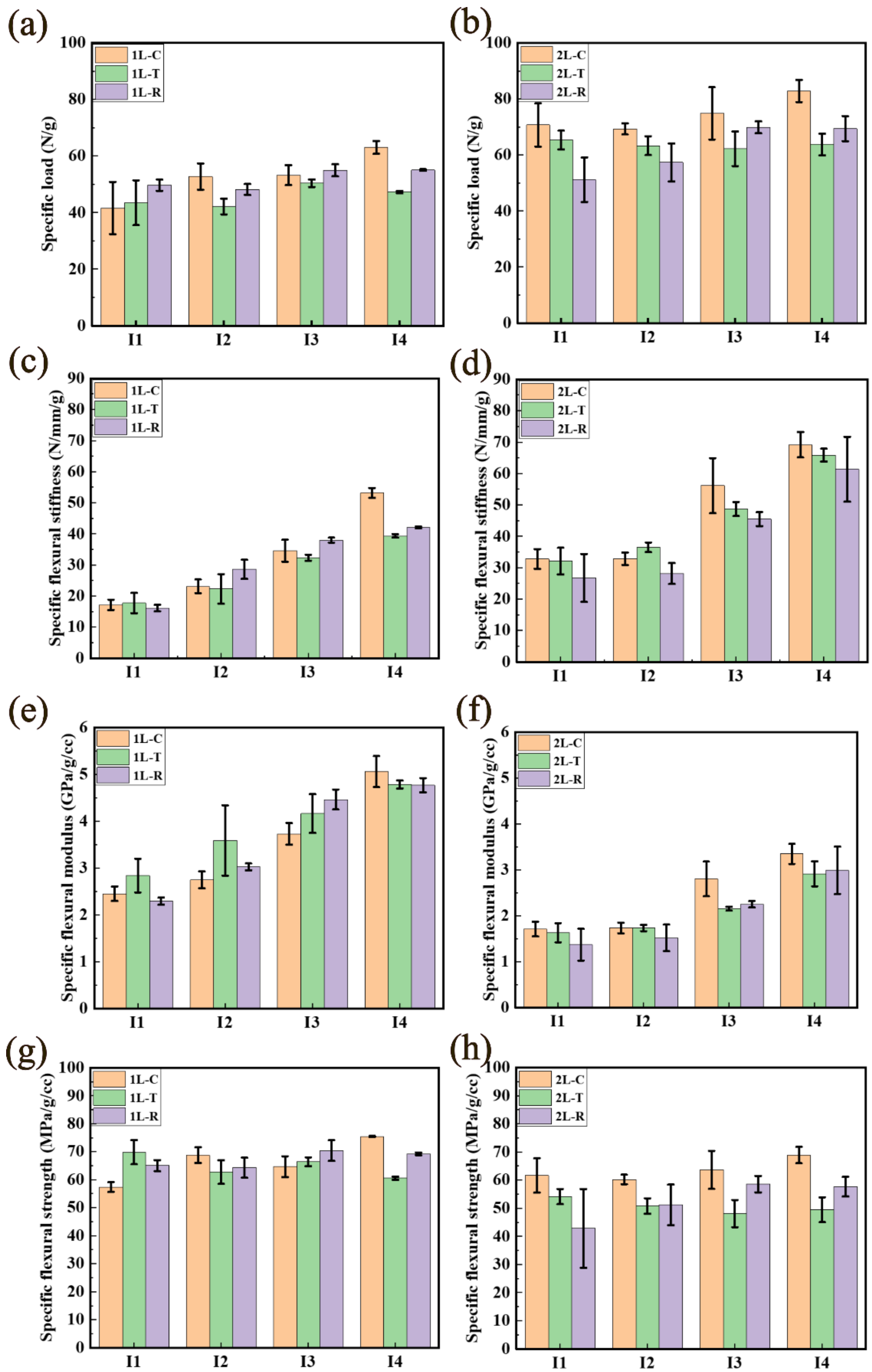

Figure S5.2. Specific mechanical properties of 1L and 2L DIW-printed CFRECSSs beams: (a)-(b) specific load, (c)-(d) specific flexural stiffness, (e)-(f) specific flexural modulus, and (g)-(h) specific flexural strength.

All 2L beams demonstrated superior specific load-carrying capacity compared to the 1L variants due to enhanced sectional properties, as depicted in figure S5.2 (a) – (b). Additionally, both 1L and 2L beams with corrugated cores, fabricated using inks I1-I4, showed improved specific load capacity trend compared to triangular and rectangular cores, likely due to their reduced mass. Conversely, as observed in figure S5.2 (a) – (b), 1L and 2L beams with triangular cores exhibited either lower specific load capacities than those with corrugated cores (1L-C, and 2L-C), potentially due to their higher mass, as detailed in table S1.

As shown in figure S5.2 (c) – (f), sandwich beams with the same core geometry and layers (1L, 2L) but different inks (I1–I4) exhibited progressive increases in specific flexural stiffness and modulus. For example, 2L-T-I4 beams showed 105% and 78% increases in specific stiffness and modulus over 2L-T-I1. All 2L configurations outperformed 1L beams in specific stiffness, likely due to their higher second moment of area. For instance, 2L-C-I4 beams had 30% higher specific stiffness than their 1L counterparts. However, 2L beams showed reduced specific modulus compared to 1L beams, due to larger unsupported spans in corrugated/rectangular cores and increased line contact in triangular cores. As depicted in figure S5.2 (g) – (h), the 2L-C configurations exhibit higher specific flexural strength compared to 2L-R and 2L-T structures, suggesting greater density and/or mass of the rectangular and triangular core sandwich beams. Similarly, the 2L-C-I4 and 2L-R-I4 structures demonstrated superior specific strength relative to 2L-C-I1/I2 and 2L- R-I1/I2, due to increased fiber content that enhanced load-bearing capacity while maintaining nearly constant density due to the presence of porosity in I4. Figure S5.2 (g) exhibits comparable trends for 1L-C-I4 and 1L-R-I4 beams. In general, sandwich structures with triangular cores, whether 1L or 2L, fabricated using inks I1-I4, exhibit higher densities (table S5.1) compared to their rectangular and corrugated counterparts, indicating a heavier build. However, as depicted in figure S5.2 (g) – (h), 1L sandwich structures generally demonstrate higher specific flexural strength compared to 2L variants, likely due to the increased flexure resistance. Sandwich structures with identical base materials (I1–I4) and layer configurations (1L or 2L) but different core geometries exhibited mixed specific flexural strength, influenced by density variation, voids, cross-sectional differences, and bending stiffness.

References

[1] San Ha N, Lu G. A review of recent research on bio-inspired structures and materials for energy absorption applications. Composites Part B: Engineering. 2020;181:107496.
[2] Mohammadi H, Ahmad Z, Petrů M, Mazlan SA, Johari MAF, Hatami H, et al. An insight from nature: honeycomb pattern in advanced structural design for impact energy absorption. Journal of Materials Research and Technology. 2023;22:2862-87.
[3] Zhang Q, Yang X, Li P, Huang G, Feng S, Shen C, et al. Bioinspired engineering of honeycomb structure–Using nature to inspire human innovation. Progress in Materials Science. 2015;74:332-400.
[4] Sreejith M, Rajeev R. Fiber reinforced composites for aerospace and sports applications. Fiber Reinforced Composites: Elsevier; 2021. p. 821-59.
[5] Arenas JP. Applications of acoustic textiles in automotive/transportation. Acoustic textiles. 2016:143-63.
[6] Palomba G, Epasto G, Sutherland L, Crupi V. Aluminium honeycomb sandwich as a design alternative for lightweight marine structures. Ships and Offshore Structures. 2022;17(10):2355-66.
[7] Sanami M, Ravirala N, Alderson K, Alderson A. Auxetic materials for sports applications. Procedia Engineering. 2014;72:453-8.
[8] Pehlivan L, Baykasoğlu C. An experimental study on the compressive response of CFRP honeycombs with various cell configurations. Composites Part B: Engineering. 2019;162:653-61.
[9] Rejab M, Cantwell W. The mechanical behaviour of corrugated-core sandwich panels. Composites Part B: Engineering. 2013;47:267-77.
[10] Compton BG, Lewis JA. 3D-printing of lightweight cellular composites. Advanced materials. 2014;26(34):5930-5.
[11] George T, Deshpande V, Wadley H. Hybrid carbon fiber composite lattice truss structures. Composites Part A: Applied Science and Manufacturing. 2014;65:135-47.
[12] Zeng C, Liu L, Bian W, Leng J, Liu Y. Compression behavior and energy absorption of 3D printed continuous fiber reinforced composite honeycomb structures with shape memory effects. Additive Manufacturing. 2021;38:101842.
[13] Sugiyama K, Matsuzaki R, Ueda M, Todoroki A, Hirano Y. 3D printing of composite sandwich structures using continuous carbon fiber and fiber tension. Composites Part A: Applied Science and Manufacturing. 2018;113:114-21.
[14] Dou H, Ye W, Zhang D, Cheng Y, Wu C. Comparative study on in-plane compression properties of 3D printed continuous carbon fiber reinforced composite honeycomb and aluminum alloy honeycomb. Thin-Walled Structures. 2022;176:109335.
[15] Andrew JJ, Alhashmi H, Schiffer A, Kumar S, Deshpande VS. Energy absorption and self-sensing performance of 3D printed CF/PEEK cellular composites. Materials & Design. 2021;208:109863.
[16] Gibson LJ. Cellular solids. Mrs Bulletin. 2003;28(4):270-4.
[17] Dong Z, Li Y, Zhao T, Wu W, Xiao D, Liang J. Experimental and numerical studies on the compressive mechanical properties of the metallic auxetic reentrant honeycomb. Materials & Design. 2019;182:108036.
[18] Kim DS, Lee JR. Compressive mechanical properties of the nomex/thermoset honeycomb cores. Polymers for Advanced Technologies. 1997;8(1):1-7.

[19] Ahmad S, Zhang J, Feng P, Yu D, Wu Z, Ke M. Processing technologies for Nomex honeycomb composites (NHCs): A critical review. Composite Structures. 2020;250:112545.
[20] George J, Onodera J, Miyata T. Biodegradable honeycomb collagen scaffold for dermal tissue engineering. Journal of Biomedical Materials Research Part A: An Official Journal of The Society for Biomaterials, The Japanese Society for Biomaterials, and The Australian Society for Biomaterials and the Korean Society for Biomaterials. 2008;87(4):1103-11.
[21] Campbell F. Structural Composite Materials. ASM International. 2010;14.
[22] Rupani SV, Acharya G, Jani SS. Design, modelling and manufacturing aspects of honeycomb sandwich structures: a review. 2017.
[23] Wei X, Xiong J, Wang J, Xu W. New advances in fiber-reinforced composite honeycomb materials. Science China Technological Sciences. 2020;63(8):1348-70.
[24] Stocchi A, Colabella L, Cisilino A, Álvarez V. Manufacturing and testing of a sandwich panel honeycomb core reinforced with natural-fiber fabrics. Materials & Design. 2014;55:394-403.
[25] Han D, Tsai SW. Interlocked composite grids design and manufacturing. Journal of Composite Materials. 2003;37(4):287-316.
[26] Xiong J, Zhang M, Stocchi A, Hu H, Ma L, Wu L, et al. Mechanical behaviors of carbon fiber composite sandwich columns with three dimensional honeycomb cores under in-plane compression. Composites Part B: Engineering. 2014;60:350-8.
[27] Xiong J, Ma L, Stocchi A, Yang J, Wu L, Pan S. Bending response of carbon fiber composite sandwich beams with three dimensional honeycomb cores. Composite Structures. 2014;108:234-42.
[28] Cote F, Deshpande V, Fleck N, Evans A. The out-of-plane compressive behavior of metallic honeycombs. Materials Science and Engineering: A. 2004;380(1-2):272-80.
[29] Russell B, Deshpande V, Wadley H. Quasistatic deformation and failure modes of composite square honeycombs. Journal of mechanics of materials and structures. 2008;3(7):1315-40.
[30] Fan H, Meng F, Yang W. Mechanical behaviors and bending effects of carbon fiber reinforced lattice materials. Archive of Applied Mechanics. 2006;75:635-47.
[31] Fan H, Meng F, Yang W. Sandwich panels with Kagome lattice cores reinforced by carbon fibers. Composite structures. 2007;81(4):533-9.
[32] Xiong J, Vaziri A, Ghosh R, Hu H, Ma L, Wu L. Compression behavior and energy absorption of carbon fiber reinforced composite sandwich panels made of three-dimensional honeycomb grid cores. Extreme Mechanics Letters. 2016;7:114-20.
[33] Zuhri M, Guan Z, Cantwell W. The mechanical properties of natural fibre based honeycomb core materials. Composites Part B: Engineering. 2014;58:1-9.
[34] Vitale JP, Francucci G, Xiong J, Stocchi A. Failure mode maps of natural and synthetic fiber reinforced composite sandwich panels. Composites Part A: Applied Science and Manufacturing. 2017;94:217-25.
[35] Wei X, Li D, Xiong J. Fabrication and mechanical behaviors of an all-composite sandwich structure with a hexagon honeycomb core based on the tailor-folding approach. Composites Science and Technology. 2019;184:107878.
[36] Mondal A, Saha MC. 3D Printing and Characterization of Carbon Fiber Epoxy Composites. Available at SSRN 4905841. 2024.
[37] MONDAL A, SAHA MC, MAITY K, ALTAN MC, LIU Y. Analysis of Fiber Flow, Fiber Orientation, and Void Formation at Syringe-Nozzle Junction in Material Extrusion Additive Manufacturing of Short Carbon Fiber Epoxy Composites. PROCEEDINGS OF THE

AMERICAN SOCIETY FOR COMPOSITES-THIRTY-EIGHTH TECHNICAL CONFERENCE2023.
[38] Maity K, Mondal A, Saha MC. Cellulose nanocrystal-based all-3D-printed pyro-piezoelectric nanogenerator for hybrid energy harvesting and self-powered cardiorespiratory monitoring toward the human–machine interface. ACS Applied Materials & Interfaces. 2023;15(11):13956-70.
[39] MONDAL A, SAHA MC, MAITY K, ALTAN MC, LIU Y. Characterization and Improvisation of Direct-Ink-Writing (DIW) Technique with In-Situ Electric Field to Print Highly Aligned Carbon Fiber/Epoxy Composite. PROCEEDINGS OF THE AMERICAN SOCIETY FOR COMPOSITES-THIRTY-SEVENTH TECHNICAL CONFERENCE2022.
[40] Mondal A, Saha MC, Jiang Y, Rhule D, Sabisch JE. Direct ink writing of hexagonal honeycomb carbon fiber-reinforced epoxy composites with varying cell geometric parameters and tailored in-plane compressive properties. Polymer Composites. 2025.
[41] MONDAL A, MAITY K, SAHA MC, LIU Y. Direct-ink-writing (DIW) of higher weight concentration of milled carbon fiber (MCF) reinforced epoxy composite. Proceedings of the American Society for Compositesâ€" Thirty-Sixth Technical Conference on Composite Materials2021.
[42] Mondal A, Maity K, Saha M, Patterson S, Robison T. Direct-Ink-Writing of Flexible Sensor Array for Large Area Pressure Mapping. Kansas City Nuclear Security Campus (KCNSC), Kansas City, MO (United States); 2022.
[43] Rhule D, Mondal A, Saha M, Cummings L, Robison T. Effect of Silica and Mixing Time on Microstructures of Porous Polymer Composite by Emulsion Templating. Kansas City Nuclear Security Campus (KCNSC), Kansas City, MO (United States); 2023.
[44] MONDAL A, SUKATI M, SAHA MC, LIU Y, PATTERSON S, ROBISON T. Evaluation of Direct-Ink-Writing (DIW) of PDMS Hybrid Nanocomposite Ink for Piezoresistive Sensor Applications. Proceedings of the American Society for Composites â€" Thirty-fifth Technical Conference2020.
[45] MONDAL A, SUKATI M, CHARARA M, SAHA MC, LIU Y, PATTERSON S, et al. Investigation of Rheology and 3D Printability of PDMS Nanocomposites Ink. Proceedings of the American Society for Composites â€" Thirty-fourth Technical Conference2019.
[46] Zeng C, Liu L, Bian W, Leng J, Liu Y. Bending performance and failure behavior of 3D printed continuous fiber reinforced composite corrugated sandwich structures with shape memory capability. Composite Structures. 2021;262:113626.
[47] Zhang H, Chen J, Yang D. Fibre misalignment and breakage in 3D printing of continuous carbon fibre reinforced thermoplastic composites. Additive manufacturing. 2021;38:101775.
[48] Cheng P, Peng Y, Li S, Rao Y, Le Duigou A, Wang K, et al. 3D printed continuous fiber reinforced composite lightweight structures: A review and outlook. Composites Part B: Engineering. 2023;250:110450.
[49] Saadi M, Maguire A, Pottackal NT, Thakur MSH, Ikram MM, Hart AJ, et al. Direct ink writing: a 3D printing technology for diverse materials. Advanced Materials. 2022;34(28):2108855.
[50] Wu T, Jiang P, Zhang X, Guo Y, Ji Z, Jia X, et al. Additively manufacturing high-performance bismaleimide architectures with ultraviolet-assisted direct ink writing. Materials & Design. 2019;180:107947.
[51] Ziaee M, Johnson JW, Yourdkhani M. 3D printing of short-carbon-fiber-reinforced thermoset polymer composites via frontal polymerization. ACS Applied Materials & Interfaces. 2022;14(14):16694-702.

[52] Bay RS, Tucker III CL. Stereological measurement and error estimates for three-dimensional fiber orientation. Polymer Engineering & Science. 1992;32(4):240-53.
[53] Zhang J, Su Y, Zhang C, Li M, Zhu X, Zhang Y, et al. Alterations in rheo-viscoelastic properties of cement composites with biochar incorporation as bio-based admixture. Construction and Building Materials. 2024;439:137358.
[54] Lourenço LR, Borges R, Carastan D, Mathor MB, Marchi J. Precision 3D printing of chitosan-bioactive glass inks: Rheological optimization for enhanced shape fidelity in tissue engineering scaffolds. Bioprinting. 2024;43:e00359.
[55] Guo Y, Liu Y, Liu J, Zhao J, Zhang H, Zhang Z. Shape memory epoxy composites with high mechanical performance manufactured by multi-material direct ink writing. Composites Part A: Applied Science and Manufacturing. 2020;135:105903.
[56] Grosskopf AK, Truby RL, Kim H, Perazzo A, Lewis JA, Stone HA. Viscoplastic matrix materials for embedded 3D printing. ACS applied materials & interfaces. 2018;10(27):23353-61.
[57] Ajinjeru C, Kishore V, Chen X, Hershey C, Lindahl J, Kunc V, et al. Rheological survey of carbon fiber-reinforced high-temperature thermoplastics for big area additive manufacturing tooling applications. Journal of Thermoplastic Composite Materials. 2021;34(11):1443-61.
[58] Jiang G, Turner TA, Pickering SJ. The shear viscosity of carbon fibre suspension and its application for fibre length measurement. Rheologica Acta. 2016;55:1-10.
[59] Gavrilov AA, Finnikov KA, Podryabinkin EV. Modeling of steady Herschel–Bulkley fluid flow over a sphere. Journal of Engineering Thermophysics. 2017;26:197-215.
[60] Siqueira G, Kokkinis D, Libanori R, Hausmann MK, Gladman AS, Neels A, et al. Cellulose nanocrystal inks for 3D printing of textured cellular architectures. Advanced Functional Materials. 2017;27(12):1604619.
[61] Islam MN, Jiang Y. 3D printable sustainable composites with thermally tunable properties entirely from corn-based products. ACS Sustainable Chemistry & Engineering. 2022;10(24):7818-24.
[62] Khatri NR, Islam MN, Cao P-F, Advincula RC, Choi W, Jiang Y. Integrating helicoid channels for passive control of fiber alignment in direct-write 3D printing. Additive Manufacturing. 2021;48:102419.
[63] Aghajani S, Wu C, Li Q, Fang J. Additively manufactured composite lattices: A state-of-the-art review on fabrications, architectures, constituent materials, mechanical properties, and future directions. Thin-Walled Structures. 2023:111539.
[64] Niendorf K, Raeymaekers B. Additive manufacturing of polymer matrix composite materials with aligned or organized filler material: a review. Advanced Engineering Materials. 2021;23(4):2001002.
[65] Pham M-S, Liu C, Todd I, Lertthanasarn J. Damage-tolerant architected materials inspired by crystal microstructure. Nature. 2019;565(7739):305-11.
[66] Schaedler TA, Ro CJ, Sorensen AE, Eckel Z, Yang SS, Carter WB, et al. Designing metallic microlattices for energy absorber applications. Advanced Engineering Materials. 2014;16(3):276-83.
[67] Habib F, Iovenitti P, Masood S, Nikzad M. In-plane energy absorption evaluation of 3D printed polymeric honeycombs. Virtual and Physical Prototyping. 2017;12(2):117-31.
[68] Zhang P, Arceneaux DJ, Khattab A. Mechanical properties of 3D printed polycaprolactone honeycomb structure. Journal of Applied Polymer Science. 2018;135(12):46018.
[69] Bates SR, Farrow IR, Trask RS. 3D printed polyurethane honeycombs for repeated tailored energy absorption. Materials & Design. 2016;112:172-83.

[70] Chohan JS, Singh R, Boparai KS, Penna R, Fraternali F. Dimensional accuracy analysis of coupled fused deposition modeling and vapour smoothing operations for biomedical applications. Composites Part B: Engineering. 2017;117:138-49.
[71] Wang X, Jiang M, Zhou Z, Gou J, Hui D. 3D printing of polymer matrix composites: A review and prospective. Composites Part B: Engineering. 2017;110:442-58.
[72] Pratama J, Cahyono SI, Suyitno S, Muflikhun MA, Salim UA, Mahardika M, et al. A review on reinforcement methods for polymeric materials processed using Fused Filament Fabrication (FFF). Polymers. 2021;13(22):4022.
[73] Li J, Durandet Y, Huang X, Sun G, Ruan D. Additively manufactured fiber-reinforced composites: A review of mechanical behavior and opportunities. Journal of Materials Science & Technology. 2022;119:219-44.
[74] Blok LG, Longana ML, Yu H, Woods BK. An investigation into 3D printing of fibre reinforced thermoplastic composites. Additive Manufacturing. 2018;22:176-86.
[75] Somireddy M, Singh C, Czekanski A. Mechanical behaviour of 3D printed composite parts with short carbon fiber reinforcements. Engineering Failure Analysis. 2020;107:104232.
[76] Shofner M, Lozano K, Rodríguez-Macías F, Barrera E. Nanofiber-reinforced polymers prepared by fused deposition modeling. Journal of applied polymer science. 2003;89(11):3081-90.
[77] Tekinalp HL, Kunc V, Velez-Garcia GM, Duty CE, Love LJ, Naskar AK, et al. Highly oriented carbon fiber–polymer composites via additive manufacturing. Composites Science and Technology. 2014;105:144-50.
[78] Anwer A, Naguib HE. Multi-functional flexible carbon fiber composites with controlled fiber alignment using additive manufacturing. Additive Manufacturing. 2018;22:360-7.
[79] Liu S, Li Y, Li N. A novel free-hanging 3D printing method for continuous carbon fiber reinforced thermoplastic lattice truss core structures. Materials & Design. 2018;137:235-44.
[80] Raney JR, Compton BG, Mueller J, Ober TJ, Shea K, Lewis JA. Rotational 3D printing of damage-tolerant composites with programmable mechanics. Proceedings of the National Academy of Sciences. 2018;115(6):1198-203.
[81] Yu W, Zhou H, Li BQ, Ding S. 3D printing of carbon nanotubes-based microsupercapacitors. ACS applied materials & interfaces. 2017;9(5):4597-604.
[82] Ozbolat V, Dey M, Ayan B, Povilianskas A, Demirel MC, Ozbolat IT. 3D printing of PDMS improves its mechanical and cell adhesion properties. ACS Biomaterials Science & Engineering. 2018;4(2):682-93.
[83] García-Tuñón E, Feilden E, Zheng H, D'Elia E, Leong A, Saiz E. Graphene oxide: an all-in-one processing additive for 3D printing. ACS applied materials & interfaces. 2017;9(38):32977-89.
[84] Lewicki JP, Rodriguez JN, Zhu C, Worsley MA, Wu AS, Kanarska Y, et al. 3D-printing of meso-structurally ordered carbon fiber/polymer composites with unprecedented orthotropic physical properties. Scientific reports. 2017;7(1):43401.
[85] Li VC-F, Dunn CK, Zhang Z, Deng Y, Qi HJ. Direct ink write (DIW) 3D printed cellulose nanocrystal aerogel structures. Scientific reports. 2017;7(1):8018.
[86] Quan C, Han B, Hou Z, Zhang Q, Tian X, Lu TJ. 3d printed continuous fiber reinforced composite auxetic honeycomb structures. Composites Part B: Engineering. 2020;187:107858.
[87] Hou Z, Tian X, Zhang J, Li D. 3D printed continuous fibre reinforced composite corrugated structure. Composite Structures. 2018;184:1005-10.

[88] Long Y, Zhang Z, Yan C, Huang Z, Fu K, Li Y. Multi-objective optimization for improving printing efficiency and mechanical properties of 3D-printed continuous plant fibre composites. Composites Communications. 2022;35:101283.
[89] Cote F, Deshpande V, Fleck N. The shear response of metallic square honeycombs. Journal of Mechanics of Materials and Structures. 2006;1(7):1281-99.
[90] Nawafleh N, Wright W, Dariavach N, Celik E. 3D-printed thermoset syntactic foams with tailorable mechanical performance. Journal of Materials Science. 2020;55:16048-57.
[91] Um H-J, Lee J-S, Shin J-H, Kim H-S. 3D printed continuous carbon fiber reinforced thermoplastic composite sandwich structure with corrugated core for high stiffness/load capability. Composite Structures. 2022;291:115590.
[92] Cheng Y, Li J, Qian X, Rudykh S. 3D printed recoverable honeycomb composites reinforced by continuous carbon fibers. Composite Structures. 2021;268:113974.
[93] Tsouknidas A, Pantazopoulos M, Katsoulis I, Fasnakis D, Maropoulos S, Michailidis N. Impact absorption capacity of 3D-printed components fabricated by fused deposition modelling. Materials & Design. 2016;102:41-4.
[94] Vidakis N, Petousis M, Kechagias J. Parameter effects and process modelling of Polyamide 12 3D-printed parts strength and toughness. Materials and Manufacturing Processes. 2022;37(11):1358-69.
[95] Fleck NA, Deshpande VS, Ashby MF. Micro-architectured materials: past, present and future. Proceedings of the Royal Society A: Mathematical, Physical and Engineering Sciences. 2010;466(2121):2495-516.
[96] Chen Y, Li T, Jia Z, Scarpa F, Yao C-W, Wang L. 3D printed hierarchical honeycombs with shape integrity under large compressive deformations. Materials & Design. 2018;137:226-34.
[97] Han B, Yan LL, Yu B, Zhang QC, Chen CQ, Lu TJ. Collapse mechanisms of metallic sandwich structures with aluminum foam-filled corrugated cores. J Mech Mater Struct. 2014;9(4):397-425.
[98] Xiong J, Ma L, Vaziri A, Yang J, Wu L. Mechanical behavior of carbon fiber composite lattice core sandwich panels fabricated by laser cutting. Acta Materialia. 2012;60(13-14):5322-34.
[99] Feng L-J, Wu L-Z, Yu G-C. An Hourglass truss lattice structure and its mechanical performances. Materials & Design. 2016;99:581-91.
[100] Liu J, Liu J, Mei J, Huang W. Investigation on manufacturing and mechanical behavior of all-composite sandwich structure with Y-shaped cores. Composites Science and Technology. 2018;159:87-102.
[101] Li C, Lei H, Liu Y, Zhang X, Xiong J, Zhou H, et al. Crushing behavior of multi-layer metal lattice panel fabricated by selective laser melting. International Journal of Mechanical Sciences. 2018;145:389-99.
[102] Cao X, Duan S, Liang J, Wen W, Fang D. Mechanical properties of an improved 3D-printed rhombic dodecahedron stainless steel lattice structure of variable cross section. International Journal of Mechanical Sciences. 2018;145:53-63.
[103] Bitzer T. Honeycomb technology: materials, design, manufacturing, applications and testing: Springer Science & Business Media; 1997.
[104] Gibson RF. A review of recent research on mechanics of multifunctional composite materials and structures. Composite structures. 2010;92(12):2793-810.
[105] Gibson I, Rosen DW, Stucker B, Khorasani M, Rosen D, Stucker B, et al. Additive manufacturing technologies: Springer; 2021.

[106] Hammetter CI, Rinaldi RG, Zok FW. Pyramidal lattice structures for high strength and energy absorption. Journal of Applied Mechanics. 2013;80(4):041015.
[107] Zok* FW, Rathbun H, He M, Ferri E, Mercer C, McMeeking RM, et al. Structural performance of metallic sandwich panels with square honeycomb cores. Philosophical Magazine. 2005;85(26-27):3207-34.
[108] Fu Z, Schlier L, Travitzky N, Greil P. Three-dimensional printing of SiSiC lattice truss structures. Materials Science and Engineering: A. 2013;560:851-6.
[109] Turner AJ, Al Rifaie M, Mian A, Srinivasan R. Low-velocity impact behavior of sandwich structures with additively manufactured polymer lattice cores. Journal of Materials Engineering and Performance. 2018;27:2505-12.
[110] Finnegan KA. Carbon fiber composite pyramidal lattice structures: University of Virginia Charlottesville, VA; 2007.
[111] Lee B-C, Lee K-W, Byun J-H, Kang K-J. The compressive response of new composite truss cores. Composites Part B: Engineering. 2012;43(2):317-24.
[112] Wang B, Wu L, Ma L, Sun Y, Du S. Mechanical behavior of the sandwich structures with carbon fiber-reinforced pyramidal lattice truss core. Materials & Design (1980-2015). 2010;31(5):2659-63.
[113] Jishi H, Umer R, Cantwell W. The fabrication and mechanical properties of novel composite lattice structures. Materials & Design. 2016;91:286-93.
[114] Azzouz L, Chen Y, Zarrelli M, Pearce JM, Mitchell L, Ren G, et al. Mechanical properties of 3-D printed truss-like lattice biopolymer non-stochastic structures for sandwich panels with natural fibre composite skins. Composite Structures. 2019;213:220-30.
[115] Ngo TD, Kashani A, Imbalzano G, Nguyen KT, Hui D. Additive manufacturing (3D printing): A review of materials, methods, applications and challenges. Composites Part B: Engineering. 2018;143:172-96.
[116] Praveena B, Lokesh N, Buradi A, Santhosh N, Praveena B, Vignesh R. A comprehensive review of emerging additive manufacturing (3D printing technology): Methods, materials, applications, challenges, trends and future potential. Materials Today: Proceedings. 2022;52:1309-13.
[117] Al Abadi H, Thai H-T, Paton-Cole V, Patel V. Elastic properties of 3D printed fibre-reinforced structures. Composite Structures. 2018;193:8-18.
[118] Botelho E, Rezende M, Lauke B. Mechanical behavior of carbon fiber reinforced polyamide composites. Composites Science and Technology. 2003;63(13):1843-55.
[119] Mondal A, Saha M, Maity K, Altan MC, Liu Y. Characterization of 3D Printed Single Filament Carbon Fiber Epoxy Composite. ASME International Mechanical Engineering Congress and Exposition: American Society of Mechanical Engineers; 2022. p. V009T12A14.
[120] Praveen S, Santhoshkumar P, Joe YC, Senthil C, Lee CW. 3D-printed architecture of Li-ion batteries and its applications to smart wearable electronic devices. Applied Materials Today. 2020;20:100688.
[121] Zhang M, Mei H, Chang P, Cheng L. 3D printing of structured electrodes for rechargeable batteries. Journal of Materials Chemistry A. 2020;8(21):10670-94.
[122] Xu Y, Zhang F, Zhai W, Cheng S, Li J, Wang Y. Unraveling of advances in 3D-printed polymer-based bone scaffolds. Polymers. 2022;14(3):566.
[123] Gibson LJ, Ashby MF, Harley BA. Cellular materials in nature and medicine: Cambridge University Press; 2010.

[124] Ma Q, Rejab M, Kumar AP, Fu H, Kumar NM, Tang J. Effect of infill pattern, density and material type of 3D printed cubic structure under quasi-static loading. Proceedings of the Institution of Mechanical Engineers, Part C: Journal of Mechanical Engineering Science. 2021;235(19):4254-72.
[125] Feng L-J, Yang Z-T, Yu G-C, Chen X-J, Wu L-Z. Compressive and shear properties of carbon fiber composite square honeycombs with optimized high-modulus hierarchical phases. Composite Structures. 2018;201:845-56.
[126] Rebelo H, Lecompte D, Cismasiu C, Jonet A, Belkassem B, Maazoun A. Experimental and numerical investigation on 3D printed PLA sacrificial honeycomb cladding. International Journal of Impact Engineering. 2019;131:162-73.
[127] Sun G, Li S, Liu Q, Li G, Li Q. Experimental study on crashworthiness of empty/aluminum foam/honeycomb-filled CFRP tubes. Composite Structures. 2016;152:969-93.
[128] Kumar SA, Ahmed KS. Compression behavior and energy absorption capacity of stiffened syntactic foam core sandwich composites. Journal of Reinforced Plastics and Composites. 2013;32(18):1370-9.
[129] Liu H, Chen L, Du B, Peng S, Guo Y, Zhao Y, et al. Flatwise compression property of hierarchical thermoplastic composite square lattice. Composite Structures. 2019;210:118-33.
[130] Wang Z, Lu Z, Tian H, Yao S, Zhou W. Theoretical assessment methodology on axial compressed hexagonal honeycomb's energy absorption capability. Mechanics of Advanced Materials and Structures. 2016;23(5):503-12.
[131] Zhang Y, Chen T, Xu X, Hu Z. Out-of-plane mechanical behaviors of a side hierarchical honeycomb. Mechanics of Materials. 2020;140:103227.
[132] Xiong J, Ma L, Wu L, Wang B, Vaziri A. Fabrication and crushing behavior of low density carbon fiber composite pyramidal truss structures. Composite Structures. 2010;92(11):2695-702.
[133] Schaedler TA, Carter WB. Architected cellular materials. Annual Review of Materials Research. 2016;46(1):187-210.
[134] Yang L, Fan H, Liu J, Ma Y, Zheng Q. Hybrid lattice-core sandwich composites designed for microwave absorption. Materials & Design. 2013;50:863-71.
[135] Wei K, He R, Cheng X, Zhang R, Pei Y, Fang D. A lightweight, high compression strength ultra high temperature ceramic corrugated panel with potential for thermal protection system applications. Materials & design. 2015;66:552-6.
[136] Gao L, Sun Y. Fluid flow and heat transfer characteristics of composite lattice core sandwich structures. Journal of Thermophysics and Heat Transfer. 2014;28(2):258-69.
[137] Malek S, Raney JR, Lewis JA, Gibson LJ. Lightweight 3D cellular composites inspired by balsa. Bioinspiration & biomimetics. 2017;12(2):026014.
[138] Xiao D, Chen X, Li Y, Wu W, Fang D. The structure response of sandwich beams with metallic auxetic honeycomb cores under localized impulsive loading-experiments and finite element analysis. Materials & Design. 2019;176:107840.
[139] Chen L, Fan H, Sun F, Zhao L, Fang D. Improved manufacturing method and mechanical performances of carbon fiber reinforced lattice-core sandwich cylinder. Thin-Walled Structures. 2013;68:75-84.
[140] Chua CK, Leong KF. 3D Printing and additive manufacturing: Principles and applications (with companion media pack)-of rapid prototyping: World Scientific Publishing Company; 2014.
[141] Tan WS, Chua CK, Chong TH, Fane AG, Jia A. 3D printing by selective laser sintering of polypropylene feed channel spacers for spiral wound membrane modules for the water industry. Virtual and Physical Prototyping. 2016;11(3):151-8.

[142] Manapat JZ, Chen Q, Ye P, Advincula RC. 3D printing of polymer nanocomposites via stereolithography. Macromolecular Materials and Engineering. 2017;302(9):1600553.
[143] Jiang Y, Raney JR. 3D printing of amylopectin-based natural fiber composites. Advanced Materials Technologies. 2019;4(11):1900521.
[144] Croom BP, Abbott A, Kemp JW, Rueschhoff L, Smieska L, Woll A, et al. Mechanics of nozzle clogging during direct ink writing of fiber-reinforced composites. Additive Manufacturing. 2021;37:101701.
[145] Anoop M, Senthil P, Sooraj V. An investigation on viscoelastic characteristics of 3D-printed FDM components using RVE numerical analysis. Journal of the Brazilian Society of Mechanical Sciences and Engineering. 2021;43:1-13.
[146] Yan L, Han B, Yu B, Chen C, Zhang Q, Lu T. Three-point bending of sandwich beams with aluminum foam-filled corrugated cores. Materials & Design. 2014;60:510-9.
[147] Wang J, Shi C, Yang N, Sun H, Liu Y, Song B. Strength, stiffness, and panel peeling strength of carbon fiber-reinforced composite sandwich structures with aluminum honeycomb cores for vehicle body. Composite Structures. 2018;184:1189-96.
[148] Hussain M, Abbas N, Zahra N, Sajjad U, Awan MB. Investigating the performance of GFRP/wood-based honeycomb sandwich panels for sustainable prefab building construction. SN Applied Sciences. 2019;1:1-8.
[149] Sarvestani HY, Akbarzadeh A, Mirbolghasemi A, Hermenean K. 3D printed meta-sandwich structures: Failure mechanism, energy absorption and multi-hit capability. Materials & Design. 2018;160:179-93.
[150] Djama K, Michel L, Gabor A, Ferrier E. Mechanical behaviour of a sandwich panel composed of hybrid skins and novel glass fibre reinforced polymer truss core. Composite Structures. 2019;215:35-48.
[151] Fan H, Zhou Q, Yang W, Jingjing Z. An experiment study on the failure mechanisms of woven textile sandwich panels under quasi-static loading. Composites Part B: Engineering. 2010;41(8):686-92.
[152] Smardzewski J, Wojciechowski KW. Response of wood-based sandwich beams with three-dimensional lattice core. Composite Structures. 2019;216:340-9.
[153] Kaboglu C, Yu L, Mohagheghian I, Blackman BR, Kinloch AJ, Dear JP. Effects of the core density on the quasi-static flexural and ballistic performance of fibre-composite skin/foam-core sandwich structures. Journal of Materials Science. 2018;53:16393-414.